

Cornell Center for Materials Research

Research Experience for Undergraduates Summer Program 2015

Section 1



Support for the REU program is provided by the NSF MRSEC program (DMR-1120296) and the REU Site program (DMR-1063059).



Table of Contents

<u>REU</u>	<u>Faculty Advisor</u>	<u>Page</u>
Agata, Wendy Angela	Prof. Darrell Schlom	3
Bigenwald, Eric	Prof. Darrell Schlom	9
Blash, Conrad	Prof. Mike Spencer	26
Dupuis, Lauren	Prof. Brett Fors	38
Frye, Liliana	Prof. Greg Fuchs	46
Gelb, Madeline	Prof. Chris Ober	51
Guan, Orion	Prof. Dan Ralph	58
Gupta, Nisha	Prof. Christopher Hernandez	65
Ivanoff, Douglas	Prof. Jonathan Butcher	71
Kaplan, Alan	Prof. Jiwoong Park	77
Kellogg, William	Prof. Tobias Hanrath	81

X-Ray Diffraction: Understanding Defects in Crystalline Oxide Thin Films

Saring Agata, Natalie Dawley, Dr. Darrell Schlom

Materials Science and Engineering Department, Cornell University, Ithaca, NY, 14853, U.S.A.

Abstract

Using background knowledge about X-ray diffraction and the common defects found in oxide thin film, the $2\theta/\omega$ scans of $4 \text{ Sr}_2\text{TiO}_4$ on LSAT of $\sim 30 \text{ nm}$ thickness samples were analyzed using both qualitative analysis and the measurement of percentage off monolayer completion between strontium and titanium all in comparison to a computer generated “ideal” $2\theta/\omega$ scan. Further, the rocking curves (ω scans) of a $\text{Sr}_3\text{Ti}_2\text{O}_7$ -(BaTiO_3) on DyScO_3 (100) substrate of $\sim 50 \text{ nm}$ thickness sample was qualitatively analyzed and a modified Williamson-Hall analysis was performed all of which to determine the presence of size effects and defect-induced strain as well as high defect density. After successful generation of these scans analysis concluded the existence of a sinusoidal relationship between percent off monolayer completion and film to substrate FWHM ratio, the existence of defects in both types of samples, and a particularly high defect density of most likely stacking faults in our rocking curve sample.

Background

The use of oxide thin films in MOSFET transistors and other semiconductors has proven to be a revolutionary addition to the already thriving area of semiconductor research. Their ability to alter the mechanical, optical, and electrical properties of these semiconductors allows them to be used as tunable dielectrics significantly widening the application and functionality of these semiconductors/ transistors. Tunable dielectrics are the basis of numerous industrial coatings and are used in the design of satellites.

²Understanding the defects seen in these oxide thin film dielectrics is crucial to eliminating the effects of dielectric loss caused by these defects specifically with perovskite oxide thin films like the Ruddlesden-Popper superlattice structured films unique due to their use at low temperatures, and therefore at low energy. X-ray diffraction is an extremely useful characterization technique for thin films especially in its unique representation of defects. As a result of its use of the key physics principle of diffraction, we are able to gain useful information about the presence of these defects and incite on the gravity of their effect on the quality of the sample due to changes in intensity and width of peaks.

Background

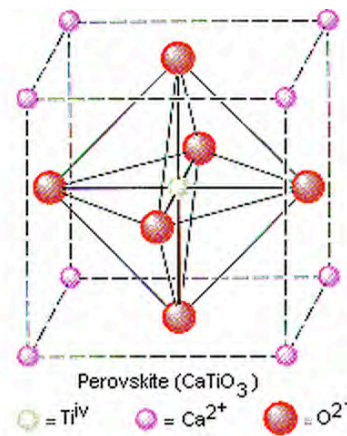


Figure 1- Basic perovskite structure shown with calcium titanate. Perovskites are known for their octahedral structure and face-centered oxygens (shown in red)

Perovskites:

The Ruddlesden-Popper superlattice crystal structure falls under the crystalline classification of perovskite, a type of crystal structure known for its ABO_3 chemical formula.⁵ (Figure 1) This crystalline structure can accommodate up to 30 different elements on site A with 100% substitution and over half the periodic table in the B position.⁵ Perovskites have been known to enhance semiconductor capabilities in numerous ways regarding ferromagnetism, piezoelectric, polarization and other electric and magnetic properties outlined in Figure 2.⁵

Table I. Examples of the Properties of Oxides

Property	Value	Oxide material	References
Mobility	$\mu = 22\,000 \text{ cm}^2 \cdot (\text{V} \cdot \text{s})^{-1} (2 \text{ K})$	SrTiO ₃	Tufte and Chapman ¹¹
Metal-insulator transition	$\Delta R/R_{T_{\text{low}}} > 10^{13}$	EuO	Petrich <i>et al.</i> ¹²
Superconductivity	$T_c = 135 \text{ K}$	HgBa ₂ Ca ₂ Cu ₃ O _{8+x}	Schilling <i>et al.</i> ¹³
Ferroelectricity	$P_s = 105 \text{ } \mu\text{C}/\text{cm}^2$ $P_s = 100 \text{ } \mu\text{C}/\text{cm}^2$	PbZr _{0.2} Ti _{0.8} O ₃ BiFeO ₃	Vrejoiu <i>et al.</i> ¹⁴ Wang <i>et al.</i> ¹⁵ Li <i>et al.</i> ¹⁶ Das <i>et al.</i> ¹⁷ Dho <i>et al.</i> ¹⁸
Piezoelectricity	$d_{33} = 2500 \text{ pC/N}$	PbZn _{1/3} Nb _{2/3} O ₃ -PbTiO ₃	Park <i>et al.</i> ¹⁹
Ferromagnetism	$M_s = 6.9 \text{ } \mu_B/\text{Eu}$	EuO	Matthias <i>et al.</i> ²⁰
Colossal magnetoresistance	$\Delta R/R_0 > 10^{11} (5 \text{ T})$	Pr _{0.7} Sr _{0.04} Ca _{0.26} MnO _{3-δ}	Maignan <i>et al.</i> ²¹
Magnetostriction	$\lambda_{100} = -590 \times 10^{-6}$	Co _{0.8} Fe _{2.2} O ₄	Bozorth <i>et al.</i> ²²
Faraday effect	$v = 4 \times 10^5 \text{ } ^\circ \cdot (\text{T} \cdot \text{cm})^{-1}$	EuO	Ahn and Shafer ²³
Spin polarization	$P > 98\%$	CrO ₂	Soulen <i>et al.</i> ²⁴ Anguelouch <i>et al.</i> ²⁵
Ferromagnetic and ferroelectric simultaneously	$T_c = 105 \text{ K}$ $T_c = 250 \text{ K}$	BiMnO ₃ LuFe ₂ O ₄ , FeTiO ₃	Hill and Rabe, ²⁹ Moreira dos Santos <i>et al.</i> , ²⁸ Sharan <i>et al.</i> , ³⁰ Baettig <i>et al.</i> ³¹ Ikeda <i>et al.</i> , Fennie ²⁷

Figure 2- A table representing the different properties different perovskites can enhance.⁶

Ruddlesden-Popper:

Ruddlesden-Popper (RP) superlattice crystals follow the perovskite chemical formula Sr_{n+1}Ti_nO_{3n+1} and are unique due to their ability to increase mobility, as shown in the above table, but also accommodate for defects commonly seen in thin film oxides through a reorganization of its otherwise organized layered structure. Layered oxides such as the RP superlattice are most successfully

ability to monitor the growth process as it occurs.

Thin Film Oxide Defects:

Common defects encountered by thin film oxides are usually classified into three different categories: point defects, linear defects, planar defects each specified by the dimension in which the defect affects the film.¹ The smallest scale of defect, the point defect is a result of the removal, replacement or addition of atoms within the Bravais lattice of the crystal. Self-interstitial atoms, interstitial impurity atoms, substitutional atoms, substitutional vacancies all act as sources for point defects and can result in either different magnetic and electric properties due to the presence or absence of atoms or an increase in stress due to an increasingly tightly packed lattice structure.^{1,2} Linear defects usually occur through dislocations, most commonly edge, screw, and misfit dislocations which can be thought of as a sort of shift in the ordering of atoms in the crystal lattice causing lattice

deposited using molecular beam epitaxy, a highly controlled vacuum deposition technique that takes advantage of the huge difference between surface and diffusion rates in oxides allowing the growth of films with superior structural order while preserving the potentially metastable layering of an oxide superlattice.² In addition, molecular beam epitaxy allows for an incomparable ability to control the layering of the structure at the monolayer level due to the

distortion and contributing to strain and also magnetic and electric variations in the film. Lastly, planar defects, some of the most common and effective defects result mainly from stacking faults and twinning.¹ Though each differ in the formation of the planar defect, both stacking faults and twinning are derived from a change in the intended growth mechanism either due to the desire for an overall lower energy profile or the appearance of two similar crystal parts symmetrically related to one another respectively.² All of these defects lead to a key issue, dielectric loss, the decreased ability to store electric charge due to the loss of power of electromagnetic waves traveling through a dielectric.^{2,3}

Method

To show the presence of defects in our strontium titanate samples, we followed the

following two procedures to try and understand the relationship between the percent off monolayer completion common in these samples and the presence of strain known to surround large-scale planar defects like stacking faults. We used a Mathematica code developed by our group to generate the rocking curve used for part of our analysis and analyze both the substrate and film FWHM. In addition, we used another Mathematica code developed by our group to generate an “ideal” $2\theta/\omega$ scan based on film structure, substrate, and film thickness, to show the qualitative differences defects can have on $2\theta/\omega$ scans. The percent off monolayer completion was calculated on the $2\theta/\omega$ scans of four Sr_2TiO_4 on LSAT of ~ 30 nm thickness. Williamson-Hall Analysis was performed on $1 \text{ Sr}_3\text{Ti}_2\text{O}_7\text{-(BaTiO}_3\text{)}$ on DyScO_3 (100) substrate of ~ 50 nm thickness.

Percent Off Monolayer Completion:

To perform this analysis we used a formula comparing the (002) and (004) position peaks in a $2\theta/\omega$ scan with the following form:

$$(1) d_{00n} = n \times \frac{\lambda}{2\theta}$$

$$(2) (d_{002}-d_{004}) \times 5 = \% \text{ off}$$

where d represents the lattice spacing at each peak’s Bragg angle, θ , and λ is the wavelength of the x-ray. After modification of their respective lattice spacings, shown Eqn(1), we were able to calculate an approximate value for the percentage off monolayer completion to give a general ideal of how close to the stoichiometric values of Sr and Ti each sample lies.

Modified Williamson-Hall Analysis:

To quantify the effects on peak width by defects we use a modified version of the Williamson-Hall Analysis, a rocking curve evaluation based on the understanding of the broadening effect of non-uniform strain, caused by extended defects such as stacking faults, on the reciprocal lattice points represented through the rocking curve.⁶ The formula model that is used to represent this broadening is as follows:

$$(3) \Delta\omega_{\text{measured}} = \Delta\omega_{\text{mosaic}} + \frac{\lambda}{2L \sin \theta}$$

where $\Delta\omega_{\text{measured}}$ represents the FWHM of the sample and $\Delta\omega_{\text{mosaic}}$ represents the deviation from the ideal omega value derived from Bragg’s law.⁶ The $\Delta\omega_{\text{mosaic}}$ value allows us to get a quantitative picture of how these large-scale defects are effecting the sample. It is important to note the distinction between the intentionally applied strain, used to improve properties already enhanced by these thin film oxides, from non-uniform unintentional strain which is a sign of defects and is shown through XRD.⁶

Results

After experimentation, we were able to determine the percent off monolayer completion for all four of our four Sr_2TiO_4 on LSAT of ~ 30 nm thickness samples from their $2\theta/\omega$ scans, compare these values with the film FWHM to substrate ratio, and check for consistency and correlations between the two. Furthermore, we were able to successfully generate the “ideal” $2\theta/\omega$ scan for samples of this type and compare for qualitative differences to prove the presence of defects. After successfully generating the rocking curve for our $\text{Sr}_3\text{Ti}_2\text{O}_7\text{-(BaTiO}_3\text{)}$ on DyScO_3 (100) substrate of ~ 50 nm thickness sample, we were able to qualitatively determine the existence of peaks as well as perform the modified Williamson-Hall analysis on our curve to quantitatively determine, using $\Delta\omega_{\text{mosaic}}$, the presence of strain possibly due to stacking faults.

Percent off Monolayer Completion results:

It is interesting to note the varied nature of film FWHM, substrate FWHM, and percent off monolayer completion for samples that are seemingly identical in original design and deposition. **Figure 3** shows the almost sinusoidal relationship between the two factors which suggests that there could be ranges of values of positive parabolic relationship between the two variables (below 100% and slightly above 100%) and ranges of negative parabolic relationship (significantly above 100%)

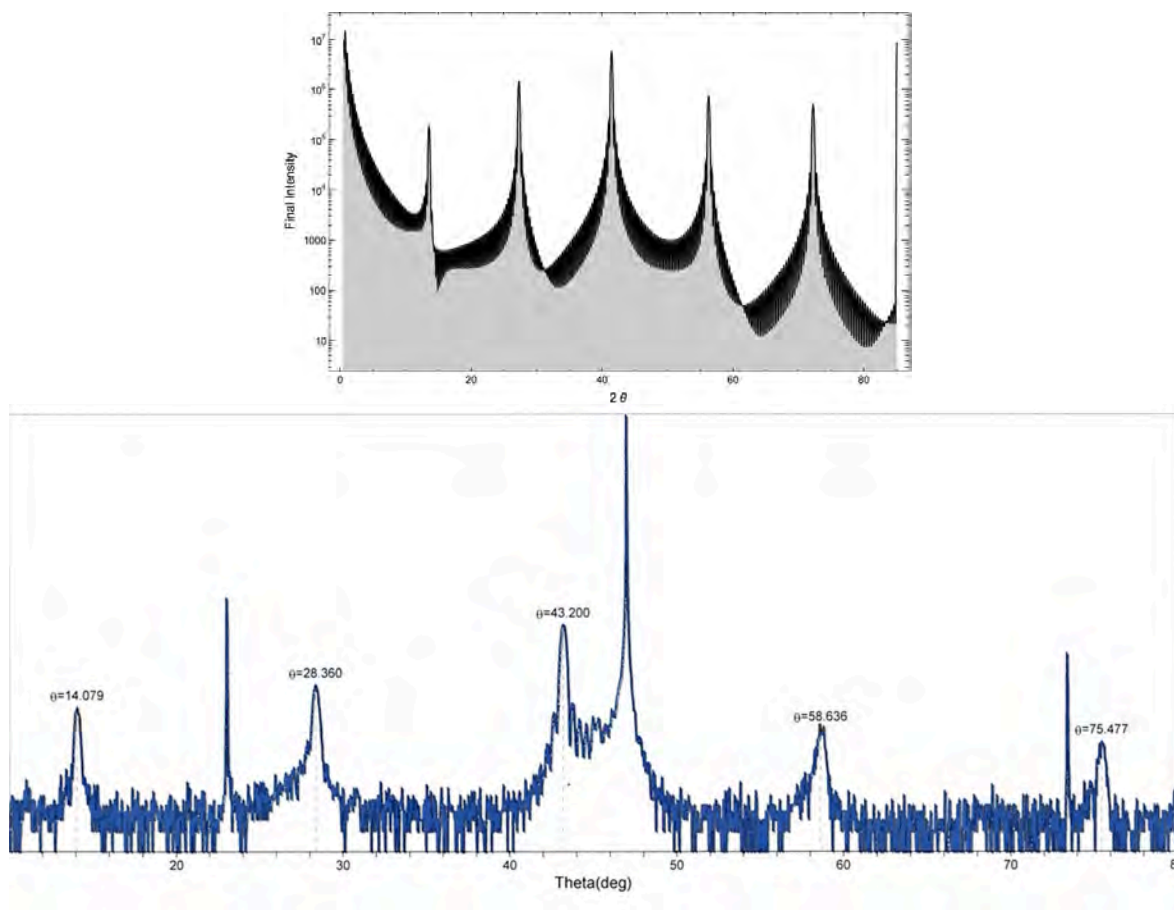
2θ/ω scan Analysis:

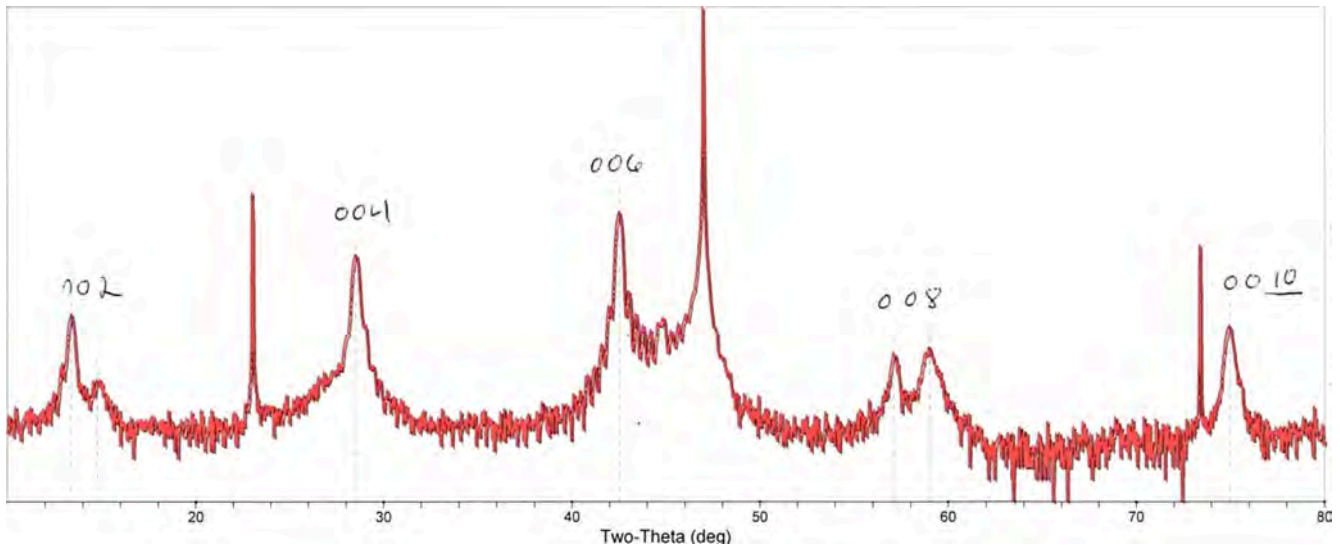
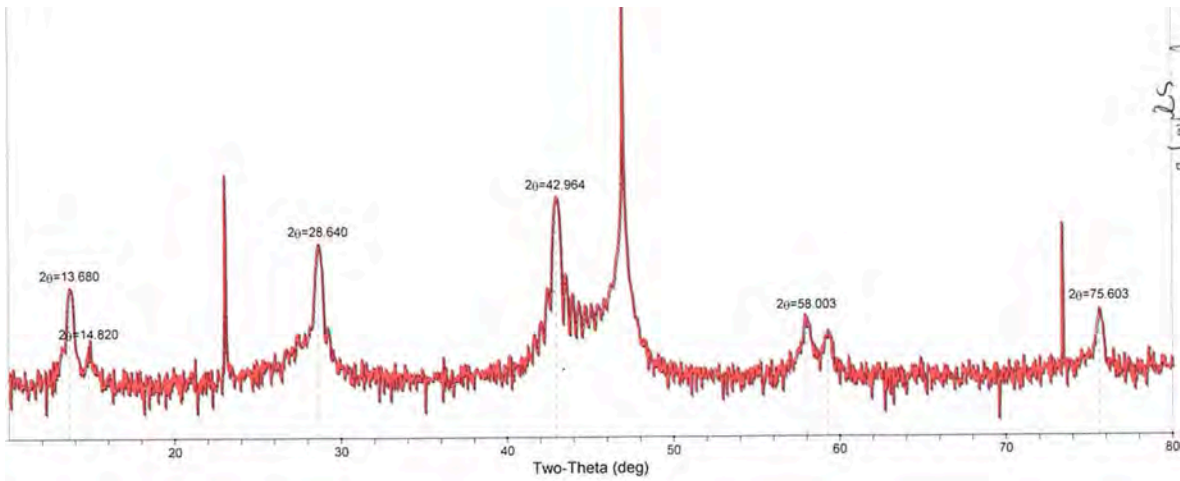
The first clear difference between each of our three shown $2\theta/\omega$ scans (**Figures 5,6,7**) is the lack of equidistance between each peak as well as the higher intensity of each peak in comparison to the computer-generated scan. Numerous factors related to overall environment of the samples through MBE and XRD could explain this consistent behavior throughout our samples but each scan also has a significant difference between the intensity of the substrate and film peaks, the film peak having a characteristically low intensity. Small peaks have been seen in XRD to be a reflection of composition fluctuations and vertical strain, the first of which is consistent with our percent off/FWHM data.⁴ Furthermore, in each sample there is either the peak of lowest intensity at the (008) or peak splitting representative of incompleteness of monolayer composition also consistent with the sinusoidal relationship

observed in **Figure 3**. Interestingly, there initially seems to be increased peak splitting as the percentage off increased, in both values far below 100% and far above, but this pattern ends at extreme values, like the sample with 113% off monolayer completion suggesting a possible correlation between peak splitting and increased deviation from monolayer completion up until a certain point. The values outside this correlated range could be the points at which defects are more likely to occur.

Rocking Curve Analysis:

After the successful generation of the rocking curve of the $\text{Sr}_3\text{Ti}_2\text{O}_7-(\text{BaTiO}_3)$ on $\text{DyScO}_3(100)$ substrate of ~ 50 nm thickness sample the modified Williamson-Hall Analysis revealed a $\Delta\omega_{\text{mosaic}}$ value of 8.666 arcseconds. This sample differs from the $2\theta/\omega$ scan samples due to the addition of barium into the superlattice structure. Barium was added to





Figures 4,5,6 & 7- The computer generated “ideal” $2\theta/\omega$ scan for Sr₂TiO₄ on LSAT of ~30nm thickness. The $2\theta/\omega$ scans for the -0.0355% off, 2.4% off, and 3.48% off Sr₂TiO₄ on LSAT of ~30 nm thickness samples respectively. Note the existence of peak splitting in Figures 6 & 7

further enhance the properties the strontium titanate oxide thin film contributes, as shown in numerous mixed metal perovskites listed in Figure 2.⁵ Though this sample has Barium in its superlattice, the large discrepancy between ideal and measured FWHM of our rocking curve, evidenced by the modified Williamson-Hall analysis, shows a significant size or defect

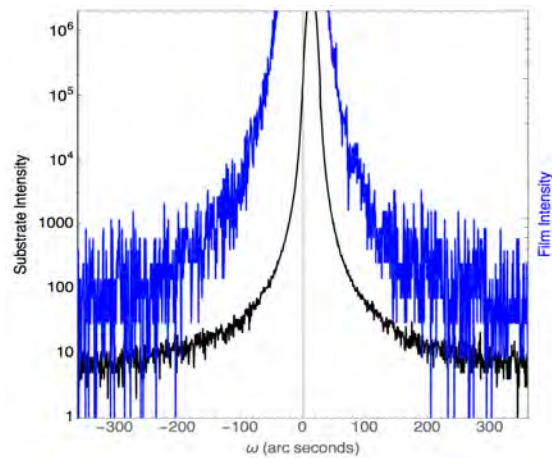


Figure 8- Computer analyzed Rocking Curve of Sr₃Ti₂O₇-(BaTiO₃) on DyScO₃ (100) substrate of ~50 nm thickness samples

-induced strain effect on our sample as well as generally a high defect density.⁶ In addition, the increased number of layers in each crystal, the $n = 2$ structure, is known to result in an increased number of defects, specifically

stacking faults to reduce the overall energy of the now larger structure.^{2,6} The discrepancy between the film and substrate peaks and slight shift in the film curve (Figure 8) could also be the result of increased defects due to the larger crystalline structure

Conclusion

After the successful generation and analysis of numerous $2\theta/\omega$ scans and a Rocking curve (ω scan) we were able to determine the existence of defects in our samples and note the effects they have on two different X-ray diffraction scans. In addition, we showed the value of the modified Williamson-Hall analysis technique in analyzing the size and defect induced strain of perovskite oxide thin films. In the future we hope to perform a full Williamson-Hall analysis on samples varying in substrate, film thickness, and lattice structure (addition of other metals like barium) to determine what factors are truly causing these common defects. Furthermore, we hope to use more sophisticated analysis techniques, such as the Warren-Averbach method, to separate the effects of size from defect-induced strain.⁶

Acknowledgments:

This work was supported by the Cornell Center for Materials Research with funding from the NSF MRSEC program (DMR-1120296)

1. Suzuki, T., Nishi, Y., & Fujimoto, M. (n.d.). *Defect Structure in Homoepitaxial Non-Stoichiometric Strontium Titanate Thin Films*.
<http://dx.doi.org/10.1080/01418610008212072>
2. Hudson, P. R., & Phakey, P. P. (n.d.). *Correlation Between Dielectric Constant and Defect Structure of Non-Stoichiometric Solid*
3. Li, H.-C., Si, W., Sirenko, A. A., Akimov, I. A., Fox, J. R., Clark, A. M., & Hao, J. (n.d.). *Oxide Thin Films for Tunable Microwave Devices*.
4. Tagantsev, A. K., Sherman, V. O., Astafeiv, K. F., Venkatesh, J., & Setter, N. (n.d.). *Ferroelectric Materials for Microwave Tunable Applications*. Moram, M. A., & Vickers, M. E. (n.d.). *X-Ray Diffraction of III-Nitrides*.
<http://dx.doi.org/10.1088/0034-4885/72/3/036502>
5. Schlom, D. G., Chen, L.-Q., Pan, X., Schmehl, A., & Zurbuchen, M. A. (n.d.). *A Thin Film Approach to Engineering Functionality into Oxides*.
<http://dx.doi.org/10.1111/j.1551-2916.2008.02556.x>
6. McLaurin, M. B., Hirai, A., Young, E., Wu, F., & Speck, J. S. (n.d.). *Basal Plane Stacking-Fault Related Anisotropy in X-ray Rocking Curve Widths of m -Plane GaN*.
<http://dx.doi.org/10.1143/JJAP.47.5429>

Electrical Characterization of Iridium Oxide Thin Films

Eric Bigenwald¹, John T. Heron^{2,3}, Jason Kawasaki^{2,3}, Darrell Schlom^{2,3,4}

¹*Department of Physics, University at Buffalo (SUNY), Buffalo, NY 14261;* ²*Department of Materials Science and Engineering, Cornell University, Ithaca, NY 14853;* ³*Cornell Center for Materials Research, Ithaca, NY 14853;* ⁴*Kavli Institute at Cornell for Nanoscale Science, Ithaca, NY 14853*

I. Abstract

Due to the rapid advance of modern technology, researchers are constantly looking for new ways to improve electronics and new applications for them. This has driven scientists to go beyond common semiconductors, such as silicon, and search for new materials with exciting properties. One area of research is in complex oxides, which have strong electronic correlations that are the root cause of numerous exotic physical phenomena. Due to its electron-electron correlations and a large spin-orbit interaction (~500 meV), the band structure and its filling in iridium oxide (IrO₂) gives rise to exotic electronic features in this material. It is anisotropic, conductive and metallic, which separates it from almost all other oxides [1]. Here we electrically characterize thin films (6 – 40 ML) of IrO₂, grown on (110) oriented titanium dioxide by molecular beam epitaxy, by resistivity and Hall effect measurements from 300 K to 5K. The results illustrate the anisotropic nature of iridium oxide, as well as its conductive nature and a switch in the sign of the slope of the carrier density versus temperature that could be related to intrinsic, thickness dependent, band structure changes of IrO₂ on TiO₂.

II. Introduction

To continue the pace of improvement in semiconductor technology, researchers have left traditional semiconductors behind and investigating new materials that may have desirable electronic or magnetic properties. This had led many to oxides, which exhibit various properties caused by powerful electron-electron correlations. In addition, altering these oxides, either through doping, strain, or layering them with other oxides (Dr. Schlom's "nanosandwiches")[2] can cause other phenomena to appear that are not found in the bulk oxide crystal [3,4]. These properties, often not found in traditional semiconductors, range from different types of conducting behavior (insulating, metallic, or semiconducting), to ferroelectricity (and tunable dielectrics), to (anti)ferromagnetism, anisotropic magnetoresistance, and more [5,6]. The wide range of novel properties make for exciting and rewarding research in oxides, as well as provide an abundance of possibilities for electronic or electrochemical applications [7]. Iridium oxide, for instance, has possible applications in pH-sensing electronics [8], chlorine, ammonia, or oxygen

evaluation [9,10,11], neural stimulation [12,13], field emission displays, and advanced memory technologies [14]. The myriad applications for iridium oxide thin films have necessitated further research on them.

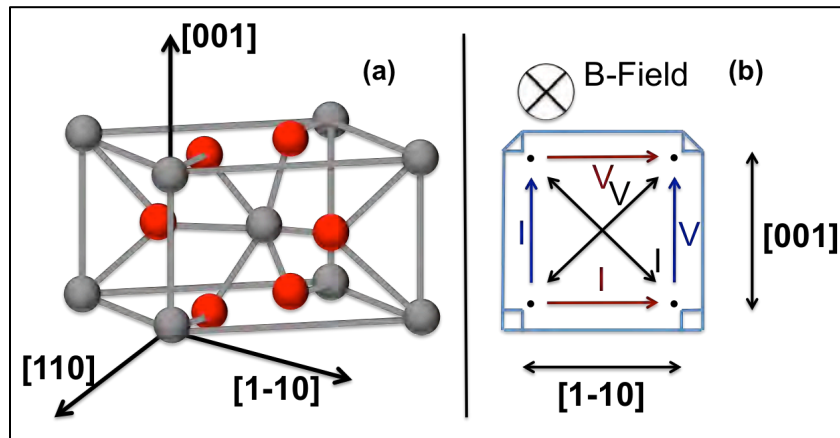


Figure 1(a): Iridium oxide crystal structure. Iridium is grey and oxygen is red. Figure 1(b): Top view of sample.

There are several deposition techniques that enable the growth thin films, one of which is molecular beam epitaxy (MBE). MBE is characterized by its slow growth/deposition rates and high levels of accuracy, control, and quality [15]. In MBE, a substrate is held still in a central chamber under ultra-high vacuum (less than 10^{-8} Pa) [16]. The

elements that are used to make the thin film are heated to gaseous form and held individually in smaller chambers, separated from the central chamber by a shutter and directed at the substrate. When the shutter is opened, the element disperses into the central chamber, where atoms can travel for long distances—the mean free path of the atoms is high, due to the vacuum in the chamber. The atoms of the desired element flow in a beam toward the substrate, where they combine and form a layer on top of the substrate. The thickness of the layer can be controlled by opening and closing the shutter at precise intervals using a computer. So not only can the growth and thickness of the thin film be controlled down to the atomic level, MBE also allows for real-time feedback on the quality of the thin film. Reflection High-Energy Electron Diffraction (RHEED) is a technique that can be used during the MBE growth process to characterize the thin film's surface. By determining what the surface looks like, researchers can quickly determine the roughness of the film's top layer and thus the quality of the film.

The Van der Pauw method is used to calculate the resistivity of a sample, and can also be used to determine the carrier density, mobility, and Hall coefficient. Carrier density, the number of charge carriers (electrons or holes) per unit volume, is measure in $(\text{carriers}) \cdot \text{cm}^{-3}$ for semiconductors. Mobility, a determinant of how quickly an electron or hole can move through a semiconductor when under an electric field, has units of $\text{cm}^2/(\text{V}\cdot\text{s})$. Mobility times the applied electric field gives the drift velocity of the electrons in the semiconductor. For semiconductors, mobility is dependent on amount of doping, the quality of the semiconductor, temperature, and the carrier density itself. Carrier density and mobility are two of the many parameters for electrically characterizing semiconductors. Conductivity is proportional to the product of mobility and carrier density, and thus the same conductivity will be achieved with a low carrier density and high mobility as with a high carrier density and low mobility. However, many devices

that utilize semiconductor materials perform better with higher mobility, making mobility the more important parameter of the two.

For a square sample, wired contacts are done as close to the four corners as possible. Current and voltage are measured on opposite sides running parallel, and a resistance can be measured, one for the vertical direction (R_{001}) and one for the horizontal direction (R_{1-10}) [17,18]. The Van der Pauw equation can then be used to calculate the sheet resistance of the thin film— and by multiplying it by the film's thickness, the resistivity can be determined. The current and voltage can also be measured diagonally (perpendicular to each other) to calculate the size of the Hall effect by also applying an external magnetic field. All of the results can then be used together to determine the carrier density, mobility, and Hall coefficient for the thin film. This is all depicted in Figure 1(b).

The thin film can also be patterned with Hall bars for further research and investigation. The Hall bars are patterned onto the film by optical lithography, and wires are bonded to the ends of a Hall bar. Depending on how that particular Hall bar is oriented, resistivity and the Hall effect can be measured on one particular axis. This differs from the above, non-patterned situation as in this case the current can only flow in one direction— down the Hall bar. This allows for the testing of anisotropy as the Van Der Pauw method require isotropic behavior to be accurate.

III. Methods

All the iridium oxide samples tested were grown in Dr. Schlom's lab, in the MBE chamber by Jason. He then structurally characterized them using X-Ray Diffraction (XRD) and Angle-Resolved Photoemission Spectroscopy (ARPES) to ensure the quality of the samples.

For each unpatterned sample for Van der Pauw measurement, the process was as follows: the sample was cleaned by immersing it in acetone and then isopropanol. Using double-sided tape, it was attached to the resistivity puck, a device that enables current to be run through the sample. Alignment of the sample was consistent in all samples, and the current was kept at a constant $150\mu\text{A}$. Once the sample was attached, wires were bonded. This was done using a Kulick & Soffa manual wire bonder, a machine contained in the CCMR Shared Research Facilities. At this point, with the sample correctly wired, the thin film could now be tested.

The sample was placed into a Quantum Design Physical Properties Measurement System (PPMS). Horizontal and vertical resistances were measured along the [1-10] and [001] axes from 300K to 5K. Next, Hall effect measurements were made at 5K, 10K, 50K, 100K, 150K, 200K, 250K, and 300K, applying an external magnetic field that scanned from -6 T (-60000 Oe) to +6 T (60000 Oe) at each desired temperature. After the Van der Pauw characterization, John patterned the 40ML sample by optical lithography. Using the newly patterned Hall bars, the measurement was repeated twice more, once with a Hall bar along the [1-10] axis and another along [001].

Sheet resistance was determined using MATLAB to numerically solve the Van der Pauw equation, and then the film's resistivity was calculated from the sheet resistance and plotted versus temperature (5K to 300K). For the Hall effect data, resistance versus applied external magnetic field was plotted for each temperature, and Igor Pro (used for all other data analysis and plots) was used to find the coefficients for a linear best-fit line. The slope of this line, along with relevant equations involving the Van der Pauw method and the Hall effect, was utilized to calculate sheet carrier density, (volume) carrier density, mobility, and the Hall coefficient. All of these parameters were plotted versus temperature. A plot of resistance versus $1/(\text{sample thickness})$ was made at both 300K and 10K.

IV. Discussion of the Results

All the relevant plots are at the end of this paper, instead of wrapping the text around the plots.

Unpatterned Samples

In the resistivity plot, the resistivity of all four samples decreases with decreasing temperature, and largely decreases with increasing thickness. The 8ML sample has a resistivity less than the 6ML sample, across all temperatures, but that could be due to surface roughness. For IrO_2 , the 2ML difference in samples is equivalent to 0.6365 nm, which is small enough that the difference in surface roughness of the two samples could cause the 8ML sample to be more resistive.

The carrier densities are slightly noisy, but illustrate that, as temperature increases, 40ML and 12ML carrier densities decrease while the 8ML and 6ML densities increase. The opposite is true for the Hall coefficients—the 40ML and 12ML coefficients increase with temperature while the 8ML and 6ML coefficients decrease. Clearly, there is some thickness, between 8ML and 12ML, where the sign of the slope of both plots switches. This was unexpected, and is a goal for future research. It is currently unclear if this is related to band structure changes caused by structural relaxation thickness of the IrO_2 on TiO_2 or something more intrinsic. In Jason's ARPES (Angle-reflective photoemission spectroscopy) plots, there is a 'side band' seen at lower thicknesses that slowly disappears as the sample thickness increases. We are uncertain whether this is related to the switching sign of the carrier densities.

Mobility decreases with increasing temperature, and it generally increases with increasing thickness, though once again the 8ML and 6ML samples are switched. Mobility values range from 18 to $1 \text{ cm}^2/(\text{V}\cdot\text{s})$, which are low for a metallic compound but quite high for an oxide.

Patterned Samples

These graphs (Figures 11-13) illustrate the anisotropic nature of iridium oxide. The resistivity differs along the [1-10] and [001] axes, causing the mobility to also differ by 5 to $10 \text{ cm}^2/(\text{V}\cdot\text{s})$.

V. Conclusion

IrO₂ thin films were found to be more conductive than most oxides, with higher mobility values as expected. The samples also exhibited the expected metallic behavior, with resistivity decreasing with decreasing temperature. Thicker samples generally had higher resistivity values, and the 6ML sample having a higher resistivity than the 8ML sample could be due to surface roughness. The sign of the slope in the graphs of carrier density vs. temperature switches at a thickness between 8ML and 12ML, and could be due to the relaxation thickness. For the patterned versus non-patterned plots, it can be clearly seen that iridium oxide is anisotropic in nature, will a large difference in resistance measured along perpendicular crystal planes. Areas of further research include determining whether this switch in sign is intrinsic or related to the side band disappearance seen in the ARPES data, as well testing samples of other thicknesses.

VI. Acknowledgements

We would like to thank the NSF MRSEC program (DMR-1120296) and the REU Site Program (DMR-1063059) for funding the REU program, along with the Cornell Center for Materials Research. This work was supported by the Cornell Center for Materials Research with funding from the NSF MRSEC program (DMR-1120296). This work made use of the Cornell Center for Materials Research Shared Facilities, which are supported through the NSF MRSEC program (DMR-1120296).

VII. References

1. M. Kawasaki *et al.*, "Field Direction Control of A Type Charge Carriers in Non-Symmorphic IrO₂", *Physics Review B*, 2015.
2. Schlom, Darrell G. "Thin Film Alchemy: Creating Astonishing Properties in Nanosandwiches." 9 July 2015 at Cornell University.
3. J. H. Haeni, P. Irvin, W. Chang, R. Uecker, P. Reiche, Y. L. Li, S. Choudhury, W. Tian, M. E. Hawley, B. Craigo, A. K. Tagantsev, X. Q. Pan, S. K. Streiffer, L. Q. Chen, S. W. Kirchoefer, J. Levy and D. G. Schlom, *Nature* **430**, 758-761 (2004).
4. A. Ohtomo and H. Y. Hwang, *Nature* **427**, 423-426 (2004).
5. F. Lichtenberg, A. Catana, J. Mannhart and D. G. Schlom, *Appl. Phys. Lett.* **60**, 1138-1141 (1992).
6. M. Dawber, K. M. Rabe and J. F. Scott, *Rev. Mod. Phys.* **77**, 1083-1130 (2005).
7. Jani Hämäläinen *et al.*, "Atomic Layer Deposition of Iridium Oxide Thin Films from Ir(acac)₃ and Ozone", *Chem. Mater.*, 2008.

8. Ges, I. A.; Ivanov, B. L.; Schaffer, D. K.; Lima, E. A.; Werdich, A. A.; Baudenbacher, F. J. *Biosens. Bioelectron.* **2005**, *21*, 248.
9. Yang, H.; Kang, S. K.; Choi, C. A.; Kim, H.; Shin, D. H.; Kim, Y. S.; Kim, Y. T. *Lab Chip* **2004**, *4*, 42.
10. Karthigeyan, A.; Gupta, R. P.; Scharnagl, K.; Burgmair, M.; Sharma, S. K.; Eisele, I. *Sens. Actuators, B* **2002**, *85*, 145.
11. Karthigeyan, A.; Gupta, R. P.; Scharnagl, K.; Burgmair, M.; Zimmer, M.; Sulima, T.; Venkataraj, S.; Sharma, S. K.; Eisele, I. *IEEE Sens. J.* **2004**, *4*, 189.
12. Slavcheva, E.; Vitushinsky, R.; Mokwa, W.; Schnakenberg, U. *J. Electrochem. Soc.* **2004**, *151*, E226.
13. Hungar, K.; Görtz, M.; Slavcheva, E.; Spanier, G.; Weidig, C.; Mokwa, W. *Sens. Actuators, A* **2005**, *123–124*, 172.
14. Nagel, N.; Constrini, G.; Lian, J.; Athavale, S.; Economicos, L.; Baniecki, J.; Wise, M. *Integr. Ferroelectr.* **2001**, *38*, 259.
15. D. G. Schlom, *APL Mat.* **3**, 062403 (2015).
16. D. G. Schlom and J. S. Harris, Jr., in *Molecular Beam Epitaxy: Applications to Key Materials*, edited by R. F. C. Farrow (Noyes, Park Ridge, 1995), pp. 505-622.
17. J. Banaszczyk, A. Schwarz, G. De Mey, L. Van Langenhove, *Wiley InterScience (online)*. 13 April 2010.
18. Van der Pauw, L. J. *Philips Res Repts* 1958, *13*, 1.

Plots of Results

ARPES Plots (from Jason)

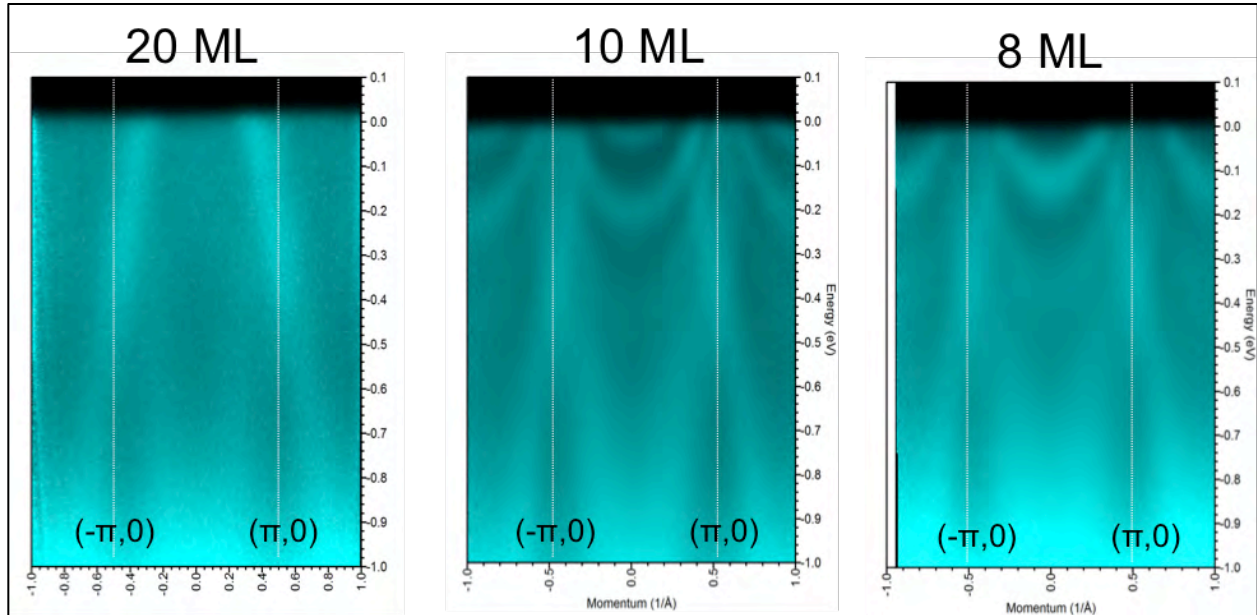


Figure 2. ARPES plots of thicker iridium oxide thin films. The side band structure clearly seen in the 8ML sample slowly disappears as the thickness increases.

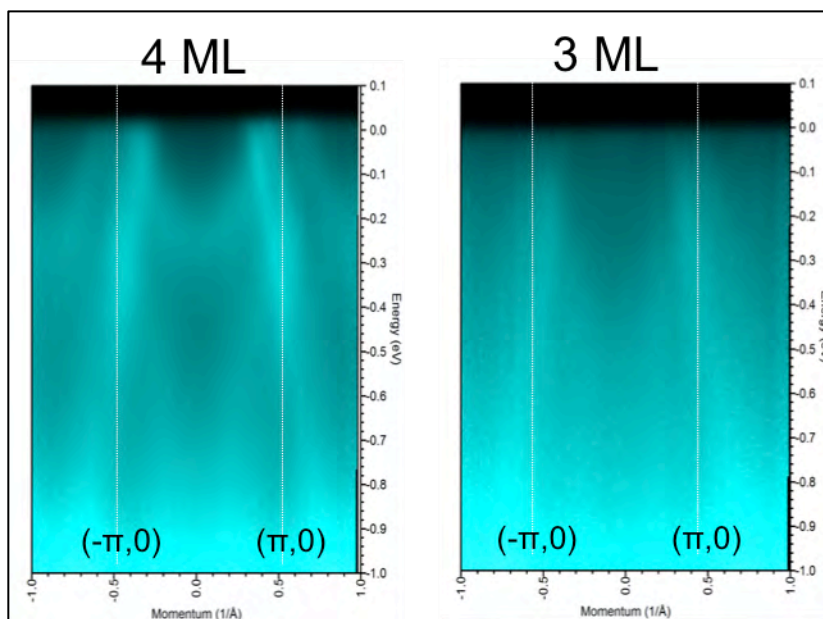


Figure 3. ARPES plots for thinner samples. Side band structure visible at 4ML.

Unpatterned Plots

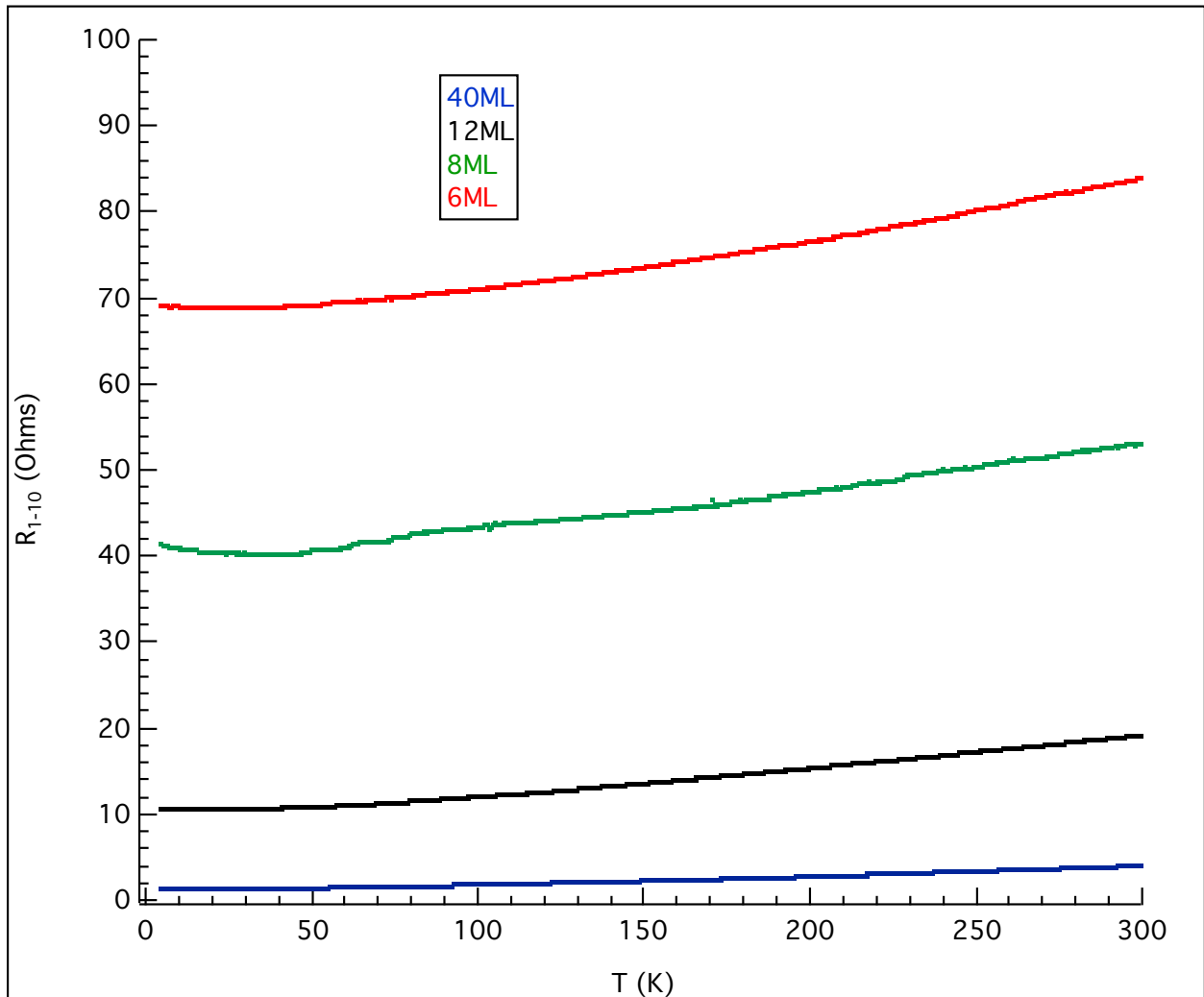


Figure 4. Resistance vs. Temperature along the [1-10] axis.

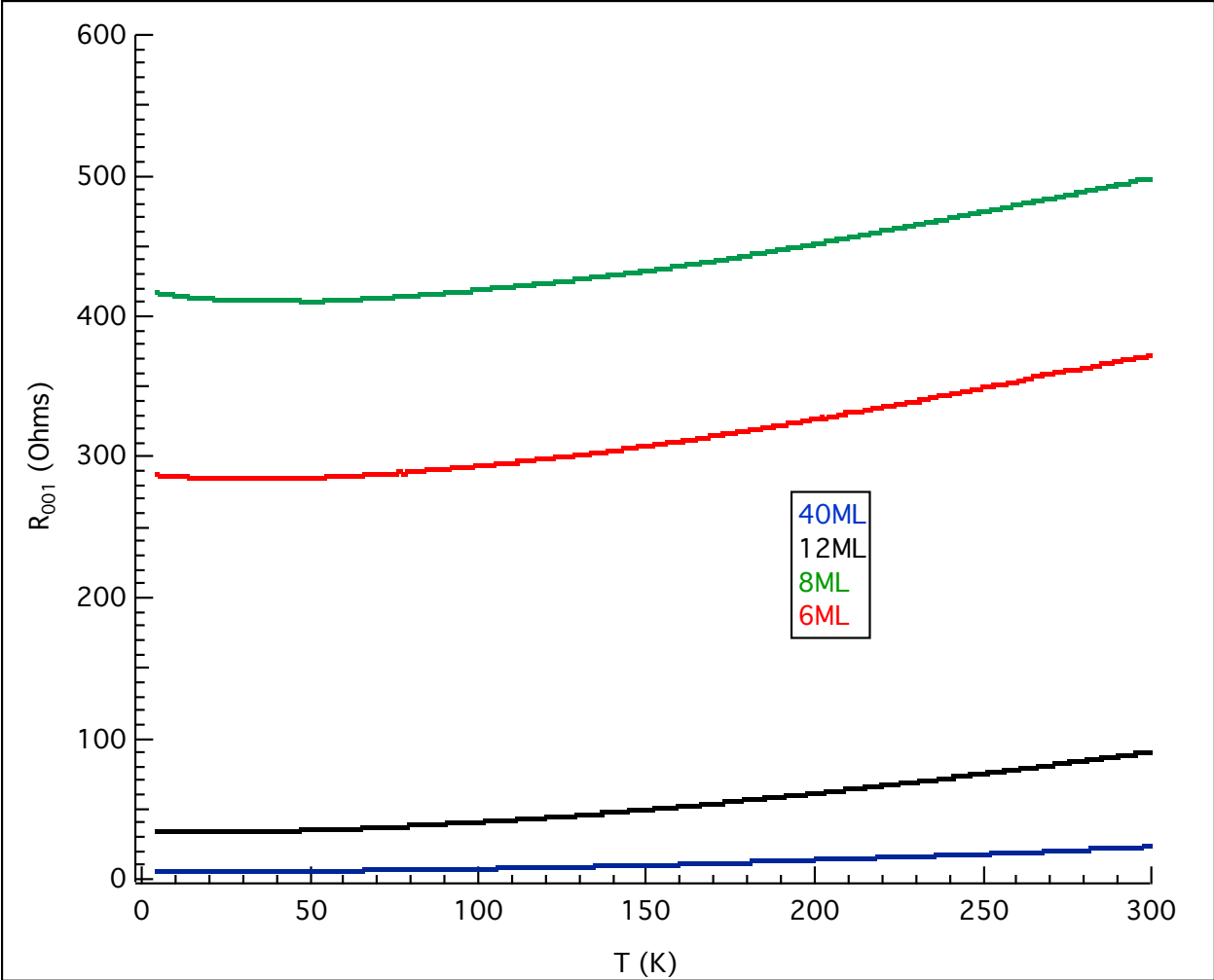


Figure 5. Resistance vs. Temperature along the [001] axis.

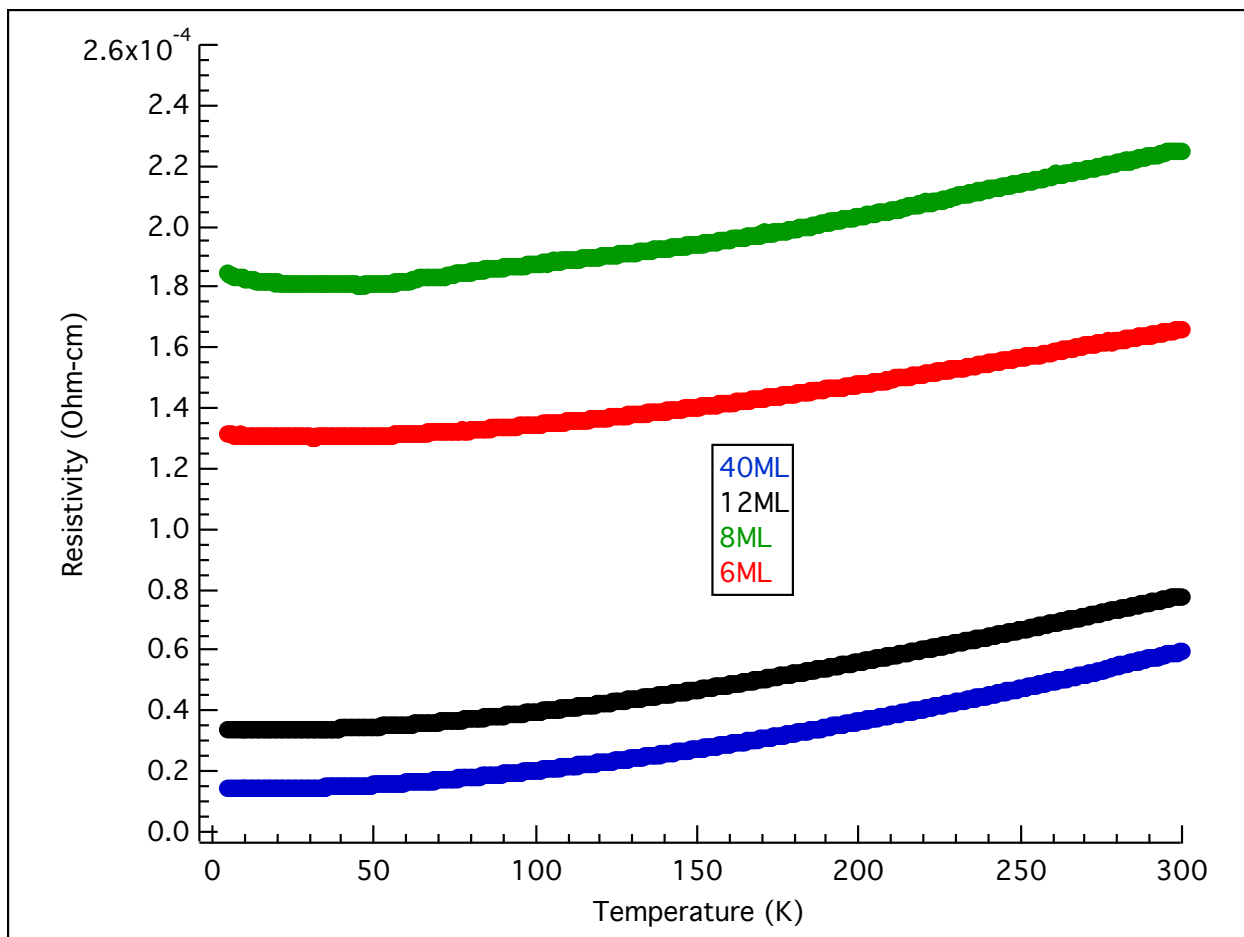


Figure 6. Resistivity vs. Temperature.

Note on Figure 6: This is the resistivity calculated from the Van der Pauw equation, which takes the resistances along the two axes and calculates the sheet resistance of the entire sample (which equals the resistivity divided by the thickness). However, the Van der Pauw equation is meant for isotropic samples, whereas our sample is clearly anisotropic—this means there is sizeable error in the resistivity values plotted above. Therefore, this graph is meant as a qualitative measurement of trends and a way to check the patterned results.

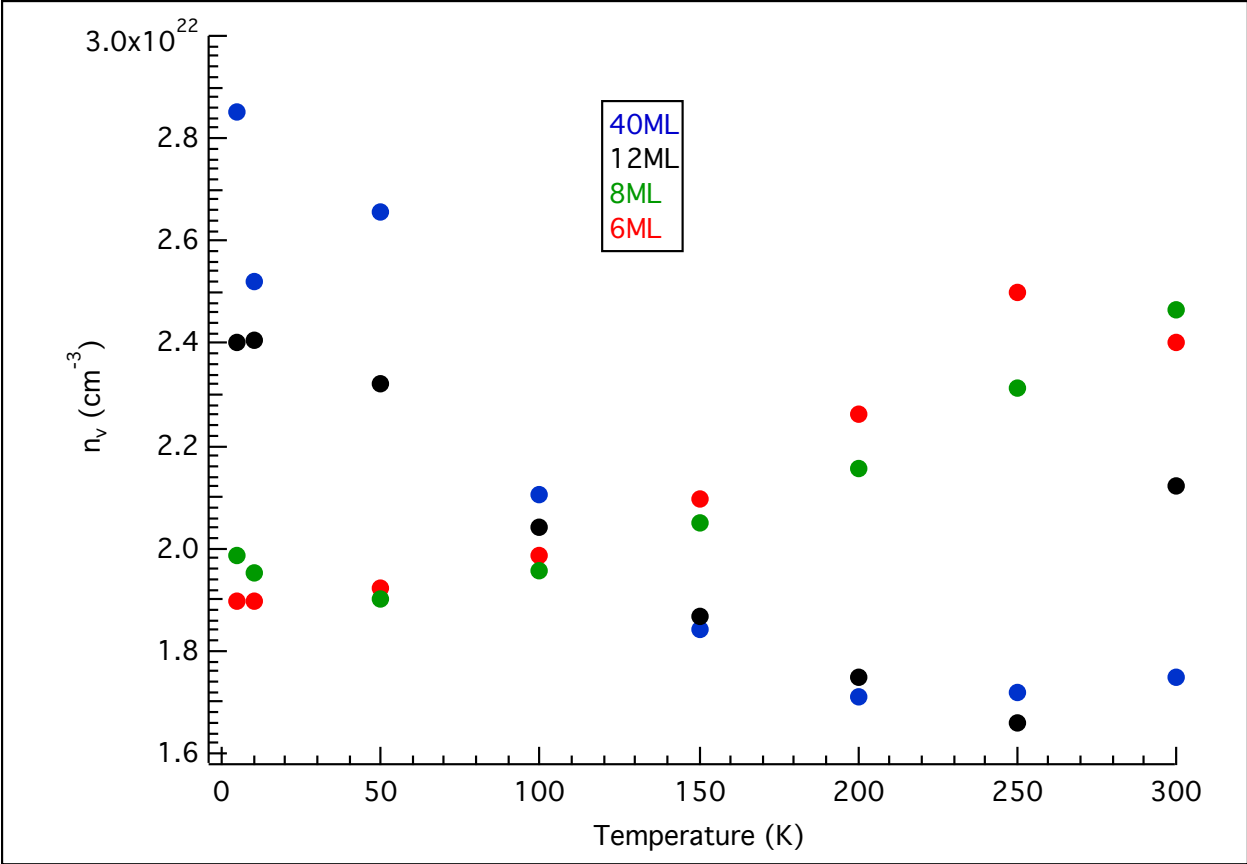


Figure 7. Carrier Density, n_v , vs. Temperature.

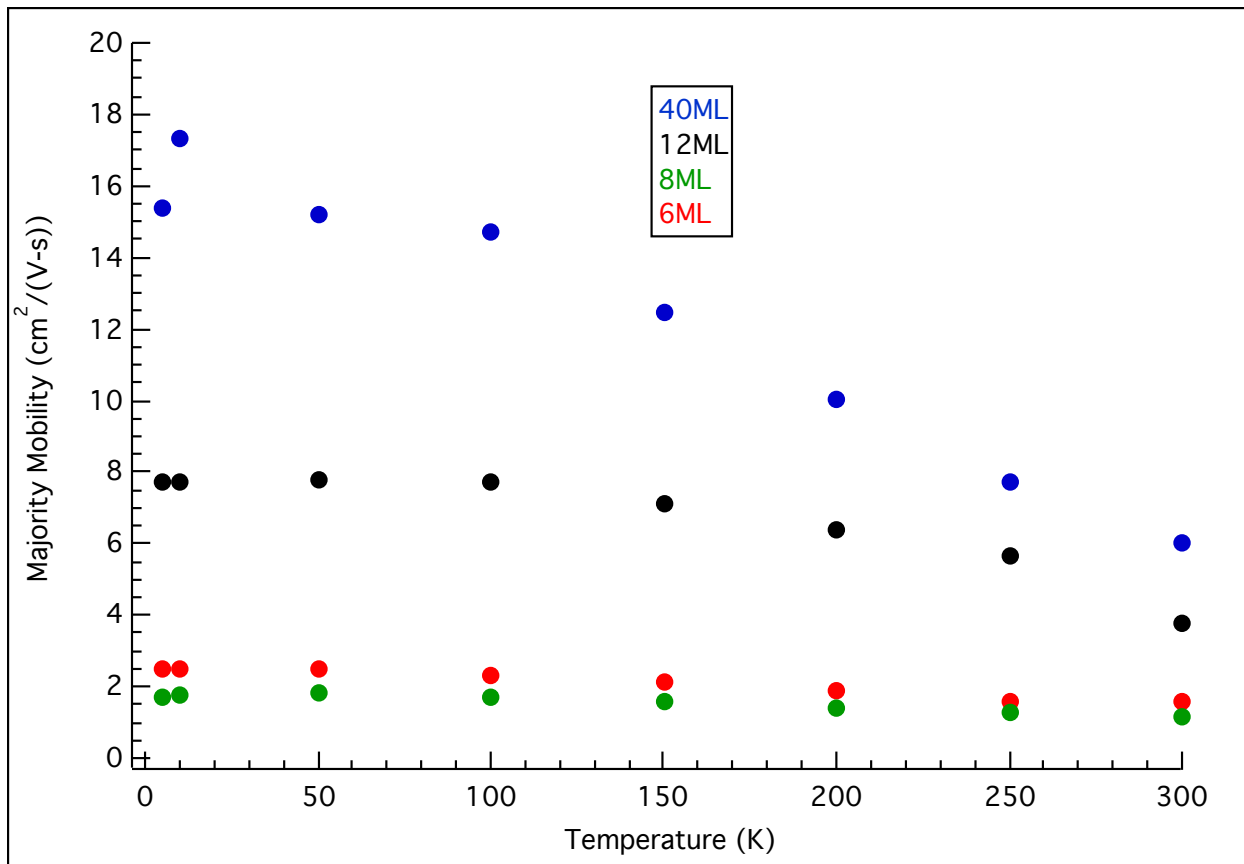


Figure 8. Majority Mobility vs. Temperature.

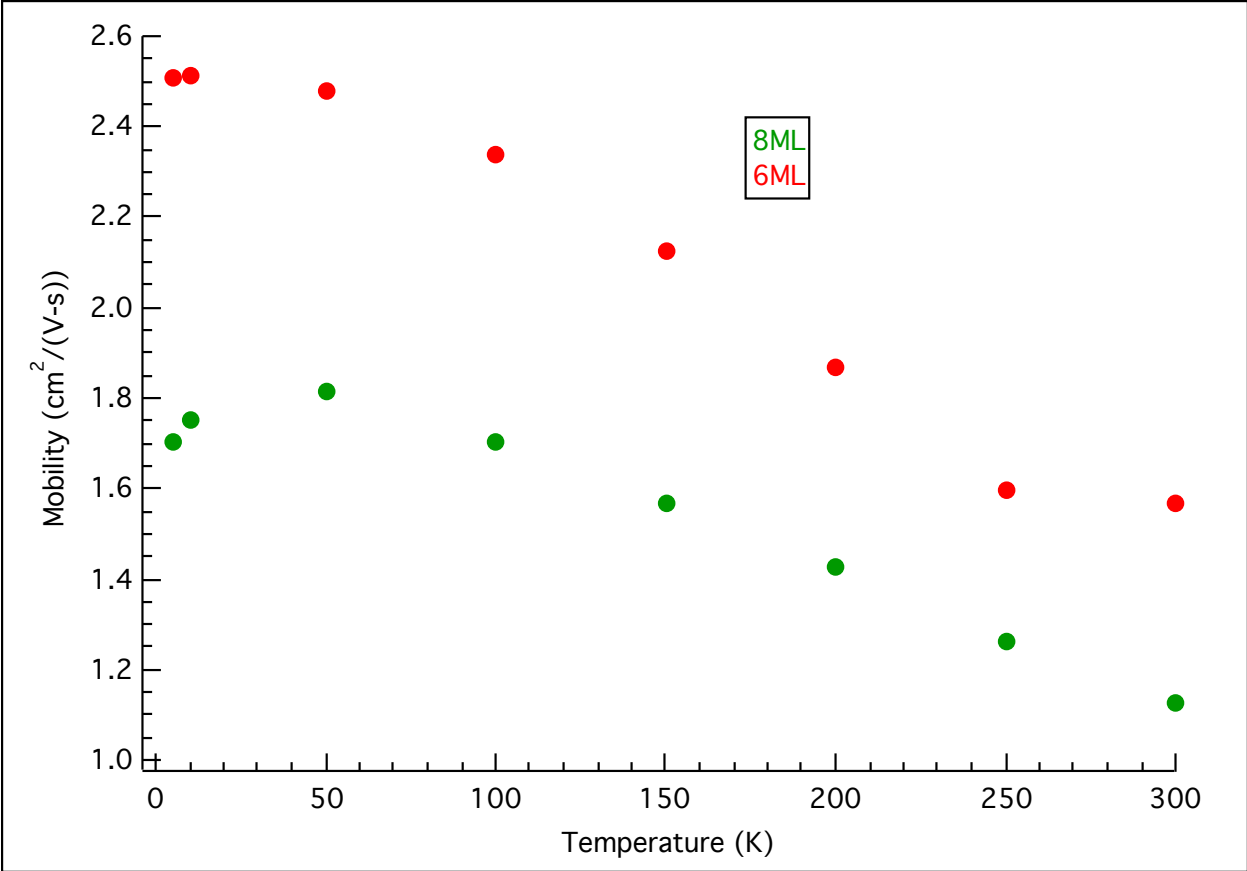


Figure 9. Magnified plot of Majority Mobility vs. Temperature.

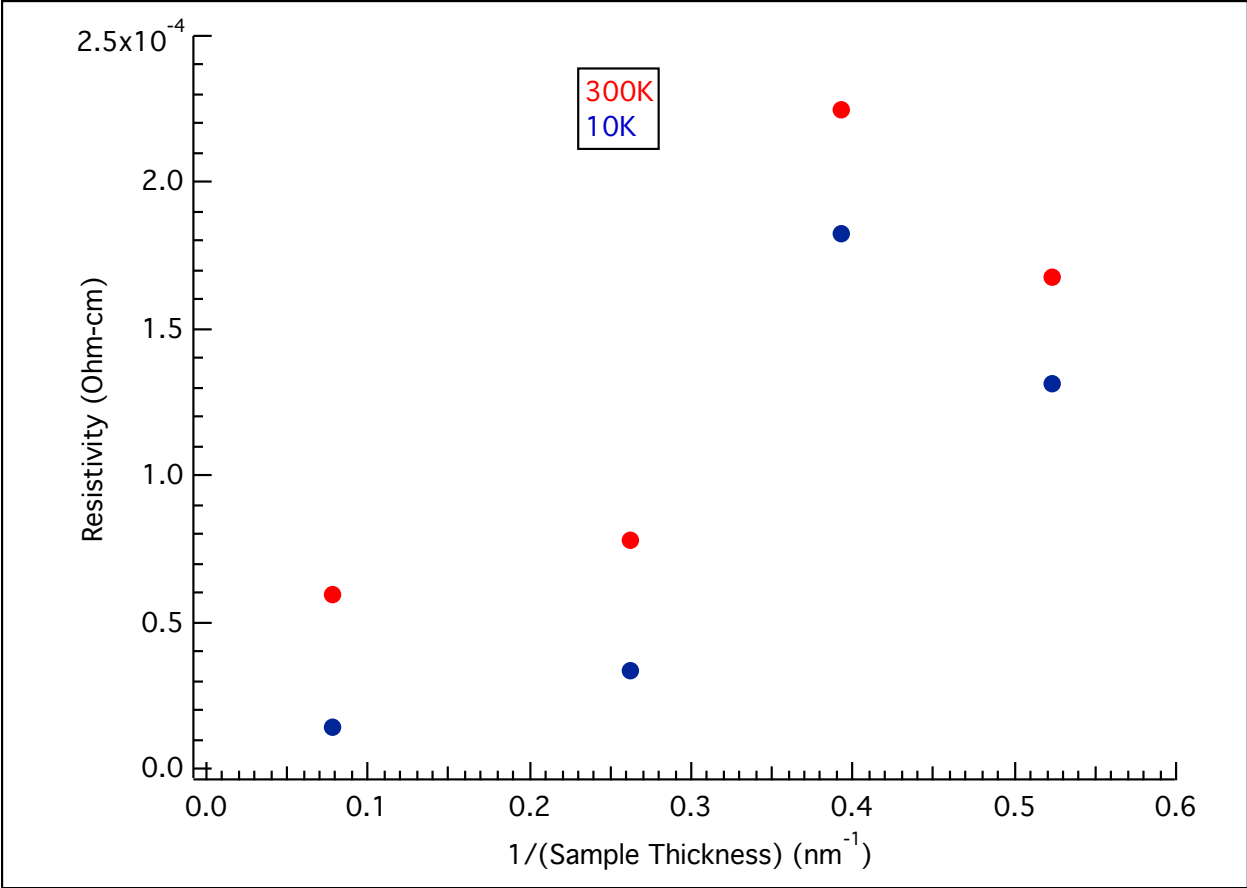


Figure 10. Resistivity vs. the reciprocal of the Thickness.

Patterned Samples

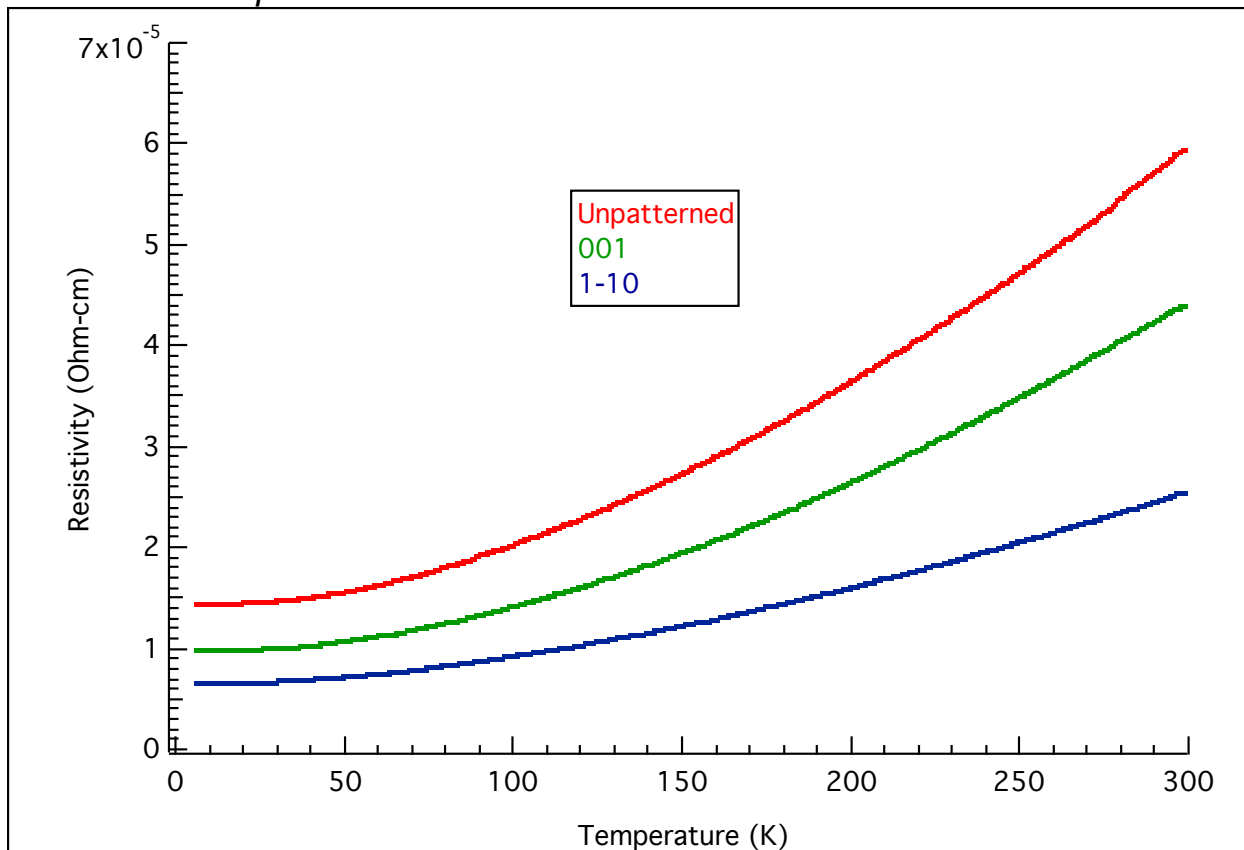


Figure 11. Resistivity vs. Temperature for the 40ML sample, both when non-patterned and when patterned with a Hall Bar along the given axis.

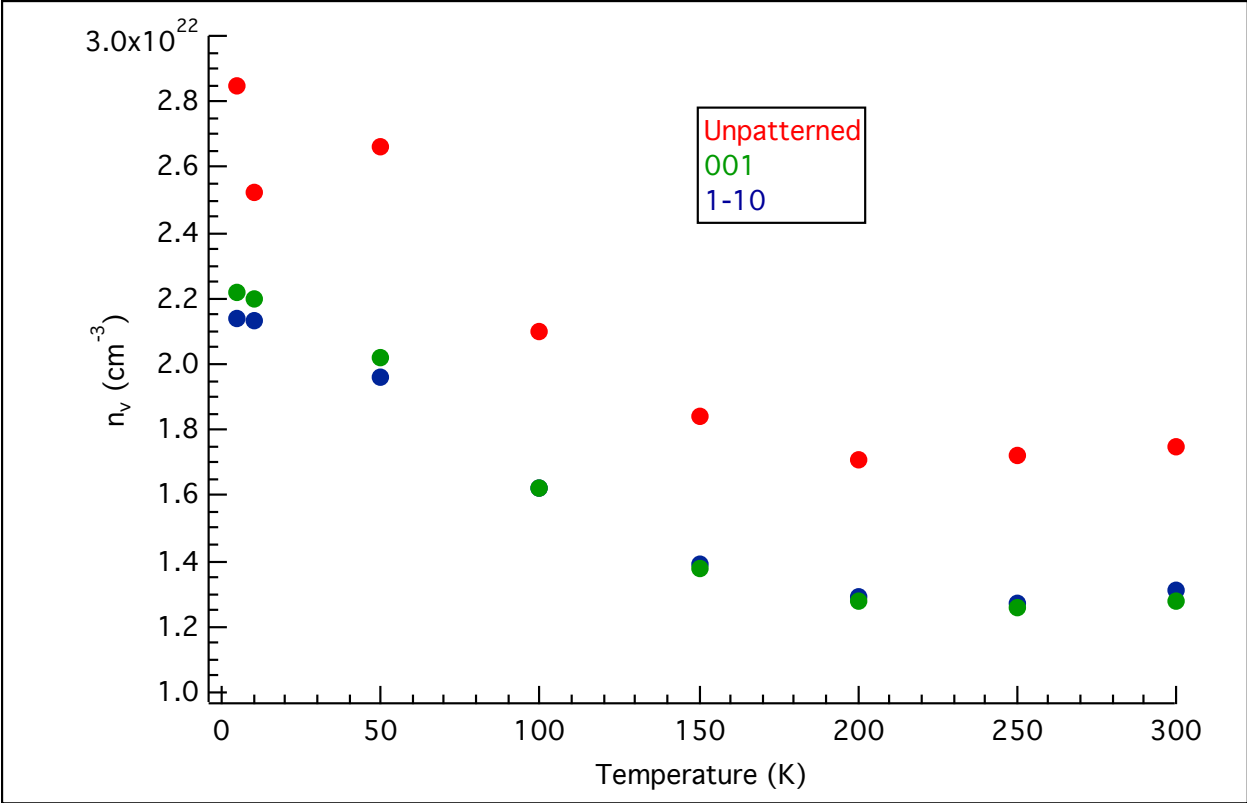


Figure 12. Carrier Density, n_v , vs. Temperature for the 40ML sample.

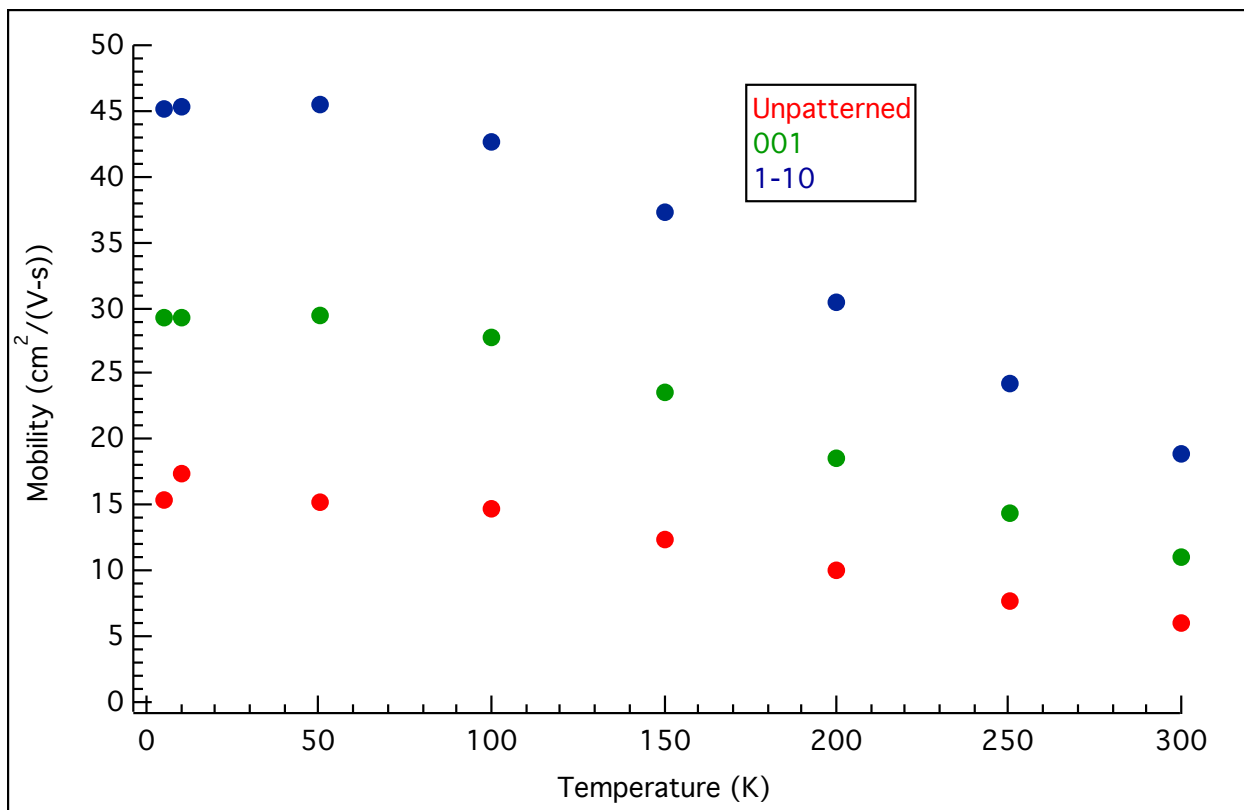


Figure 13. Mobility vs. Temperature for the 40ML sample.

Electropolishing Copper Foil

Conrad Blash

Abstract: In order to facilitate superior Boron Nitride growth via chemical vapor deposition, electropolishing of copper foil at elevated temperatures was attempted in order to eliminate copper roll and reduce rms roughness without causing pitting. The conditions of polishing that yielded the best results were 65°C in an electrolyte that consisted of 4.7M phosphoric acid with ethylene glycol added in to a concentration of 0.6g/mL with a current density of 190mA/cm² for 10 minutes on annealed copper that was approximately 127µm thick.

Introduction

In recent years, thin copper foil has found purpose as a substrate for the growth of thin films¹⁻⁵. However, the surface of most purchased copper foils are covered in line markings from machine rolling and other small defects^{6,7}. In order to optimize any film growth the substrate's surface should first be prepared⁶. Of the three more common methods of polishing copper foil, (mechanical, chemical-mechanical, and electrochemical⁶), electrochemical polishing, or electropolishing, is the simpler of the three, in terms of handling as opposed to using polishing machines, which aren't very compatible with copper foil⁸. In a recent study, it has been found that electropolishing at elevated temperatures, while staying within the kinetic regime of mass transfer limitation, or the current plateau in the anodic polarization curves⁹ (Fig. 2), is quite efficient in getting rid of manufacturer defects while preventing more defects from electropolishing, such as pitting, from forming⁷.

Procedure

With the exception of power source functionality tests, all experiments were done at elevated temperatures. Two main power sources were used to perform the experiments. A constant voltage source (Buehler Ltd., 1740 Micromet Etcher), and a constant current source (HP E3611A). With the exception of one trial, where 25 µm thick Cu foil was used, 127 µm thick Cu foil (Alfa Aesar) was used in all experiments. Samples were typically cut in rectangles of dimensions 1x2.5 cm and were always degreased before polishing. The degreasing was a three step process, starting with a bath in TCE (Trichloroethylene), then a bath in acetone and finally a bath in methyl alcohol as a the acetone solvent. All baths were done on a hot plate of temperature 100 °C and lasted 3 minutes. Some samples were also annealed after degreasing in order to increase grain size and better analyze the results of electropolishing (Fig. 6).

The electrolyte prepared for the experiments contained H₃PO₄ (Sigma Aldrich) at a concentration of either 4.7M or 7.6M, with ethylene glycol (Sigma Aldrich) added in to a concentration of 0.6g/ml as done by Kwon [31]. Two current densities were used in the experiments with the 1x2 cm of copper samples submerged in the electrolyte: 760mA and 30mA. The former was a value obtained from the recent study on electropolishing Cu⁷, and the second was a value obtained experimentally from graphing our own polarization curves (Fig. 2, Fig. 3). Both were values found in the plateau region of voltage vs. current polarization curves. The duration of the polishing was done in increments of 5 minutes with the

longest polishing at 90 minutes while using the constant voltage. With one exception, all experiments had the electrolyte heated to 65 °C. Rinsing of the Cu samples after electropolishing was done by full submersion in DI water for 1-2 minutes.

Results

From surface analysis via AFM, the initial RMS value of the copper was found to be around 170-180 nm (Fig. 4). Using the constant voltage source to achieve a current of 760 mA the RMS roughness actually increased. Visually, while some of the machine roll lines disappeared, the surface became quite inconsistent and darker in color, as if a layer of oxidation or some other substance had covered the surface (Fig. 7). It was believed that this was because polishing was not occurring in the appropriate polarization plateau for our etching device. After graphing the voltage vs. current curve, we found a plateau at much lower current and voltage values. Polishing was then done at these lower values only to find that while the surface showed slightly lower roughness (Fig. 7), but there was still no real improvement over the controls and the initial polishing, in all forms of analysis.

Several other adjustments were made in order to reduce roughness including changing the geometry of the electrolytic cell and agitating the electrolyte. The change in geometry made the counter electrode parallel to the sample being polished. This simply reduced roughness on one side slightly while the side that faced the counter electrode became extremely damaged due to inconsistency in polishing. Agitating the electrolyte served well in increasing the current to voltage ratio. However, after testing annealed samples in these conditions we gained results identical to the surface controlled kinetics region of the polarization curve⁷ (Fig. 8).

In order to obtain results comparable to the to the recent study's results from polishing in the plateau of the polarization curve, the power source was changed from one of constant voltage to one of constant current. Also, annealed samples were the main samples used with the constant current source. After polishing the annealed samples at the two currents primarily used before, the lower current of 30 mA showed surface controlled kinetics like before, with varying roughness on each individual grain, while the higher current of 760 mA showed results almost identical to mass transport controlled region or the polarization plateau⁷ (Fig. 8), with a roughness of around 12 nm when polished for 5 to 10 minutes (Fig. 5).

In terms of thickness of Cu, the constant voltage source polishing was slow with 5-10 being polished off even after 90 minutes. Conversely, the constant current source etched the copper at a rate of around 3.5 μm per minute, with the Cu completely dissolving into solution after 35 minutes.

Conclusion

In conclusion, while the final RMS value was quite low, it was probably not the optimal value, as there was a low amount of pitting that formed, possibly due to slight gas formation. It was not tested if room temperature polishing or if temperatures higher than 65 °C made a difference overall when using the constant current source, but it did not make a difference when using the constant voltage source. And while the samples did come out relatively smooth (Fig. 9) it was found out after BN was grown on several that there was slight contamination on the surface that was not visible. This means that the rinsing and storing process might also need to be built upon. Overall this copper polishing process has room for improvement.

Acknowledgements

Hussain Als Salman, Yanxin Ji, Lori Lepak, Jeonghyun “Jeff” Hwang, Brian Calderon, John Grazul, and Michael Spencer.

References

1. Luo, Z. *et al.* Effect of Substrate Roughness and Feedstock Concentration on Growth of Wafer-Scale Graphene at Atmospheric Pressure. 1441–1447 (2011).
2. Zhang, B. *et al.* Low-Temperature Chemical Vapor Deposition Growth of Graphene from Toluene on Electropolished Copper Foils. 2471–2476 (2012).
3. Graphene, S. *et al.* Toward the Synthesis of Wafer-Scale. 9110–9117 (2012).
4. Wu, T. *et al.* Triggering the Continuous Growth of Graphene Toward Millimeter-Sized Grains. 198–203 (2013). doi:10.1002/adfm.201201577
5. Vlassiuk, I. *et al.* Large scale atmospheric pressure chemical vapor deposition of graphene. *Carbon N. Y.* **54**, 58–67 (2012).
6. Han, G. H. *et al.* Influence of Copper Morphology in Forming Nucleation Seeds for Graphene Growth. 4144–4148 (2011).
7. Kwon, G. D. *et al.* Controlled electropolishing of copper foils at elevated temperature. *Appl. Surf. Sci.* **307**, 731–735 (2014).
8. Bae, S. *et al.* Roll-to-roll production of 30-inch graphene films for transparent electrodes. **5**, 1–5 (2010).
9. Landolt, D. REVIEW ARTICLE FUNDAMENTAL ASPECTS OF ELECTROPOLISHING. (1987).

Figures

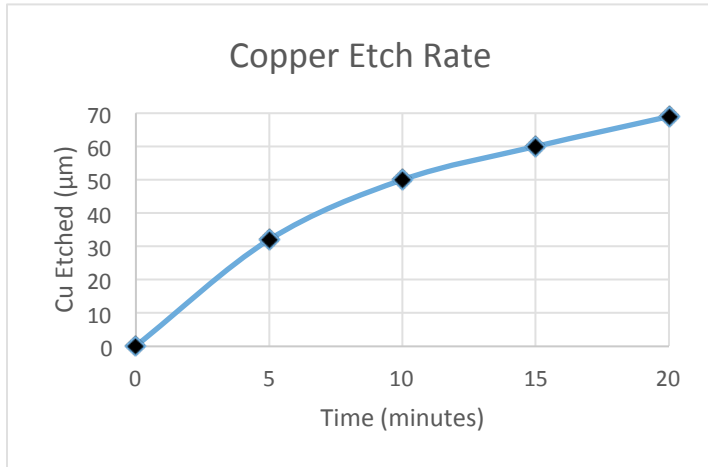


Fig. 1

During the first five 5 minutes of etching, a large amount of Cu is etched from the surface however the rate at which copper etched slowly decreased over time.

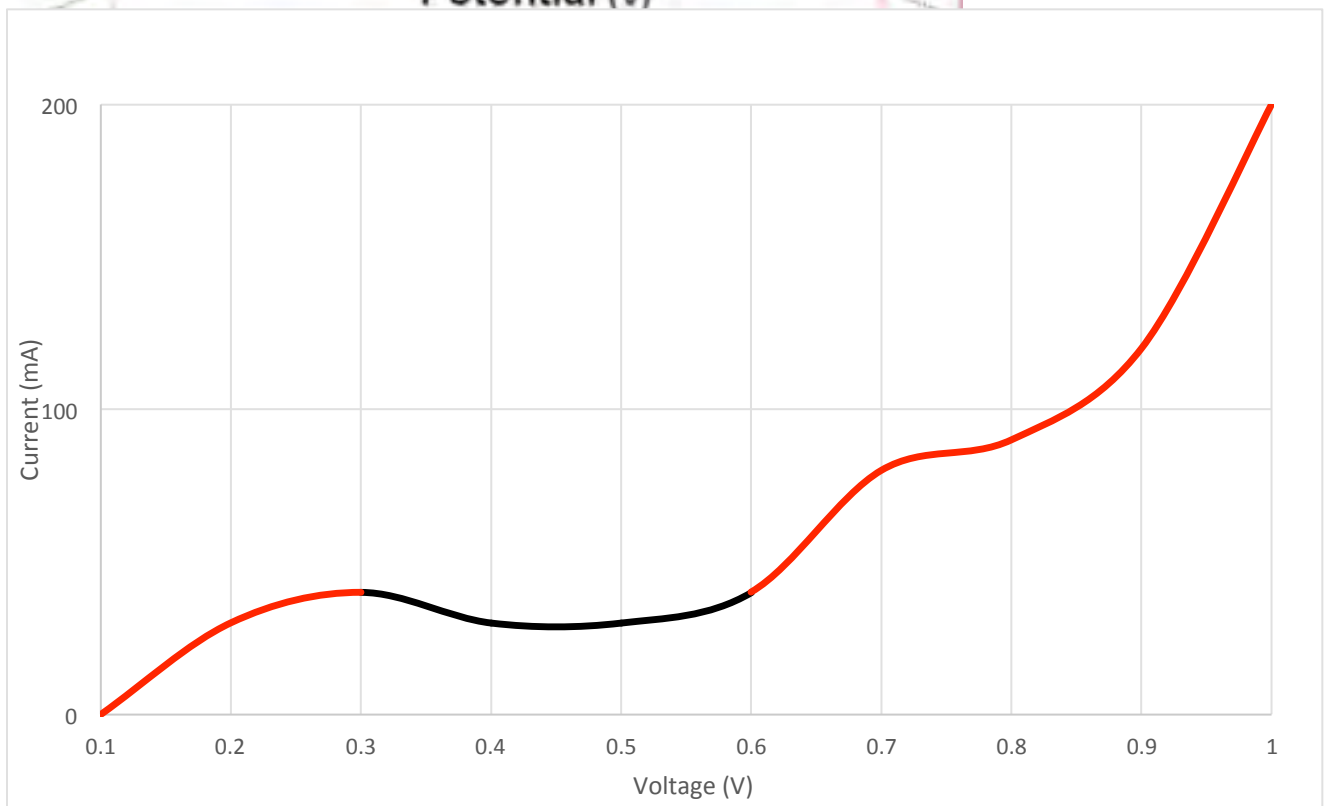
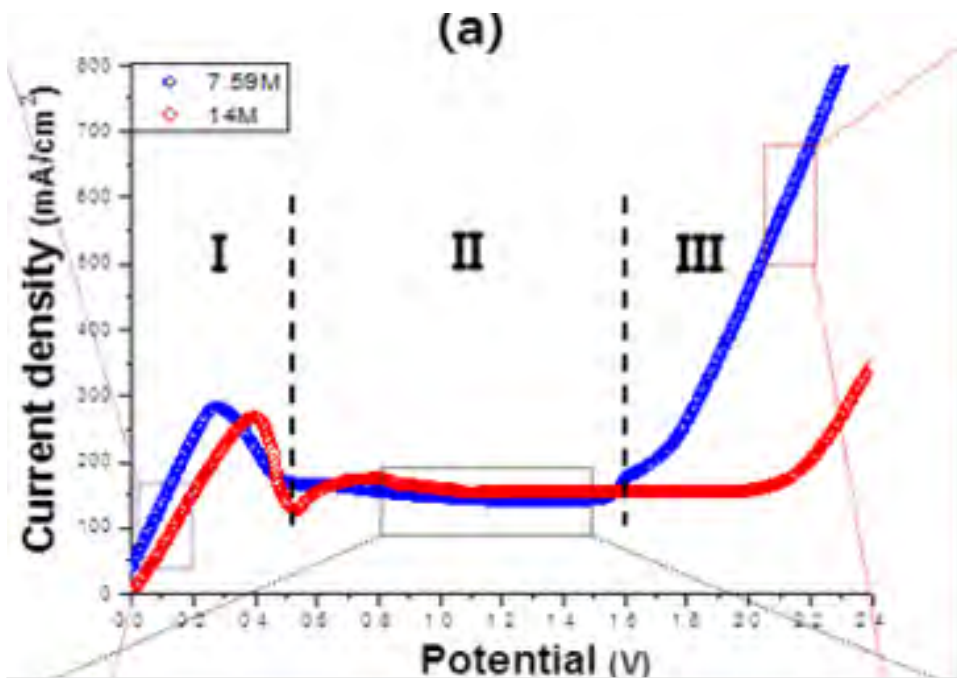


Fig. 2 and 3

Our graph of voltage vs. current (Lower) was very different from the one found in the recent study (Upper⁷). However, both seemed to have somewhat of a plateau region. The darkened area on our graph is what we believe to be our plateau.

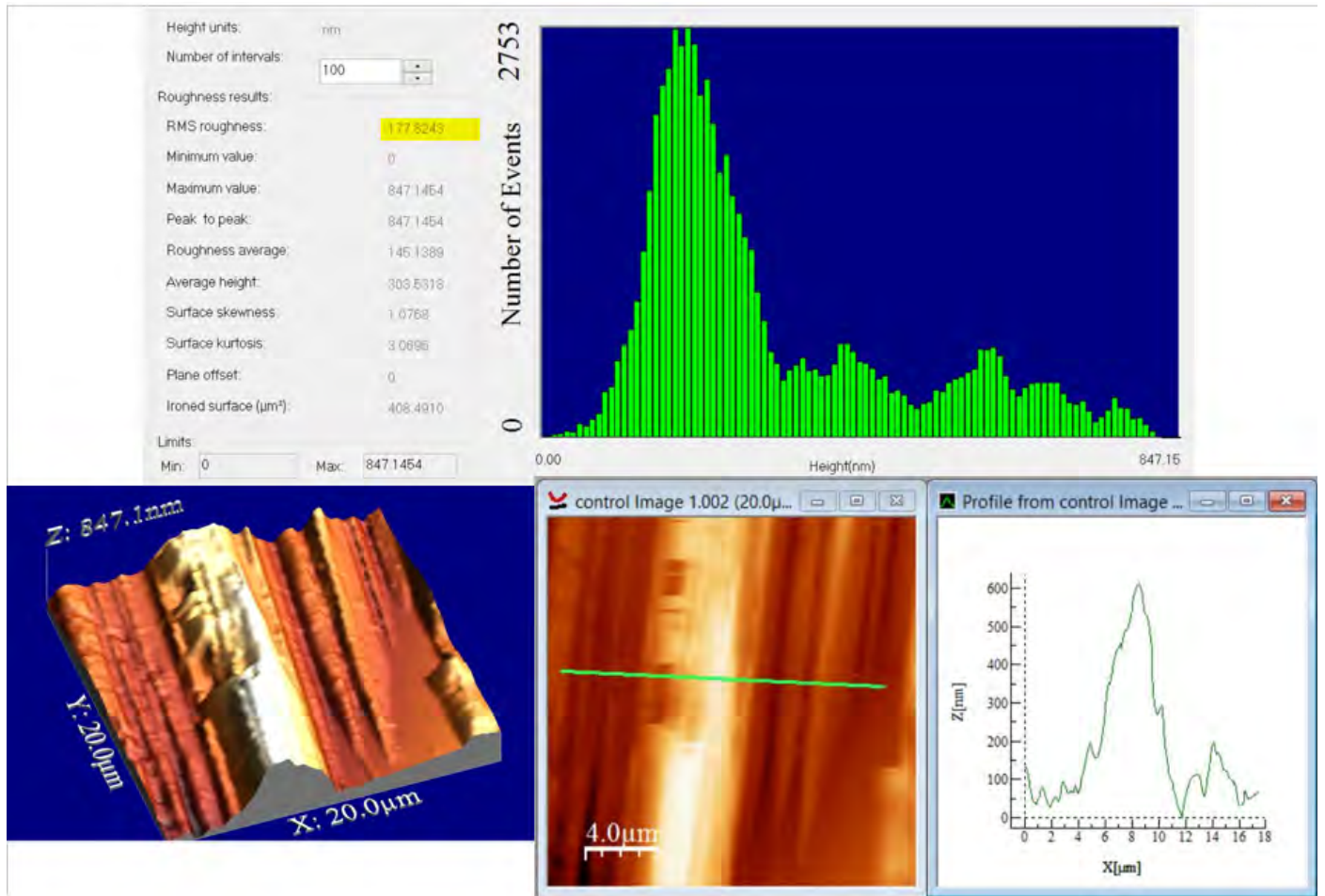


Fig. 4

AFM data on unpolished copper. The RMS of approximately 177 is highlighted.

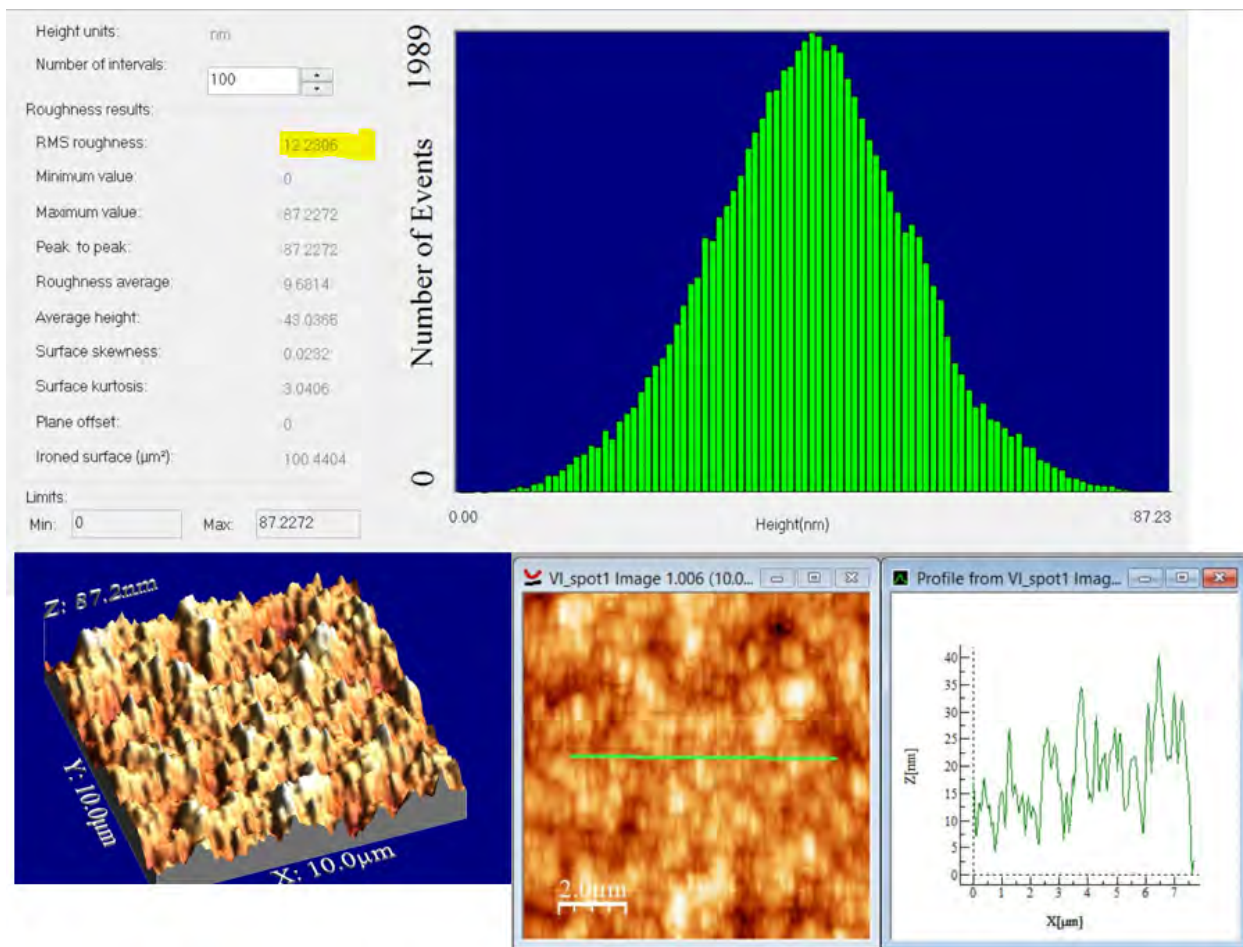


Fig. 5

AFM data on Cu polished with Constant current source at 760 mA. RMS of 12 is highlighted.

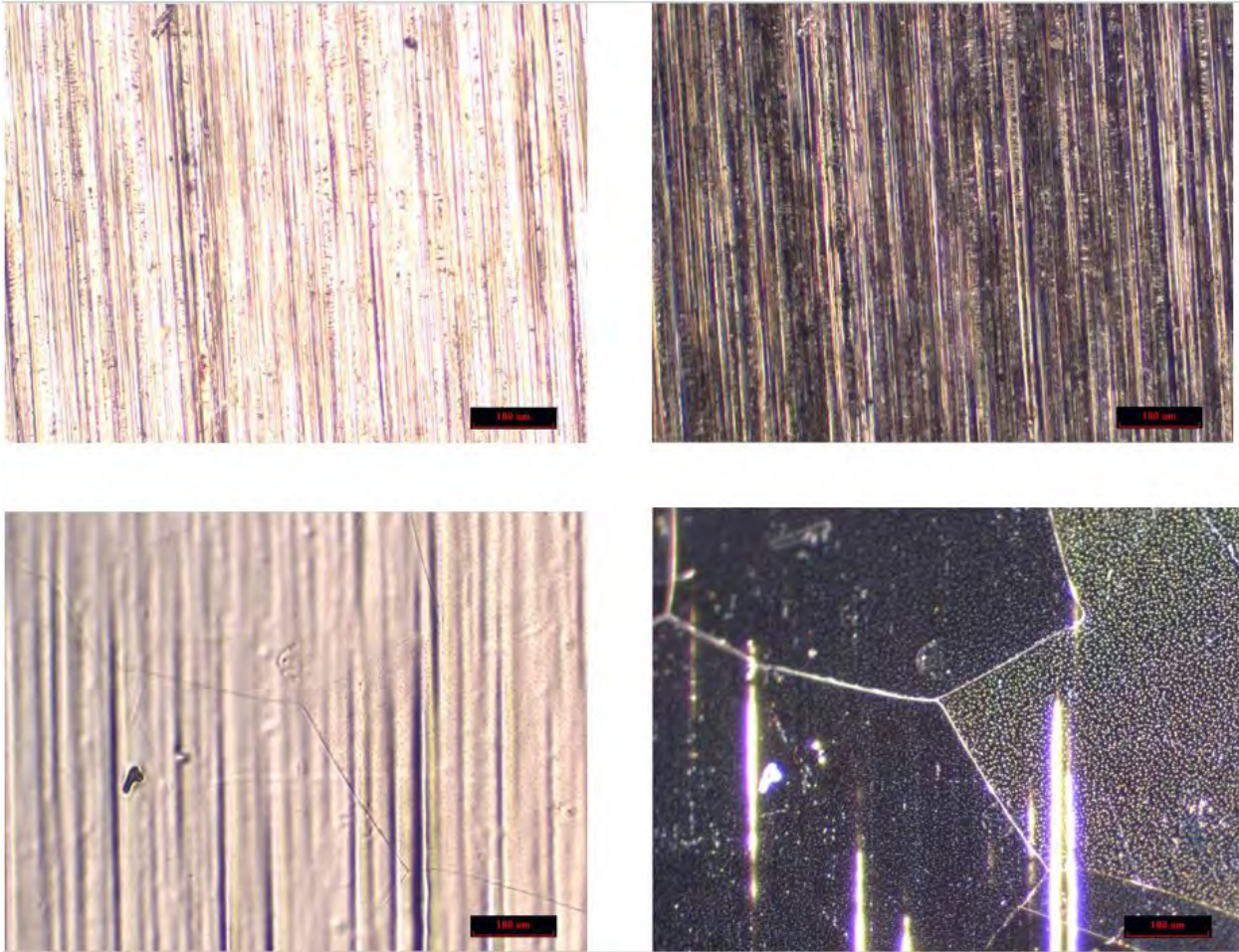


Fig. 6

Optical microscope images of the surface of Unpolished Cu. The top two images are bright field (left) and dark field (right) displays of unannealed copper. The bottom two are bright and dark field images of annealed Cu.

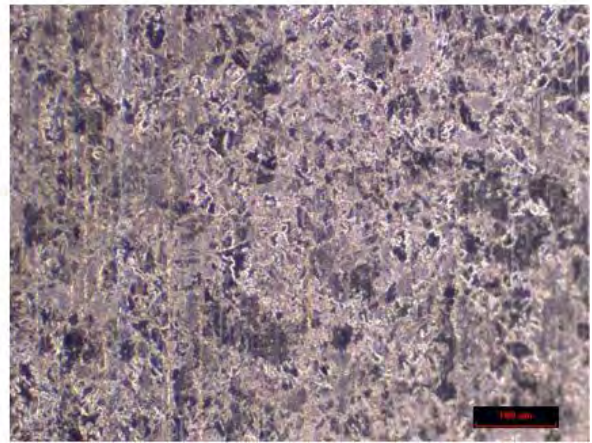
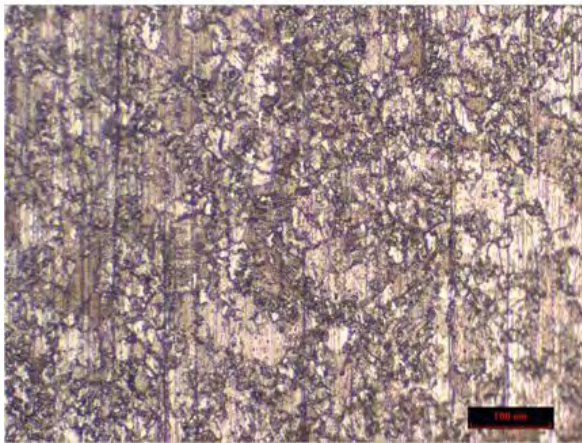
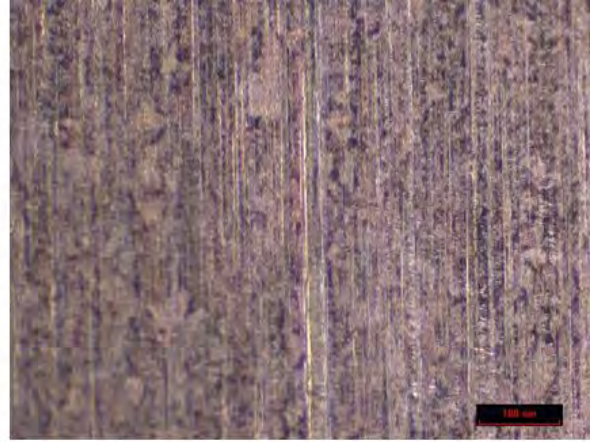
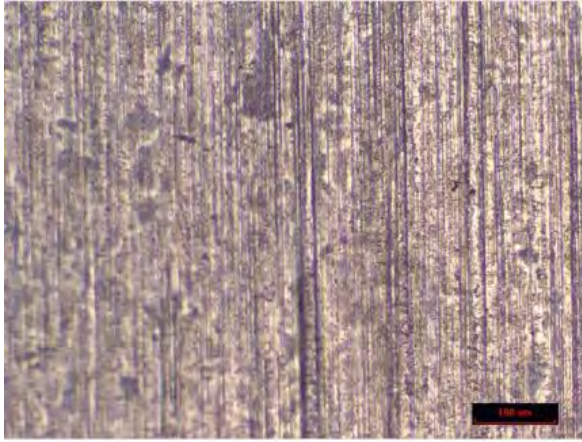


Fig. 7

Opt. microscope images of polished unannealed copper using the constant voltage source. Both polished for 5 minutes. The top two being bright and dark field images of Cu polished at a current of 30 mA and .5 V. The bottom two being bright and dark field images of Cu polished at a current of 760 mA and 1.5 V.

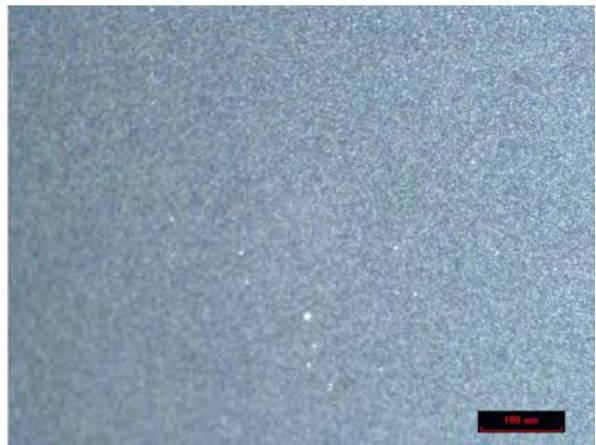
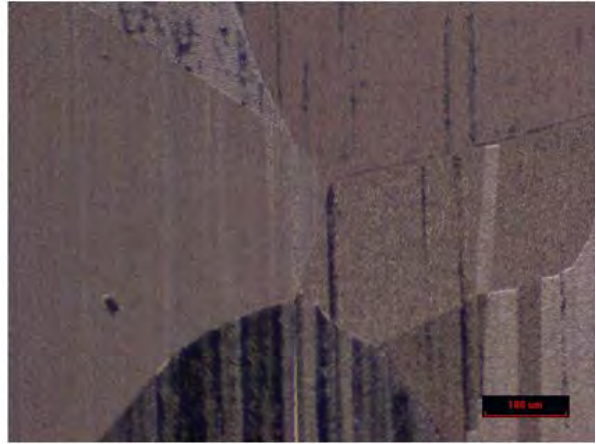
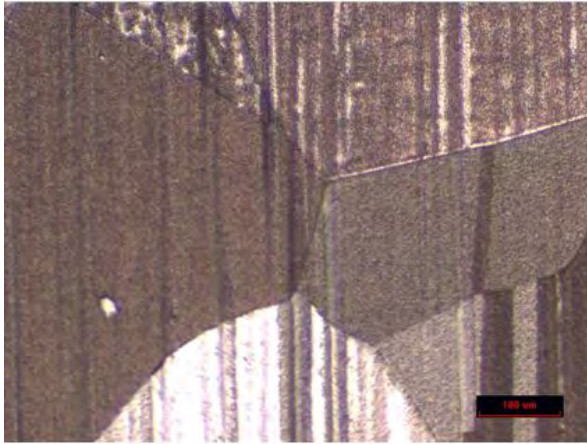


Fig. 8

Opt. microscope images of polishing done on annealed Cu samples. The top two are bright and dark field images of Cu polished at a current of 30 mA and voltage of .5 V for a time period of 90 minutes using the constant voltage source. The bottom two are bright and dark field images of Cu polished at a current of 760 mA and voltage of 8.8 V for a time period of 10 minutes using the constant current source and is our best results.

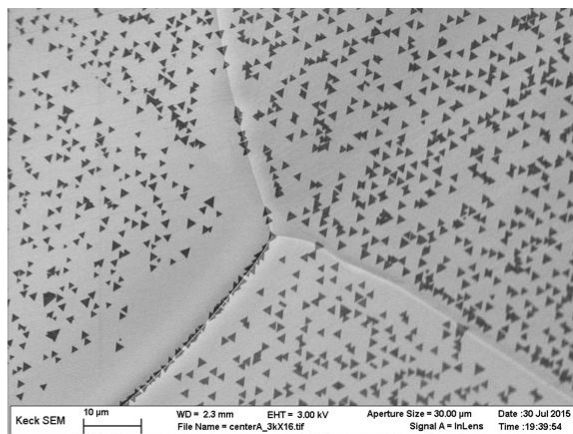
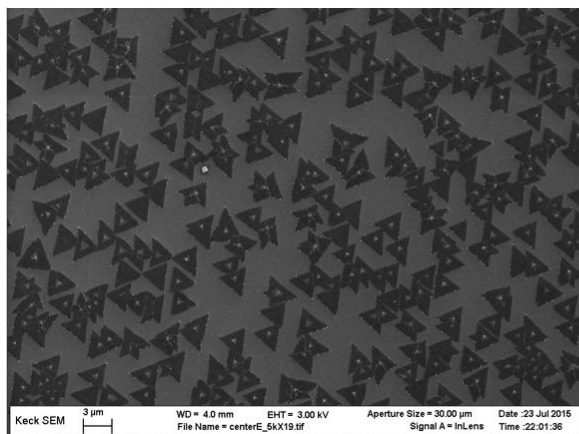


Fig. 9

SEM images of boron nitride growth on polished copper samples. Both images are on annealed copper that was polished using a constant current source. The one on the left was polished for 5 minutes, and the one on the right for 10 minutes.

Precise Control of Molecular Weight Distribution Shape

Lauren N. Dupuis¹, Dillon T. Gentekos², and Brett P. Fors^{*2}

¹Department of Chemical and Biological Engineering, Montana State University, Bozeman, MT

²Department of Chemistry and Biochemistry, Cornell University, Ithaca, NY

Abstract

There is a large interest in the field of polymer chemistry, due to the fact that polymers are part of so many aspects of our daily lives. It is becoming more apparent that having complete control of a polymer molecular weight distribution (MWD), and in turn the properties of the polymer, would have a major impact on the manufacturing of polymers. By using controlled radical polymerization (CRP), a systematic method of initiator addition has been used to precisely shape the MWD of styrene polymers. Also, previously only dispersity (\mathcal{D}) and the average molecular weight (M_n) have been used to describe polymers and we have shown that this is not sufficient information to describe the absolute distribution of chain lengths. The shape of the MWD has been predicted to affect polymer properties, but no one has been able to test this theory experimentally.

Introduction

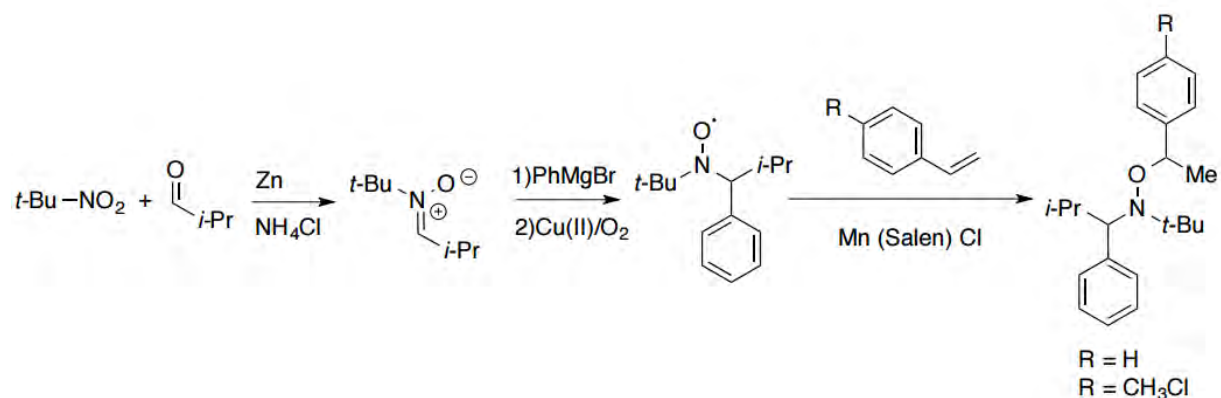
Polymers are used in almost everything, both natural and synthetic objects. That is why research about them, to get a better understanding, is crucial. The self-assembly of block copolymers, when two polymers are attached and repel each other so that they assemble in certain patterns or morphologies, is used for many things in industry such as nanolithography and filtration membranes¹. These morphologies are theorized to be affected by the MWD shape². If it's proven that a polymer's MWD plays a role determining which morphology a polymer block will form, along with other properties, it will also have a major impact on the design and manufacturing of many products. Having a method of making precisely controlled polymer MWD in an easy, cheap, and fast enough way to be used in industry would be very beneficial.

In the past, many thought that having a monodisperse MWD gives the most effective control on polymer properties, but a more disperse MWD could have a desired effect on certain properties. \mathcal{D} represents the ratio of weight average (M_w) to the number average molecular weights (M_n). \mathcal{D} and M_n are the two parameters used to characterize a polymer, but there are theories that say these are not enough to describe a MWD and that the specific shape could also impact polymer properties⁶. This theory has not been fully tested because there hasn't been a way to have good control over a MWD's shape.

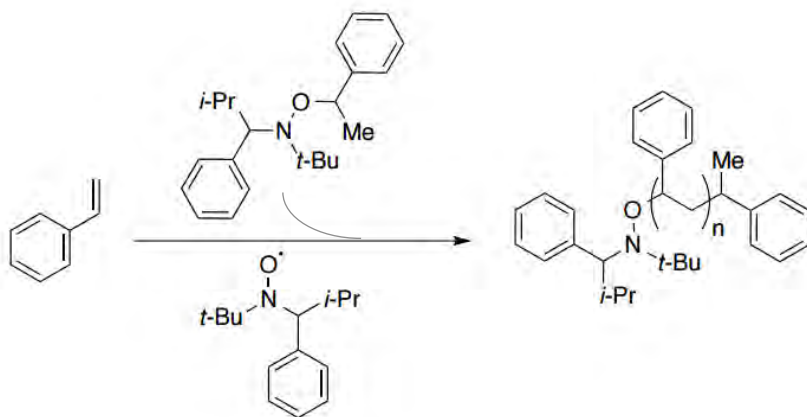
There are several methods previously used to control the \mathcal{D} of polymers but most have certain limitations. Uncontrolled polymerizations have been used for creating a large \mathcal{D} ⁵. However, there is no control of the M_n or MWD shape when this method is used. When using a blending

polymers method, several polymers with M_n 's and \bar{D} 's that differ are mixed together². This method does not have a continuous distribution and it also takes a lot of work to precisely control the synthesis of several polymers. Depolymerization, or equilibrium polymerization, is a method that works well for controlling \bar{D} , but it only works for lactide polymers and doesn't have control over the shape of the MWD³.

The ideal candidate for controlling MWD shape is nitroxide mediated polymerization (NMP), which is a type of controlled radical polymerization (CRP). CRP methods have been shown to have great control of \bar{D} previously⁹ and NMP has first order kinetics, making it easy to manipulate MWD shape.



Scheme 1. Synthesis of Initiators



Scheme 2. Nitroxide mediated styrene polymerizations with initiator additions to control MWD.

Results

NMP reactions were used as an initial example of how CRP methods can be used to have complete control over polymer MWD. NMP was perfect for these initial experiments because it only has two components to the reaction and has first order kinetics, making the method very simple. By systematically altering the initiating process, rate and amount, MWD shape can be manipulated

while also keeping control of \bar{D} and M_n . The chains grow at the same rate and one chain grows on each initiator molecule. The theoretical chain length can be calculated from the relative amounts of monomer and initiator added. The amounts of the initiator was kept the same for all polymerizations so that each experiment could be more easily compared.

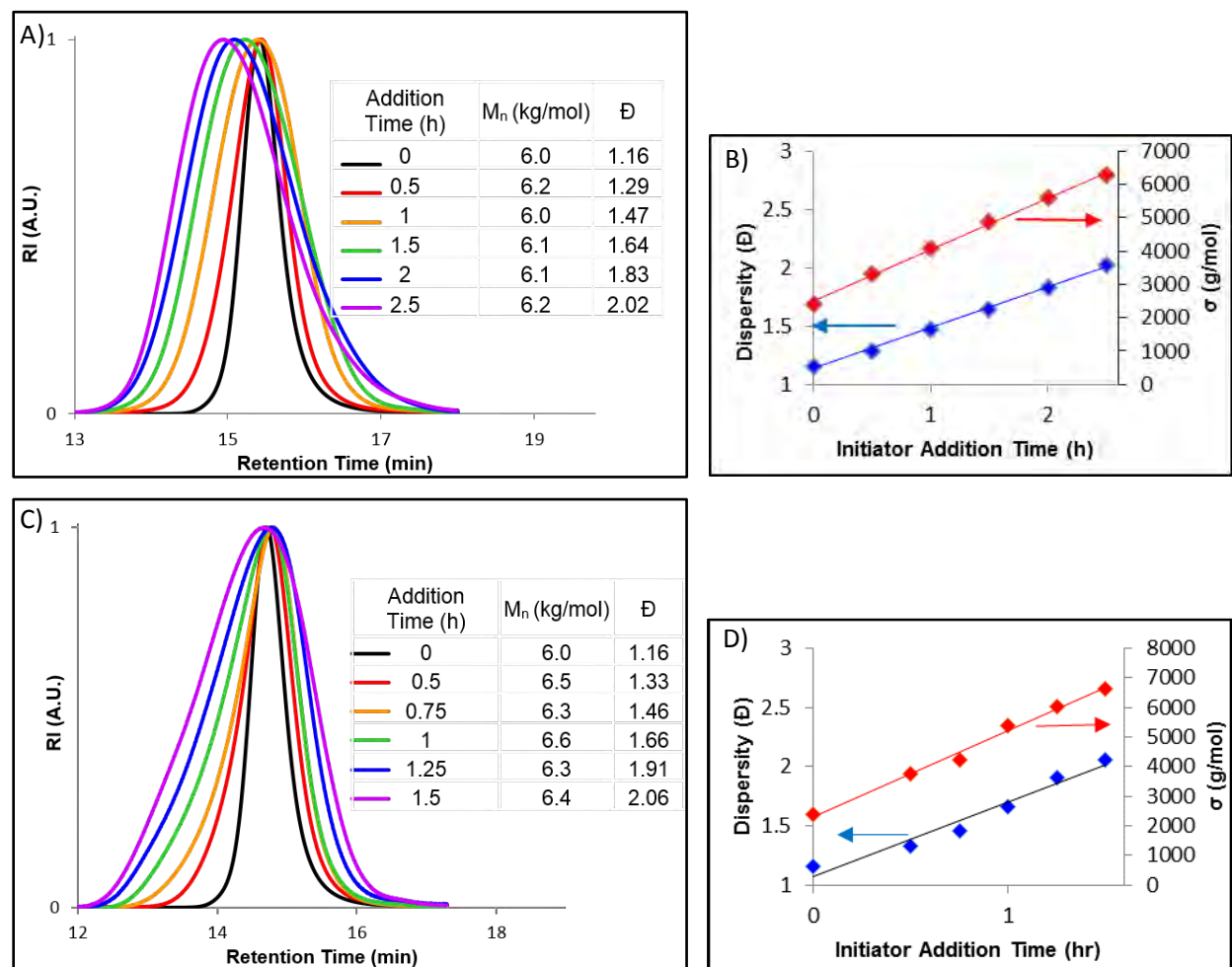


Figure 1. Altering the initiation rate altered the shape of the graph. A) is a constant addition rate and B) shows a linear relationship of \bar{D}/σ and addition time. C) is a ramped rate with D) showing there is still a linear relationship.

The initiator was synthesized using the procedure in the literature¹⁰, shown in Scheme 1. Using commercially available 2methyl-2nitropropane, zinc metal was used to do a reductive condensation onto isobutyraldehyde to make the nitron, **1**. Addition of a phenyl Grignard to the nitron and then oxidizing with Cu(II) formed the TIPNO nitroxide radical, **2**. The nitroxide radical was added on to the p-vinyl benzyl chloride using a manganese (salen) catalyst to make the final

alkoxyamine initiator, **5**. Another initiator, **6**, was also made by substituting styrene for p-vinyl benzyl chloride.

The procedure for the styrene polymerizations¹⁰ is shown in Scheme 2. Initiator, **6**, was used to control the growing polymer chains by regulated additions throughout the reaction. The amount of initiator was kept constant for the first experiments to simplify the comparisons and show a trend more readily. Changing the amount of time initiator was added over systematically broadened \mathcal{D} , which can be seen in Figure 1a. M_n stays the same as \mathcal{D} gets larger, showing control of the polymerization. Figure 1b displays the linear relationship between the addition times and \mathcal{D} , showing that by controlling the initiating process \mathcal{D} is also able to be controlled.

\mathcal{D} is related to the standard deviation of polymer chain lengths but is normalized to M_n . Therefore, because \mathcal{D} and σ can be controlled, it can be assumed that regulated initiator addition can control the breadth and the average of the distribution. This is proven in Figure 1b, which shows that the relationship between addition time and σ is linear.

By changing the addition rate to a linearly ramped rate, the shape of the MWD can be further manipulated. Instead of just broadening \mathcal{D} Figure 1c shows how the distribution is also shifted towards higher molecular weights, though the M_n is the same. The ramped rate also showed a linear relationship between the addition times and \mathcal{D} , as well as addition time and σ which can be seen in Figure 1d. This shows that there is still control and also the MWD can be manipulated to almost any shape by altering the addition rate. For further proof that this is true, a nonlinear increasing rate was tested and showed the same control with a more symmetrical MWD. The rates are all compared in Figure 2, showing how the different rates alter shape.

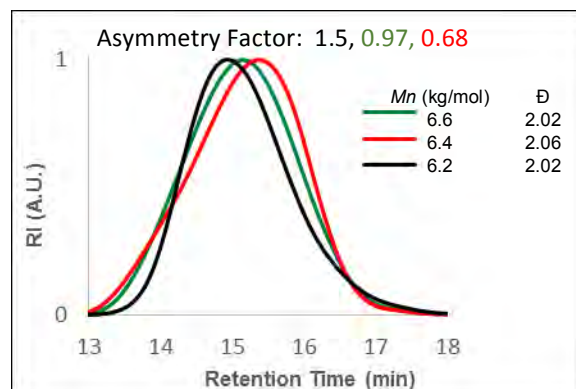


Figure 2. Comparing addition rates to show that polymers with the same M_n and \mathcal{D} can have different MWD shapes. Black line is constant addition, red line is linear addition, and green line is nonlinear addition. Asymmetry gives more description of the curves.

Polymers have been described by only their M_n and \bar{M}_w , however, Figure 2 demonstrates how this is not sufficient information. Two polymers can have the same exact M_n and \bar{M}_w but have completely different MWD. In Figure 2, a third parameter was introduced, the asymmetry factor. The asymmetry factor is the distance from the max peak of the curve to the right side divided by the distance from the max peak to the left side at 10 % of the peak height. The asymmetry factor for the constant rate is 1.5, indicating that the MWD includes more low molecular weight polymers, while the linear rate asymmetry factor is 0.68 because its MWD includes more high molecular weight polymers. The nonlinear asymmetry factor is 0.97, showing that it has a nearly symmetrical MWD.

Conclusion

This new method of using CRP is a simple, yet effective, way to precisely control polymer MWD. Through altering initiation rates during polymerization, \bar{M}_w and MWD shape can be manipulated to be virtually anything, while still remaining in control of M_n . The next step in this project is to use kinetic modeling of the initiator addition and how it influences the MWD so that it would be very simple to find the addition profile for any polymer MWD. Also this type of systematic procedure should be able to be extended to other types of monomers and CRPs, such as ATRP⁷.

By altering the MWD shape and keeping \bar{M}_w and M_n the same, it is now clear that two parameters is not enough to sufficiently describe a polymer. Using the asymmetry factor will allow a more precise description of a polymer and the properties that it will have.

Another continuation of this project is testing the effect on properties that the shape of the MWD will have on polymers. To study these effects the polymers previously made by the initiator additions will be used, with only MWD shape differences, to make block copolymers. Block copolymers are used for many things in industry and have interesting properties, including order-disorder transition (ODT)⁸. Using rheology to look at these ODT properties and see how they change for different MWD could prove the theory that polymer properties are, in fact, affected by MWD shape.

Experimental

Synthesis of N-tert-butyl-alpha-iso-propylnitrone, 1

2methyl-2nitropropane (5 g, 48.5 mmol), isobutyraldehyde (4.4 mL, 48.5 mmol), and ammonium chloride (2.9 g, 53.4 mmol) were measured into a three-neck round bottom flask. The round bottom was degassed by nitrogen bubbling, or sparged, for twenty minutes. Then it was put in an ice bath and stirred. Diethyl ether (48.5 mL) was added and the solution was sparged again for ten minutes. Zinc dust (12.6 g, 194.2 mmol) was added slowly over one hour. The round bottom was kept in the ice bath for an hour until everything looked well mixed and the solution looked gray/blue. The solution was warmed to room temperature and stirred for eight hours.

The reaction was filtered with a sintered glass funnel to remove the zinc. Then the white zinc residue left over was washed with methanol (30 mL) three times. The liquid, with product in it, was

poured into a separatory funnel and the product was extracted with dichloromethane (50 mL) four times. The organic layers were combined and dried with brine (80 mL) and magnesium sulfate and filtered with a cotton funnel. The product was concentrated under reduced pressure to evaporate solvent off. We had 5.66 g of crude nitron, **1**, a yield of 82%.

Synthesis of 2,2,5-trimethyl-4-phenyl-3-azahexane-3-nitroxide, 2

A solution of the nitron, **1**, (3 g, 21 mmol) and tetrahydrofuran (22.7 mL) was cooled to 0°C with an ice bath and stirred. A 3M solution of phenyl magnesium bromide (14.1 mL, 42 mmol) and diethyl ether was made (Grignard reagent) and added dropwise by syringe while the nitron solution was continuously stirred. A green precipitate formed and solution was warmed to room temperature and stirred for seventeen hours.

Concentrated ammonium chloride (4.5 mL) was added dropwise to the Grignard solution at 0°C along with DI water (13.6 mL) until everything was dissolved. The organic layer was separated and the aqueous layer was extracted with diethyl ether (22.7 mL). The organic layers were combined and dried with magnesium sulfate and filtered. The solution was concentrated under reduced pressure. Methanol (90.9 mL), ammonium hydroxide (6.8 mL), and copper acetate (210 mg, 1.05 mmol) was added to the concentrated solution. The solution was open to air and had air bubbling through. The solution stayed orange so another large amount of copper acetate was added. After ten minutes of stirring, the blue solution was concentrated under reduced pressure.

The solution was added to a mixture of chloroform (90.9 mL), sodium bisulfate (22.7 mL), and DI water (90.9 mL). The organic layer was separated and the aqueous layer was extracted with chloroform (22.7 mL). The organic layers were combined and washed with sodium bicarbonate (27.3 mL), dried with brine and magnesium sulfate, then concentrated under reduced pressure. The crude product was purified by flash column chromatography with 30:1 hexanes/ethyl acetate as the solvent. There was 2.461 g of TIPNO, **2**, 53.2% yield.

Synthesis of [N,N'-bis(3,5-di-tert-butylsalicylidene)-1,2-cyclohexanediaminato] manganese(III) chloride, 4

To make the salen, **3**, salicylaldehyde (2.44 mL, 20 mmol) was weighed out into a 50 mL round bottom with absolute ethanol (25 mL). This reaction was done under nitrogen. Ethylenediamine (600 mg, 10 mmol) was added to solution drop-wise. Precipitate crashed out while the ethylenediamine was being added. The reaction was stirred at room temperature for an hour and then filtered. The yellow crystals were filtered and then dissolved in ethanol. The solution was heated with a heat gun and then allowed to cool and recrystallize overnight. 2875.5 mg of **3** was made.

For the magnesium (salen) chloride catalyst, **4**, the salen, **3**, (2.682 g, 10 mmol) was dissolved in hot ethanol (80 mL), all in a three-neck round bottom with a reflux condenser on top and put in an oil bath at 80°C. After the crystals were dissolved, solid magnesium diacetate (2.442 mg,

10 mmol) and lithium chloride (420 mg, 9.9 mmol) were added and the solution continued to reflux for four hours. The reaction mixture was condensed and the brown powder was washed with DI water and condensed again. 2.06 g of catalyst, **4**, was obtained with a 57.7% yield.

*General Procedure for Manganese Coupling, Synthesis 2,2,5-Trimethyl-3-(1-(4'-chloromethyl)phenylethoxy)-4-phenyl-3-azahexane **5***

To a three-neck round bottom, **2** (220 mg, 1 mmol) and p-vinyl benzyl chloride (282 μ L, 2 mmol) were added and sparged for 10 minutes. The manganese catalyst, **4**, (140 mg, 0.4 mmol) was weighed into a round bottom and a 1:1 solution of toluene/ethanol (7.5 mL) was added. The round bottom was then sparged. The catalyst solution was added by syringe to the TIPNO solution. Under a stream of nitrogen, di-tert-butyl peroxide (270 μ L, 1.5 mmol) and sodium borohydride (114 mg, 3 mmol) was added to solution. The reaction stirred at room temperature, and after a couple hours some sodium borohydride and di-tert-butyl peroxide was added until the solution turned orange. The reaction went for around a total of twenty-four hours.

Reaction solution was concentrated under reduced pressure and extracted with dichloromethane (7.5 mL) and DI water (10 mL). The aqueous layer was extracted again with dichloromethane (5 mL) three times. The organic layers were combined and dried with magnesium sulfate, then concentrated under reduced pressure. Crude product was purified by flash chromatography in 10:1 hexanes/dichloromethane. There was 162 mg of initiator, **5**, 43.3% yield.

The same procedure was used to make N-tert-butyl-N-(2-methyl-1-phenylpropyl)-O-(1-phenylethyl)hydroxylamine, **6**, by using styrene instead of p-vinyl benzyl chloride.

Styrene Polymerization Method

Styrene was first filtered with small pipette column of basic alumina to remove inhibitor. A dilution of TIPNO, **2** (6.5 mg, 0.0295 mmol), was made in filtered styrene (1.2 mL, 10.47 mmol). In four small vials, filtered styrene (420 μ L, 3.67 mmol) and 2 μ L of the TIPNO dilution were added, along with small stir bars. The initiator, **6** (36 mg, 0.111 mmol), and styrene (633 μ L, 5.52 mmol) were added to two other vials. All six vials were degassed by doing three cycles of freeze-pump-thaw. 220 μ L of both initiator solutions were pulled into a 1 mL syringe that was first degassed three times with nitrogen. The syringes were loaded onto a syringe pump that was set at a certain addition rate. The needle was quickly taken out of the initiator solution vial and put in the TIPNO/styrene solution vial and lowered into the solution. The vials were submerged into a 120°C oil bath and the syringe pump was started. Reaction times varied for each experiment, and then the vials were cooled by liquid nitrogen to stop polymerization.

Acknowledgements

This work was supported by the Cornell Center for Materials Research with funding from the Research Experience for Undergraduates program NSF grant (DMR-1063059 and DMR-1120296).

References

- (1) Matyjaszewski, K.; Gnanou, Y.; Leibler, L. *Macromolecular Engineering: From Precise Macromolecular Synthesis to Macroscopic Materials Properties and Applications*; Wiley-VCH: Weinheim, Germany, 2007.
- (2) Lynd, N. A.; Meuler, A. J.; Hillmyer, M. A. Polydispersity and Block Copolymer Self-Assembly. *Progress in Polymer Science* 2008, 33, 875-893.
- (3) Lynd, N. A.; Hillmyer, M. A. Influence of Polydispersity on the Self-Assembly of Diblock Copolymers. *Macromolecules* 2005, 38, 8803-8810.
- (4) Lynd, N. A.; Hillmyer, M. A. Effects of Polydispersity on the Order-Disorder Transition in Block Copolymer Melts. *Macromolecules* 2007, 40, 8050-8055.
- (5) Widin, J. M.; Schmitt, A. L.; Im, K.; Mahanthappa, M. K. Unexpected Consequences of Block Polydispersity on the Self-Assembly of ABA Triblock Copolymers. *J. Am. Chem. Soc.* 2012, 134, 3834-3844.
- (6) Lynd, N. A.; Hillmyer, M. A.; Matsen, M. W. Theory of Polydispersity Block Copolymer Melts: Beyond the Schultz-Zimm Distribution. *Macromolecules* 2008, 41, 4531-4533.
- (7) Listak, J.; Jakubowski, W.; Mueller, L.; Plichta, A.; Matyjaszewski, K.; Bockstaller, M. R. Effect of Symmetry of Molecular Weight Distribution in Block Copolymers on Formation of "Metastable" Morphologies. *Macromolecules* 2008, 41, 5919-5927.
- (8) Hadziioannou G, Skoulios A. Structural study of mixtures of styrene isoprene two- and three-block copolymers. *Macromolecules* 1982, 15, 267-271
- (9) Hawker, C. J.; Bosman, A. W.; Harth, E. New Polymer Synthesis by Nitroxide Mediated Living Radical Polymerizations. *Chem. Rev.* 2001, 101, 3661-3688.
- (10) Benoit, D.; Chaplinski, V.; Braslau, R.; Hawker, C. J. Development of a Universal Alkoxyamine for "Living" Free Radical Polymerizations. *J. Am. Chem. Soc.* 1999, 121, 3904-3920.

Using Thermal Gradients to Understand Local Magnetization Dynamics in Nanoscale Bilayer Systems

Liliana Frye¹, Jason Bartell², Isaiah Gray², Gregory Fuchs²

¹Department of Physics, Vassar College, Poughkeepsie, NY 12604

²Department of Applied and Engineering Physics, Cornell University, Ithaca, NY 14853

Abstract

Using time resolved anomalous Nernst effect microscopy and applications of the spin Hall effect, magnetization dynamics in two stacked nanoscale wires can be studied, but only if their interactions with an evolving thermal gradient can be well defined. A laser pulse (width 1.2739 ps) was applied to a bilayer of Platinum and Yttrium Iron Garnet, and secondly, a bilayer of Permalloy and Bismuth Selenide. This was done both computationally and in a mixing experiment to find a temperature gradient lasting ~ 18 and ~ 35 ps respectively, and a thermal relaxation time of ~ 0.2 and ~ 2 ns respectively. Notably, the YIG temporal profile is strongly influenced by the other substances in the stack, and the temperature of the material rises and falls twice over the whole experiment instead of the predicted smooth peak and gradual relaxation.

I. Introduction

The areas of magnetism and spintronics are increasingly popular topics of study in physics and engineering because current technology is primarily based on charge, but calculations and prototypes indicate that magnetic technology has potential for increased capacity and speed. This promising conclusion is drawn from studies of the spin Hall effect, which is responsible for the sorting of subatomic particles in magnetized materials based on spin and charge instead of popular technology's utilization of the Hall effect, which sorts the particles based only on charge. In the past, light has been used to study these magnetic materials, but this approach cannot yield sufficient information due to the spatial resolution limitations of the optical diffraction technique. However, studies of the interaction of heat and magnetization present no such resolution limitations.

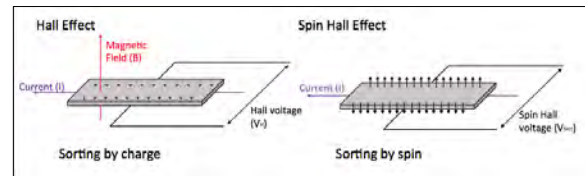


Figure 1: Comparison of the Hall and Spin Hall effect. Note that the spin Hall effect works in reverse, as well: SHE creates a spin current, and ISHE detects a spin current.

Magneto-thermoelectric interactions are relatively well understood mathematically, the most useful of which for the purpose of understanding nanoscale materials, is the time-resolved anomalous Nernst effect (TRANE), which uses heat and light to convert the local magnetic moment in the material to a voltage.^[1] The electric signal can be used to quantitatively study the evolution of the thermal gradient within the material, and to image magnetization dynamics of the materials at extremely high spatial and temporal resolution.

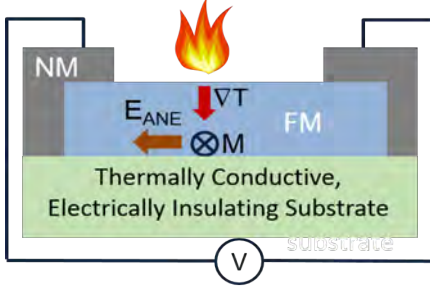


Figure 2: Illustration of the time-resolved anomalous Nernst Effect, where FM denotes a ferromagnetic material, NM denotes a nonmagnetic material, and E_{ANE} is the electrical signal produced due to the thermal gradient and magnetic moment of the material. [2]

Fundamentally, the behavior of the thermal gradient within the material must be understood before the TRANE method can extract any significant information. So far, the simplest system has been studied: one ferromagnetic nanowire on an insulating substrate. The next steps to this study are to take these same techniques and apply them to a bilayer system. This paper studies the behavior of a thermal gradient as it passes through these different layered materials, and qualitatively and quantitatively scrutinizes the evolution of the temperature gradient as a function of interfacial thermal resistance in systems of Platinum and Yttrium Iron Garnet (YIG) on a substrate of Gadolinium Gallium Garnet (GGG), and secondarily of a system of Permalloy and Bismuth Selenide on a Sapphire substrate.

II. Methods and Materials

The bilayer systems were studied both computationally and experimentally: the computational approach presents a far finer temporal resolution than the experimental version, but both techniques provided insight into the physical problem.

Materials

	Pt*	YIG ^{[3][4]}
Thermal conductivity ($\text{W m}^{-1} \text{K}^{-1}$)	71.6	0.0270
Density (kg m^{-3})	21450	5170
C_p ($\text{J K}^{-1} \text{mol}^{-1}$)	133	600

	Permalloy ^[1]	Bi_2Se_3 ^[5]
Thermal conductivity ($\text{W m}^{-1} \text{K}^{-1}$)	46.4	2.50
Density (kg m^{-3})	8700	6820
C_p ($\text{J K}^{-1} \text{mol}^{-1}$)	430	189.8

	GGG ^[6]	Sapphire*
Thermal conductivity ($\text{W m}^{-1} \text{K}^{-1}$)	12.0	2.50
Density (kg m^{-3})	7080	6820
C_p ($\text{J K}^{-1} \text{mol}^{-1}$)	415	189.8

Table 1: Material properties. Asterisks denote the materials with numerical values built into COMSOL.

YIG is an especially relevant material because it is a ferromagnetic insulator whose properties are difficult to measure using more popular techniques, but this method circumvents those problems because it does not rely on electrical transport. The spin Hall effect is the relevant physical study pertaining to YIG.

Bismuth Selenide is not a magnetic material (it is a topological insulator) but is important in the magnetics world because it induces spin torque, and therefore is influential to magnetic materials. The TRANE method is the most useful physical study for Bismuth Selenide.

Parameters of the Problem

Each nanowire was 30 nm thick, 2 μm wide, 10 μm long, stacked onto a substrate that was roughly two orders of magnitude thicker, twice as wide, and twice as long. The size of the substrate varied in each computational measurement and it was

concluded that the specific size was of very minimal importance to the thermal gradient within the nanowires. The heat was applied using a pulsed laser with a pulse width of 1.2739 ps, and a laser path radius of 44 nm.

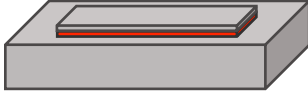


Figure 3: Simple illustration of the sample. Top to bottom: Pt, YIG, GGG or Permalloy, Bi₂Se₃, Sapphire. (Red indicates material of interest).

Computational Method

COMSOL multiphysics modeling software is a matrix-based program that solves the thermal diffusion equation to find the dissipation of heat through this system. The user can “build” a system where every parameter is chosen and specified, and the program uses finite-element analysis by breaking the volume into “mesh elements” and integrating over each individual element. The size of the mesh can be chosen manually to ensure maximum efficiency and precision, especially within the nanowires and along the boundaries. A Gaussian waveform was inputted as the laser heat pulse, and the mesh was set to the appropriate fineness. Typically, the simulation was run to 0.2 ns, but to study the complete temperature profile, it was run out to as far as 10 ns. Both the spatial temperature and temporal temperature behavior were further studied using Mathematica, in addition to the spatial and temporal gradients.

Laser heat pulse input (Gaussian):

$$Q_{in} = Q_0 R_c e^{-\frac{|z|}{skin}} \left(\frac{1}{2\pi(sigx)sigy} \right) * e^{-\frac{(x-x_0)^2}{2(sigx)^2} - \frac{(y-y_0)^2}{2(sigy)^2}} * e^{-\frac{(t-mid)^2}{2(pulsewidth)^2}} \quad (1)$$

Where Q_0 is the total laser power, R_c is the reflection coefficient, $skin$ is the skin depth, $sigx$ and $sigy$ are the pulse’s standard deviations in the x and y direction (the pulse is incident on the xy plane at $z=0$), x_0 and y_0 are the path center’s coordinates, mid is the mean of the temporal distribution, and $pulsewidth$ is self explanatory.^[1]

Experimental Method

To confirm the findings from the computational approach, a “fast-mixing experiment” was attempted. A magnetic microscope was used, directing a laser pulse onto the sample. Using the anomalous Nernst effect, the resulting Electric current was measured and therefore the changing temperature gradient. Because the equipment is not sensitive enough to measure this temporal temperature data directly, a known waveform was generated, mixed with that pulse, and the resulting data was deconvolved to find the temperature gradient. A fast mixing experiment mixes a 100 ps pulse with the unknown curve, where a slow-mixing experiment mixes a 1.5 ns pulse.

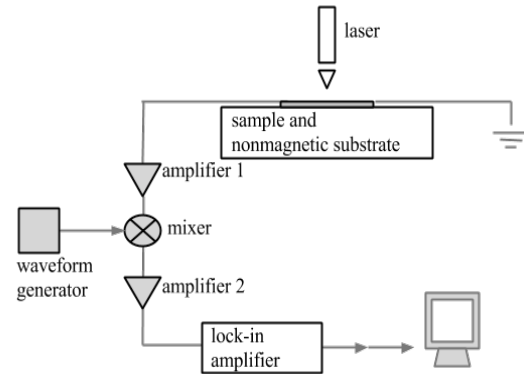


Figure 4: Experimental apparatus for the mixing experiment. This is a simplified diagrammatical representation of the hyper-sensitive magnetic microscope used in the Fuchs Group for magnetic imaging, here configured for the mixing of a temperature heat pulse with a generated known pulse.^[2]

The fast mixing experiment is the most direct way to measure the time frame of the pulses of heat. Slow mixing still gives valuable time-frame information, but it is more quantitative than qualitative.

III. Results

COMSOL Results

1. Platinum, YIG on GGG substrate:

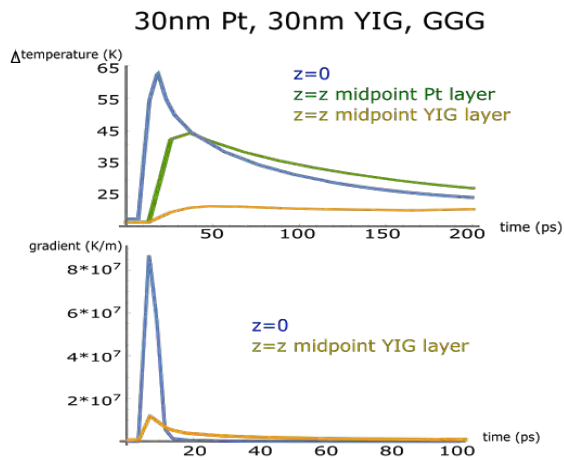


Figure 5: COMSOL simulation results for a bilayer of Platinum and Yttrium Iron Garnet. In the top graph, the temperature is taken as a function of time at three points in the bilayer: the hottest point in the system (blue), where the pulse is incident upon the Platinum, halfway into the Platinum (green), and halfway into the YIG (yellow).

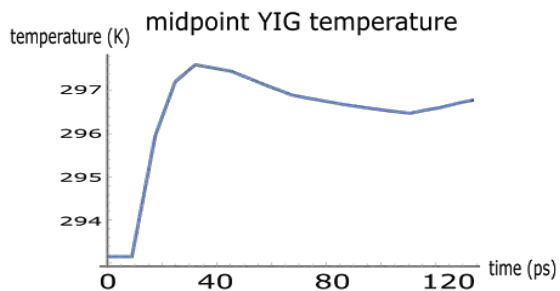


Figure 6: Enlarged image of the temporal curve of YIG from Figure 5.

It is important to note here that the temperature of the YIG rises predictably, but the actual temperature gain is very tiny, approximately 5 K, then it loses some heat,

then rises again, attempting to equilibrate with the rest of the system. The simulation must be run for a longer time, out to 1 nanosecond, to ensure a complete visual of the heat evolution.

2. Permalloy and Bismuth Selenide on a Sapphire substrate (respectively):

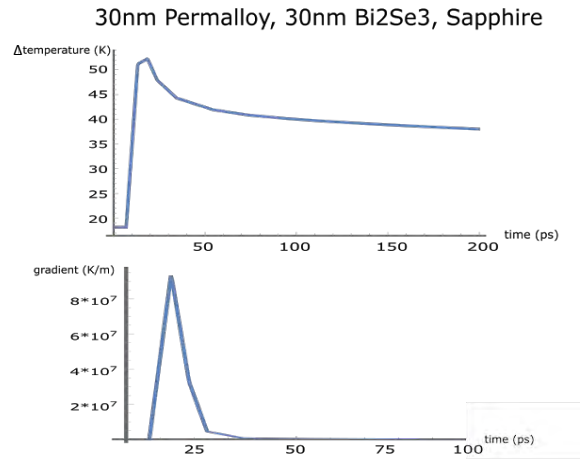


Figure 7: COMSOL results for a bilayer of Permalloy and Bismuth Selenide. Data taken at the hottest point in the system (theoretically, the center of the heating spot on the surface of the Permalloy).

The Bismuth Selenide results pose questions about the material and the setup as to why the peak is unpredictably jagged despite many data points between the apparent corners in the above figure, and why it takes almost ten times as long for the temperature of the system to return to room. More experimentation is necessary with this material.

Mixing Results

Unfortunately the mixer necessary for fast mixing (for the 100 ps generated pulse) was broken. Slow mixing data was recorded, using a 1.5 ns mixing pulse.

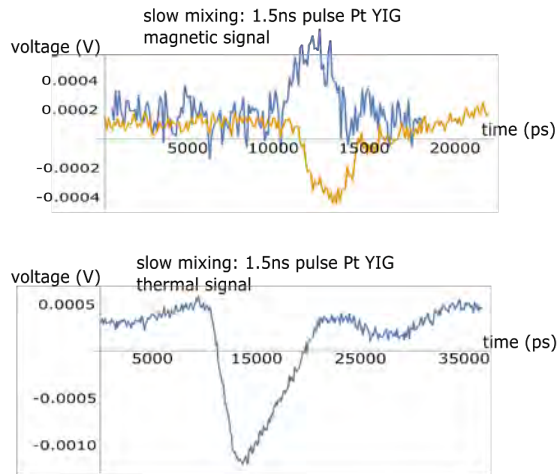


Figure 8: Slow Mixing data (see Figure 4: taken between *mixer* and *amplifier 2*). Amplifier 1: 0.1-6 GHz, 15.4 DB. Mixing pulse: 1.5 ns, 800 mV. Plot (1) is the magnetic signal, in the center of the wire, and plot (2) is the thermal signal, taken very close to the contact pad.

This data both proves that magnetic switching is occurring in the YIG sample (the blue line is in a $+m_y$ saturated field, and the yellow is in a $-m_y$ saturated field), and it supports the simulation data. However, more experimentation is necessary (specifically with the 100 ps mixer) before any definite quantitative conclusions can be made.

IV. Conclusion

The Platinum, YIG, and GGG system takes about 200 ps to return to room temperature, where the second system (Bismuth Selenide) takes about ten times as long to complete the cycle.

These two systems were successfully modeled using COMSOL multiphysics modeling software, and preliminary slow-mixing data indicates that the models are correct.

More experimental data needs to be taken before any definitive affirmations about the model. Next, the thermal profiles of the systems can be used to study the local magnetization dynamics according to the

spin Hall effect and the time-resolved anomalous Nernst effect.

V. Acknowledgements

Special thanks to Primary Investigator Professor Gregory Fuchs, Ph.D. students Jason Bartell and Isaiah Gray, and all of the members of the Fuchs Group of the Applied and Engineering Physics Department at Cornell University.

This work was supported by the Cornell Center for Materials Research with funding from the NSF MRSEC program (DMR-1120296) and the Research Experience for Undergraduates program (DMR-1063059 and DMR-1120296).

VI. References

1. J. Bartell, D. Ngai, G. Fuchs. *Table-top Measurement of Local Magnetization Dynamics Using Picosecond Thermal Gradients: Toward Nanoscale Magnetic Imaging*. 23 Feb 2015. TS “arXiv:1502.06505.”
2. The Fuchs Group, “Research.” 2015. Web. June 2015. www.fuchs.research.engineering.cornell.edu
3. Deltronic Crystal Industries, Inc, 2012. Web 24 June 2015. http://deltroniccrystalindustries.com/deltronic_crystal_products/yttrium_iron_garnet
4. S. Boona and J. Heremans, “Magnon thermal mean free path in yttrium iron garnet.” *Phys. Rev. B* 90, 064421 – Published 22 August 2014
5. O. Madelung, U. Rössler, M. Schulz; SpringerMaterials; sm_lbs_978-3-540-31360-1_945 (Springer-Verlag GmbH, Heidelberg, 1998), http://materials.springer.com/lb/docs/s_m_lbs_978-3-540-31360-1_945; accessed: 27-07-2015
6. J. Ahn, Thermal and optical properties of gadolinium gallium garnet, *Materials Research Bulletin*, Volume 17, Issue 11, November 1982, Pages 1393-1399, ISSN 0025-5408, [http://dx.doi.org/10.1016/0025-5408\(82\)90224-0](http://dx.doi.org/10.1016/0025-5408(82)90224-0).

Surface active block copolymer coatings incorporating stable free radicals to prevent marine biofouling

CCMR REU – Chris Ober Lab Group, Department of Materials Science and Engineering

Madeline Gelb, Case Western Reserve University

A set of polymers with systematically varied chemistry incorporating stable free radicals was designed and synthesized to be environmentally friendly antifouling and high fouling-release coatings. An anionically polymerized diblock of poly(styrene) and poly(dimethyl siloxane) was capped with an ATRP initiator to make a diblock macroinitiator. The macroinitiator was used to polymerize and randomly copolymerize six polymer variations of the monomers for pTEMPO, MAF6, and PEGMEMA. The chemical composition and molecular weights of each block were determined with ^1H NMR and GPC, respectively. Sample slide preparation allowed for initial surface chemical composition characterization that showed the fluoroalkyl MAF6 to be critical to surface chemical composition. Future biofouling assays will test the performance of the stable free radical for antifouling and high fouling-release properties. This research delves into the design and synthesis of these SABC materials incorporating stable free radicals.

Introduction

The accumulation of marine organisms on artificial surfaces exposed to seawater such as boats, piers, and even filters in desalination plants is known as marine biofouling. This buildup is detrimental to the performance of the structure causing decreased throughput in filters and pipes, corrosion of static objects, and increased drag on boats. In most applications the costs associated with biofouling are largely due to maintenance costs for removing and reinforcing and damage caused [1-2]. This problem is especially inimical for boats, however, as, in addition to the maintenance costs, the costs of operation due to increased drag are also significant. Just the US Navy Fleet is estimated at spending \$56 million every year, and this is less than 1% of the world's boats [3]. Costs incurred from biofouling are numerous, they range from straightforward spending like increased fuel usage due to drag, to money lost because of slower speeds for shipping, potential repair costs caused by decreased maneuverability, as well as the environmental restoration costs from hurting the environment.

Environmental concerns, in part stemming from fuel consumption but also in the types of antifouling and high fouling-release coatings available and their efficacy, have increased the demand for anti-biofouling coatings. Because the boating industry consumes huge amounts of fuel, approximately 300 million tons of the world's yearly fuel consumption, and therefore is a huge transport polluter releasing large amounts of pollution just in the form of emissions, the environmental benefit of decreasing drag and increasing fuel efficiency is immense [4]. To reduce drag and prevent biofouling traditionally, the marine industry has resorted to the use of biocidal toxic coatings that become injurious to the environment as they wear off [5]. This has led to increased regulation of biocide coatings. Furthermore, as boats with ineffective coatings travel around, they pick up marine organisms from ecosystems that can be transported on the side of the boat to new environments where they can become invasive. Due to both the monetary and environmental concerns, it has become critical to develop improved antifouling and high fouling-release coatings that inhibit marine organisms

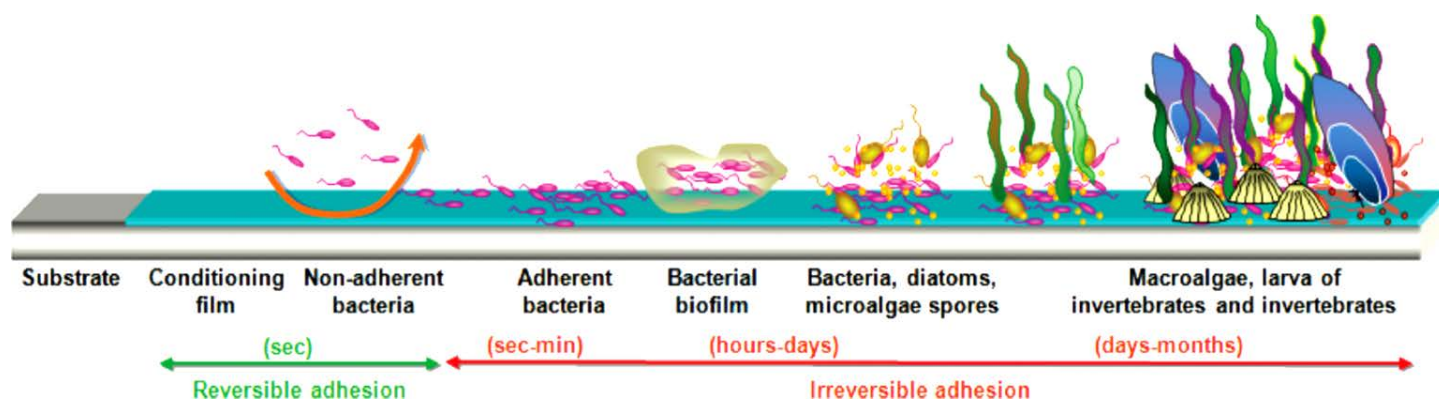


Figure 1 | Progression of marine biofouling [6].

from settling and stimulate release of any settled organisms.

Marine organisms accumulate on surfaces through a series of growth stages that each condition the surface for adhesion of larger and more detrimental marine organisms, as seen in figure 1 [6]. The initial phase consists of physical adsorption of protein and other organic molecules to condition surfaces with a biofilm suitable for marine organisms to adhere to. Initial bacteria can settle and create a biofilm matrix that makes the surface attractive for the settlement of further marine organisms. Some of these later marine organisms such as barnacles secrete protein adhesives that are cross-linked with oxidation and oxidation enzymes to form an irreversible foundation on the surface. This lays the groundwork for successive stages of bacteria, diatoms, micro and macro algae, and eventually invertebrates.

Previous research has identified many chemical strategies that prevent the permanent settlement and buildup of marine organisms through the use of bioactive surface chemistry. Many of the most effective chemical strategies focus on designing ambiguous surfaces that incorporate hydrophilic, hydrophobic, amphiphilic, and zwitterionic components [7-11]. The end goal of these strategies is to produce coatings that have increased lifetimes and effectiveness compared to current biocide based coatings without residual negative environmental consequences. To optimize these variables and improve upon the efficacy of coatings in deterring settlement and decreasing the adhesion strength of settled organisms to coatings, it is valuable to increase the available toolbox of chemical functionalities. Free radicals are of particular interest because of their potential to interfere with the oxidative protein crosslinking process that allows some marine organisms to transition from reversibly adhering to irreversibly adhering to the surface. The research described in this paper seeks to add to these functionalities the use of stable free radicals both alone and in combination with some of the proven chemical strategies.

Poly(dimethyl siloxane) (PDMS) based surface active block copolymers (SABCs) were developed incorporating stable free radical, PEG, and fluorinated chemistry. PDMS was chosen as the base for these polymer coatings due to previous research showing its low surface energy and

modulus to give it good properties in releasing adhered organisms [10, 11]. The SABC varieties studied here all had a poly(styrene) (PS), PDMS diblock capped with the atom transfer radical polymerization (ATRP) initiator 2-bromo-2-methylpropionic acid dimethylchlorosilanylpropyl ester from which the bioactive components were polymerized. (2,2,6,6-Tetramethylpiperidin-1-yl)oxyl methacrylate (TEMPO), polymerized from 2,2,6,6-tetramethylpiperidyl methacrylate (pTEMPO) before being oxidized to the free radical state, was introduced as the free radical component. To force the free radical to the surface, prevent protein adsorption, deter organisms from adhering, and create a more ambiguous surface, the TEMPO component was systematically polymerized alone and copolymerized with the respective hydrophilic and hydrophobic monomers of poly(ethylene glycol methyl methacrylate) (PEGMEMA), and poly(3,3,4,4,5,5,6,6,7,7,8,8,8-tridecafluorooctyl methacrylate) (MAF6), a fluorinated methacrylate [10, 11]. This set of materials incorporates a wide range of active chemical functionalities into the surface chemistry of these coatings in order to evaluate the effectiveness of a stable free radical in preventing permanent fouling of marine organisms.

Synthesis of Materials

Synthesis of (PS-PDMS) Macroinitiator

This research used the same PS-PDMS based macroinitiator to synthesize all copolymers (figure 2). Styrene monomer and then hexamethylcyclotrisiloxane (D3) monomer were sequentially polymerized via anionic polymerization to create a diblock copolymer. In an anaerobic chamber under nitrogen, 250 mL (3.896 mmol) of the initiator sec butyllithium was dissolved in 45 mL distilled benzene. 5 mL (52.8 mmol) styrene monomer was added and allowed to stir for 24 hours at room temperature in the anaerobic chamber. After the styrene had polymerized, samples were taken for ^1H NMR and GPC, and five times excess D3 monomer was added to the reaction to form the PDMS polymer block. Following another 24 hours in the anaerobic chamber stirring at room temperature, distilled tetrahydrofuran (THF) was added in a 1:3 ratio of THF:benzene already in the reaction. The PS-PDMS block copolymer was samples and then capped with the ATRP initiator by adding excess 2-bromo-

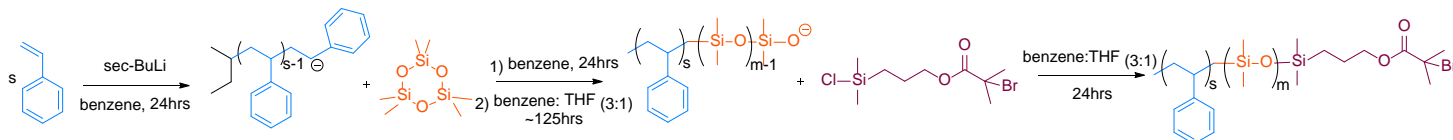


Figure 2 | Synthesis of PS-PDMS Macroinitiator

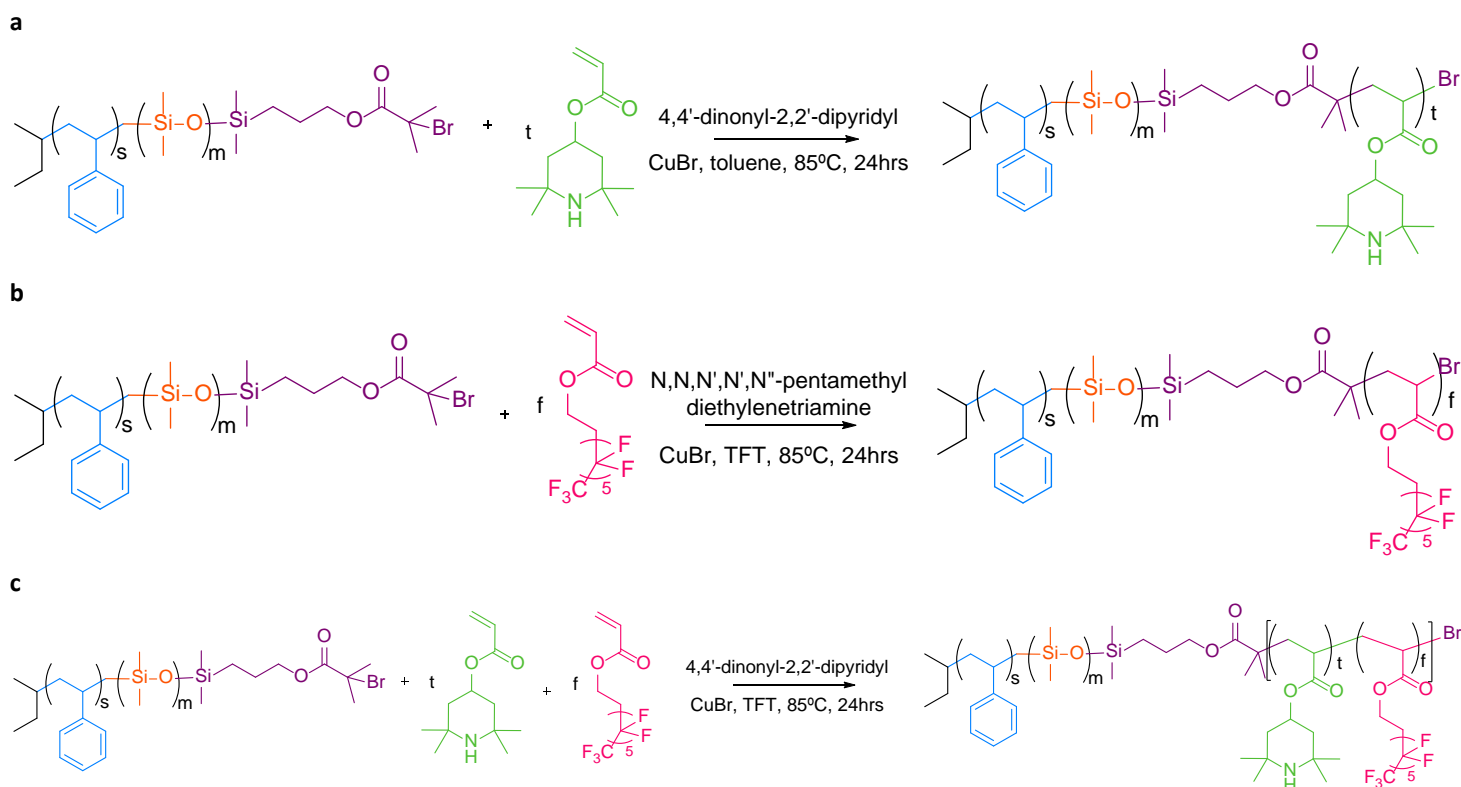


Figure 3 | Syntheses of pTEMPO and MAF6 block copolymers from PS-PDMS macroinitiator. a, Polymerization of pTEMPO. b, Polymerization of MAF6. c, Copolymerization of pTEMPO and MAF6

2-methylpropionic acid dimethylchlorosilylpropyl ester to react under continuous stirring at room temperature for 24 hours.

Polymerization

The different monomers were polymerized from the PS-PDMS macroinitiator with atom transfer radical polymerizations (ATRP) reactions. Polymerizations were carried out with similar conditions where deviations were taken only in the batch of macroinitiator, solvent (dependent on if MAF6 was being polymerized), and the ligand (dependent on if pTEMPO was one of the monomers).

Unless described differently in the following sections for each polymer and copolymer synthesized, the conditions used were as follows. Macroinitiator, monomer or monomers, and ligand were dissolved together in a Schlenk tube with solvent, either toluene or trifluorotoluene (TFT). This solution was run through three Freeze-Pump-Thaw-Backfill cycles to displace the oxygen in the tube with nitrogen. After the three successive cycles, 20 mg of Cu(I)Br was quickly transferred into the tube and the solution was again Freeze-Pump-Thaw-Backfilled three times. The reaction solution was then heated to 85°C and set stirring to react for 24 hours. The reaction solution was then washed three times with saturated sodium

bicarbonate solution and three times with deionized water (DI water) to wash away impurities from the solution such as copper. The remaining polymer solution was precipitated dropwise into methanol (MeOH). The polymer solids were filtered, collected, and dried under reduced pressure overnight at 55°C.

pTEMPO Polymerization

2.0 g (0.048 mmol) of the PS⁷PDMS³⁵ macroinitiator, 0.71 g (3 mmol) of the monomer 2,2,6,6-tetramethyl-4-piperidyl methacrylate, the monomer precursor to TEMPO, (pTEMPO), and the 6.8 mg (0.048 mmol) of the ligand 4,4'-dinonyl-2,2'-dipyridyl were dissolved in a Schlenk tube with 10 mL of toluene. 20 mg of Cu(I)Br was used to form the copper complex for the ATRP reaction. The solution became amber in color upon addition of the copper, but, when heated, the solution turned green-brown until it was washed. See polymerization reaction in figure 3a.

MAF6 Polymerization

1.98 g (0.047 mmol) of the PS⁷PDMS³⁵ macroinitiator, 1.17 mL (4 mmol) of the monomer 3,3,4,4,5,5,6,6,7,7,8,8,8-tridecafluorooctyl methacrylate (MAF6), and 50 μ L (0.047 mmol) of the ligand N,N,N',N',N''-pentamethyldiethylenetriamine were dissolved with 10 mL of trifluorotoluene (TFT) in a Schlenk tube. Three Freeze-Pump-Thaw-Backfill

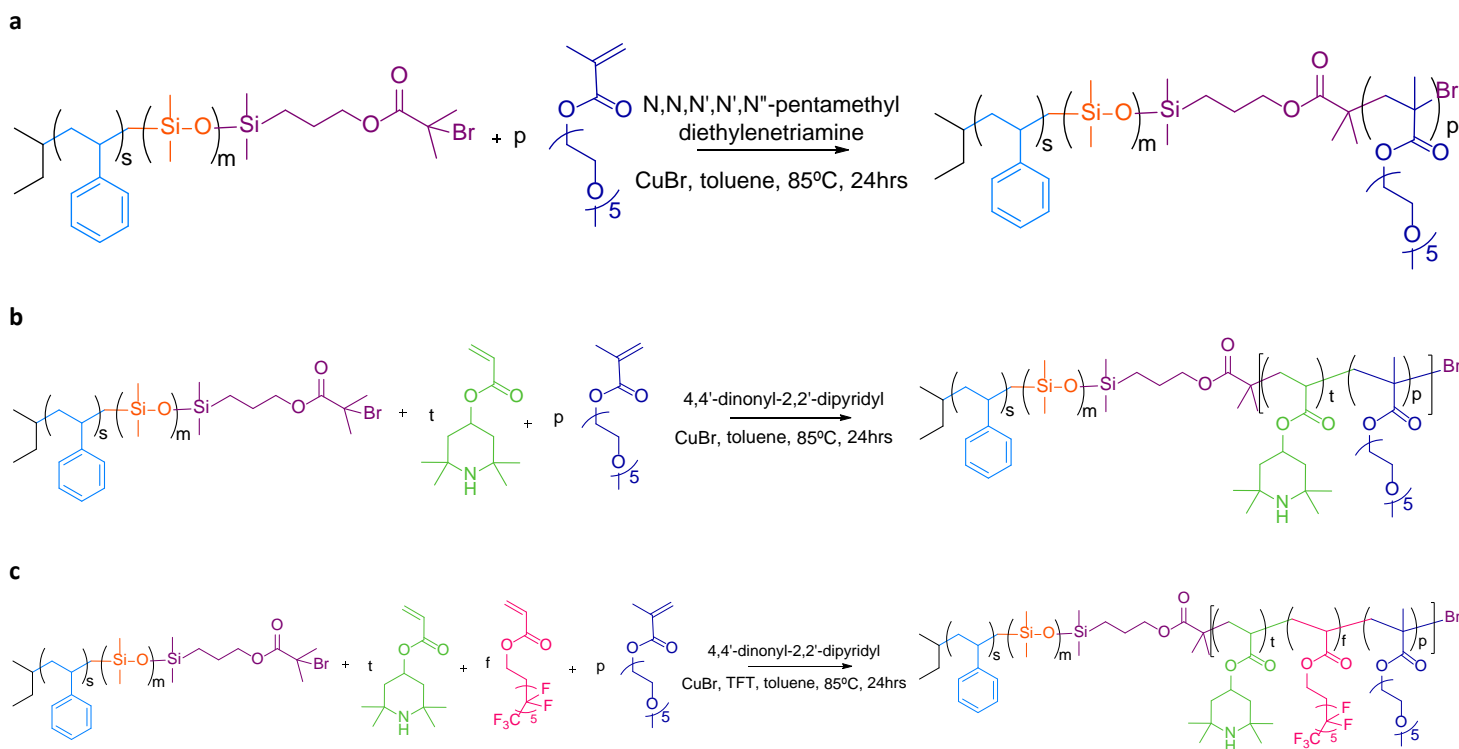


Figure 4 | Syntheses block copolymers incorporating PEGMEMA from PS-PDMS macroinitiator. a, Polymerization of PEGMEMA. **b,** Copolymerization of pTEMPO and PEGMEMA. **c,** Copolymerization of pTEMPO, MAF6, and PEGMEMA

cycles were run with the solution before 20 mg of Cu(I)Br was transferred into the solution and it was again Freeze-Pump-Thaw-Backfilled three times. The reaction solution was set stirring for 24hrs at 85°C to react. The polymer was then precipitated into excess MeOH and set stirring overnight to remove copper and any other impurities from the solution. To further remove these impurities, the polymer was filtered, re-dissolved in dichloromethane (DCM) and some TFT. The polymer was then again precipitated into excess MeOH and left stirring overnight. The collected polymer solids were dried under reduced pressure overnight at 55°C. See polymerization reaction in figure 3b.

pTEMPO and MAF6 Copolymerization

4.0 g (0.095 mmol) of the PS⁷PDMS³⁵ macroinitiator, 0.71g (3 mmol) of the monomer pTEMPO, 0.88 mL (3 mmol) of the monomer MAF6, and the 13.5 mg (0.095 mmol) of the ligand 4,4'-dinonyl-2,2'-dipyridyl were dissolved in a Schlenk tube with 20 mL of TFT and 10% toluene by volume. For the copper complex, 40 mg of Cu(I)Br was added, whereupon the solution turned dark brown, almost green, in color. See copolymerization reaction in figure 3c.

PEGMEMA Polymerization

2.0 g (0.043 mmol) of the PS¹²PDMS³⁹ macroinitiator, 0.86 mL (3 mmol) of the monomer PEGMEMA, and the 50 μ L

(0.047 mmol) of the ligand N,N,N',N',N''-pentamethyldiethylenetriamine were dissolved with 10 mL toluene in a Schlenk tube. 20 mg of Cu(I)Br was added to the reaction solution. After reacting for 24 hours, the solution was washed over an alumina gel to remove the impurities, especially copper, with toluene followed by DCM. The filtered solution was concentrated through rotary evaporation, and then the concentrated solution was precipitated into excess MeOH. The polymer precipitate was filtered, collected, and dried at 55°C under reduced pressure. See polymerization reaction in figure 4a.

pTEMPO and PEGMEMA Copolymerization

4.0 g (0.086 mmol) of the PS¹²PDMS³⁹ macroinitiator, 0.74g (3 mmol) of the monomer pTEMPO, 0.86 mL (3 mmol) of the PEGMEMA monomer, and 12.8 mg (0.086 mmol) of the ligand 4,4'-dinonyl-2,2'-dipyridyl were dissolved in a Schlenk tube with 20 mL of toluene. 40 mg of Cu(I)Br was added to create the copper complex. See polymerization reaction in figure 4b.

pTEMPO, MAF6, and PEGMEMA Copolymerization

4.0 g (0.086 mmol) of the PS¹²PDMS³⁹ macroinitiator, 0.62g (2.8 mmol) of the monomer pTEMPO, 0.6 mL (2 mmol) of the PEGMEMA monomer, 0.6 mL (2 mmol) of the MAF6 monomer, and 12.8 mg (0.086 mmol) of the ligand 4,4'-dinonyl-2,2'-dipyridyl were dissolved in a Schlenk tube

with 20 mL of TFT and 10% toluene by volume. For the copper complex 40 mg of Cu(I)Br was added. See polymerization reaction in figure 4c.

Sample Preparations

Slides were initially cleaned with piranha and functionalized with 10 drops of glacial acetic acid and 8 mL of (3-aminopropyl)trimethoxysilane. After a 12 hour drying process at 120°C under reduced pressure, the slides were spin coated with two layers of the elastomeric triblock styrene-ethylene butadiene-styrene (SEBS). The first layer was made of 6% by weight SEBS polymer dissolved in toluene and stirred until the solution was homogenous. This first layer was annealed for 12 hours at again 120°C under reduced pressure. A second layer of 12% by weight SEBS in toluene was coated on in three iterations to get a substantial amount of the SEBS layer on the sample slides. Following this tri-coat second layer, the slides were again annealed for 12 hours at 120°C under reduced pressure.

To add the designed surface chemistry, SABC samples were spray coated on to the SEBS coated slides as seen in the diagram in figure 5. Nearly all of each polymer was used in this process, so the amount used was primarily a reflection of how much was left. The polymer was dissolved in dichloromethane (DCM) and evenly sprayed onto sample slides. The spray coated slides were then annealed under reduced pressure for 12 hours at 120°C.

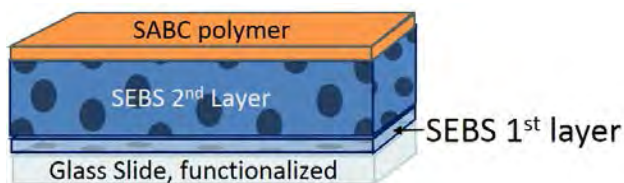


Figure 5 | Diagram of polymer layers for sample prep.

Characterization

¹H Nuclear Magnetic Resonance

¹H NMR spectra were measured in deuterated chloroform with a Varian Gemini spectrometer at 400MHz.

Gel Permeation Chromatography

GPC was measured in THF with a Waters Ambient Temperature GPC equipped with a Waters 410 differential refractive index detector and a Waters 486 UV-Vis detector. Machine was calibrated with polystyrene standards.

X-ray Photoelectron Spectroscopy

XPS of dry surfaces was measured with an ultrahigh vacuum system (UHV) Surface Science Instruments (SSI) SSX-100 XPS. SSI XPS instrument has an operating pressure of $<2 \times 10^{-9}$ and is equipped with x-ray sources producing monochromatic AlK α rays at 1486.6 eV. Photoelectrons collected at a 55 degree angle from the surface normal before entering the 180-degree hemispherical analyzer and being detected by the SSI Position Sensitive Detector.

Results and Conclusions

Previous research has proven the effectiveness of PDMS-based antifouling coatings. However, these coatings are still imperfect at preventing marine organism adhesion via protein crosslinking. Herein a set of surface active block copolymers incorporating stable free radicals were systematically designed and synthesized to interfere with this crosslinking. Fluoroalkyl methacrylate was copolymerized with the free radical methacrylate in order to achieve surface segregation of block copolymers in a PDMS network, bringing the free radicals to the surface [10, 11]. Additionally PEG methacrylate, shown to prevent protein adsorption, was copolymerized with only the free radical methacrylate and with both the free radical methacrylate and fluoroalkyl methacrylate.

NMR confirmed the synthesis and controlled chemical composition of each polymer. The relative control of each blocks molecular weight and PDI were observed with GPC. The molecular weight and PDI for each polymer synthesized were as follows in figure 6, showing that comparative amounts of each block was polymerized.

Surface chemistry was controlled by logically varying the block copolymer chemistry. As shown in the XPS of the dry block copolymer coating surfaces in figure 7, samples

Polymer	Mn PS (kDa)	Mn PDMS (kDa)	Mn ATRP (kDa)	Mn total (kDa)
PS-PDMS-pTEMPO	7	35	11	53 (PDI 1.14)
PS-PDMS-Fluoro	7	35	18	60 (PDI 1.14)
PS-PDMS-(pTEMPO, Fluoro)	7	35	14	56 (PDI 1.13)
PS-PDMS-PEGMEMA	12	39	15	66 (PDI 1.42)
PS-PDMS-(pTEMPO, PEGMEMA)	12	39	NA	NA
PS-PDMS-(pTEMPO, Fluoro, PEGMEMA)	12	39	21	72 (PDI 1.23)

Figure 6 | Table of molecular weight of each block for each polymer synthesized.

showed predominantly PDMS at the surface except for the fluoroalkyl rich polymer where fluorine replaced some of the PDMS at the surface.

This research shows that SABC polymer coatings combining stable free radicals, fluoroalkyl groups, and PEG groups can be synthesized. Additionally, by varying the chemical composition, the fluoroalkyl groups were shown to rise up to the surface.

Future Work

This set of surface active block copolymers will continue to be characterized for a more complete analysis of each surface. XPS will be conducted with samples after being submerged in DI water for 72 hours to determine the surface environment. Water bubble contact angle will be measured over multiple days to study the wettability of the polymer coatings. To evaluate performance as antifouling and high fouling release coatings the coatings will be subjected to bioassays using *Ulva Linza*, a marine algae, and *Navicula*, a marine diatom.

Additionally, a potentially more robust synthesis scheme based on thiolene click attachment of the stable free radical will be researched and evaluated as an alternative to the synthesis here.

Acknowledgements

I would like to thank Brandon Wenning, Amanda Leonardi, Alicia Cintora, Chris Ober, and the Ober lab for their help and support with this project. This project was part of the Office of Naval Research Coatings/Biofouling Program supported by the Office of Naval Research. This work was supported in part by the Cornell Center for Materials Research with funding from the Research Experience for Undergraduates program (DMR-1063059 and DMR-1120296). This work made use of the Cornell Center for Materials Research Shared Facilities which are supported through the NSF MRSEC program (DMR-1120296).

References

- [1] Schultz, M. P.; Bendick, J. A; Holm, E. R.; Hertel, W. M. *Biofouling* **2011**, *27* (1), 87–98.
- [2] Townsin, R. L. *Biofouling* **2003**, *19*, 9–15.
- [3] Corbett, J. J. *J. Geophys. Res.* **2003**, *108*, 4650.
- [4] Salta, M.; Wharton, J. A.; Stoodley, P.; Dennington, S. P.; Goodes, L. R.; Werwinski, S.; Mart, U.; Wood, R. J. K.; Stokes, K., R. *PHILOS T ROY SOC A* **2010**, *368*, 4729–4754
- [5] Champ, M. A. *Mar. Pollut. Bull.* **2003**, *46* (8), 935–940.

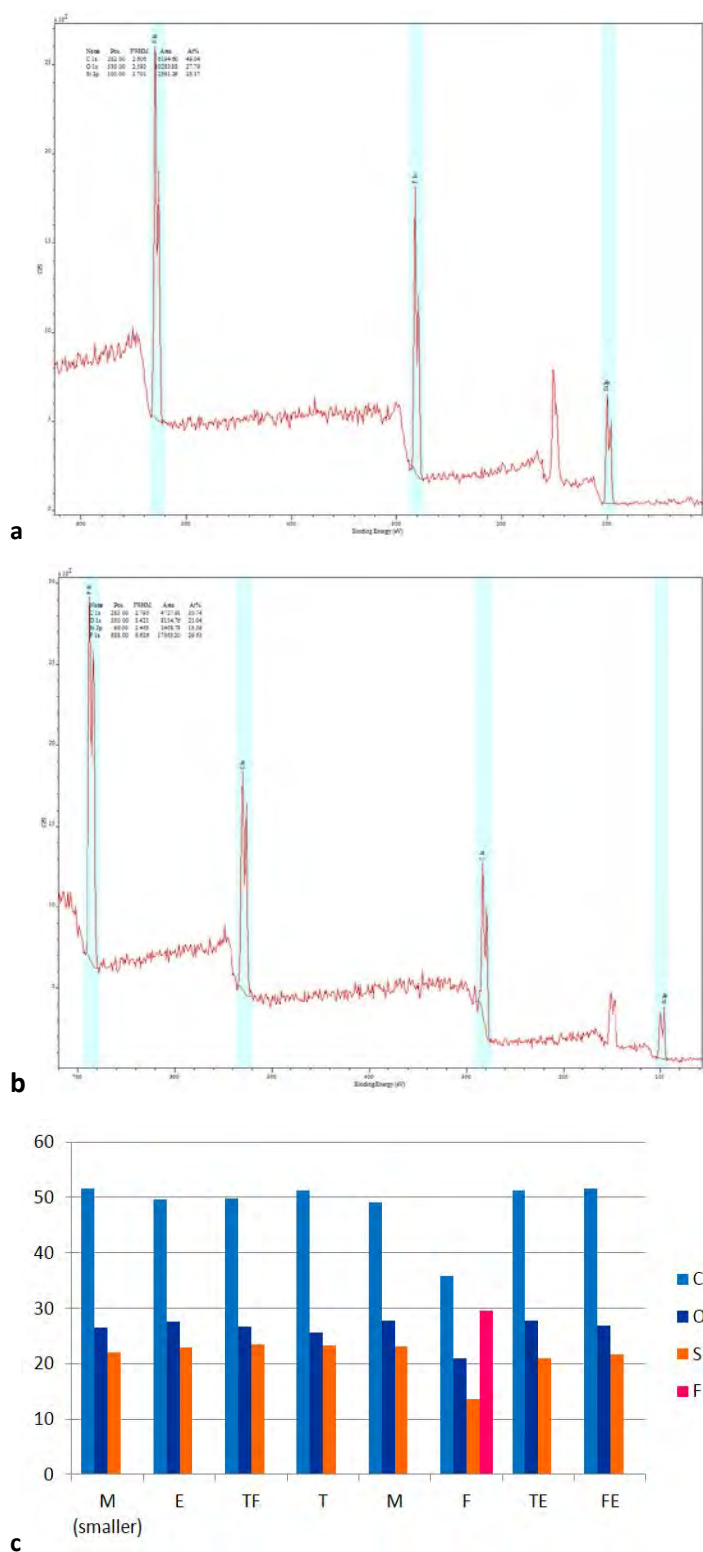


Figure 7 | XPS of dry SABC surfaces. **a**, Dry XPS of PS-PDMS showing only PDMS at the surface. **b**, Dry XPS of PS-PDMS-MAF6 where fluoroalkyl groups replaced some of the PDMS. **c**, Dry XPS surface composition by percent where only F (PS-PDMS-MAF6) shows surface chemical composition other than PDMS.

[6] Haras, D. *Mater. Tech.* **2005**, *93*, s.27-s.41

[7] Zhang, Z.; Finlay, J. A.; Wang, L.; Gao, Y.; Callow, J. A.; Callow, M. E.; Jiang, S. *Langmuir* **2009**, *25* (23), 13516–13521.

[8] Krishnan, S.; Weinman, C. J.; Ober, C. K. *J. Mater. Chem.* **2008**, *18* (29), 3405.

[9] Gudipati, C. S.; Finlay, J. a.; Callow, J. A.; Callow, M. E.; Wooley, K. L. *Langmuir* **2005**, *21* (7), 3044–3053.

[10] Cho, Y.; Sundaram, H. S.; Finlay, J. A.; Dimitriou, M. D.; Callow, M. E.; Callow, J. A.; Kramer, E. J.; Ober, C. K. *Biomacromolecules* **2012**, *13* (6), 1864–1874.

[11] Calabrese, D. R.; Wenning, B.; Finlay, J. A.; Callow, M. E.; Callow, J. A.; Fischer, D.; Ober, C. K. *Polym. Adv. Technol.* **2015**, p. n/a–n/a.

Measuring the Spin Hall Effect and Applying Strain

Orion Guan, Neal Reynolds, Greg Stiehl, John Heron, Dan Ralph*

Cornell Center for Materials Research

Cornell University, Ithaca, New York 14853, U.S.A

(Dated: July 30, 2015)

The spin Hall ratio of a 10nm layer of platinum grown on PbMgNbO_3 - PbTiO_3 is measured while applying biaxial compressive strain. The spin Hall ratios are calculated by (1) measuring the 2nd harmonic Hall voltage of a ferromagnetic layer of permalloy above the platinum and (2) using the Magneto-Optical Kerr Effect. These techniques are used to determine the spin torque exerted on the permalloy. Strain is applied using an electric field to tense the PMN-PT vertically. The results show signs that compression has an effect on the spin Hall ratio of platinum. When the Kerr Effect is measured while compression is applied, the results don't show such a relationship. However, there were mysterious problems with the experiment that are worthy of note for future experiments.

I. INTRODUCTION

Magnetoresistance Random Access Memory (MRAM) is a data storage technique in which ferromagnets' magnetizations are changed in order to store and rewrite information. It has the potential to be a fast, stable, and cost effective form of data storage. In order to effectively manipulate a ferromagnet without using another magnet, there is use for a phenomenon that can use electric current to flip magnetization. [1]

There is such a phenomenon. When a current is sent through certain conductors such as platinum, the Spin Hall Effect (SHE) diverts electrons of opposite spins, creating a spin current on the lateral surfaces of the conductor. Spin current is the current of electrons of a given spin subtracted from the current of electrons of the opposite spin. The generation of spin current can induce a change in magnetization in nearby materials, by a phenomenon known as *spin-transfer torque*, or simply spin torque.

The efficiency by which metals such as platinum generate spin current is measured in a parameter characteristic of the metal, called the spin Hall angle of the metal, or the *spin Hall ratio* (henceforth SHR). It is the ratio of the generated spin current to the initial current sent through the conductor. If the SHR of a conductor were to be artificially raised somehow, then the generation of spin transfer torque would be stronger for a given current.

Strain, the compression and tension of a material from its equilibrium shape, can change electrical and magnetic properties. Therefore, it's quite possible that strain could have an effect on the SHR of a conductor.

SHR can be calculated by measuring spin torque. When AC current is sent through platinum, it is easier to detect and measure tiny spin torques that turn magnetization at the frequency of the current. This is a basis for the setup of two methods of measuring spin torque: The 2nd harmonic Hall voltage of the ferromagnet, and the Magneto-Optic Kerr Effect.

II. METHODS AND SETUP

In my experiments, I use a "bar" with two layers of material, a ferromagnet on top of a conductor. The ferromagnet is an alloy (80% Fe, 20% Ni), known as permalloy, while the conductor is platinum. This "bilayer" rests on a thick (millimeter) sheet of PMN-PT.

II.1. Method 1: 2nd harmonic Hall voltage.

The (ordinary) Hall Effect occurs when charge carriers move through a magnetic field and change directions, creating a voltage difference between sides of the conductor. Similar types of Hall effects, the Anomalous and Planar Hall Effects, work in ferromagnets. Only instead of magnetic field, it is the magnetization that results in "Hall voltage".

Spin torque rotates a ferromagnet's magnetization, which results in changes to a ferromagnet's resistance. Thus the Hall voltage is affected by two things that vary at AC frequency: the "Hall resistance" and the current itself. Since $V = IR$, the math shows that spin torque affects the Hall voltage at *twice* the AC frequency, or in other words, at the 2nd harmonic.

The spin torque on the ferromagnet depends a cross product between the its magnetization and the impinging spin. An magnetic field (henceforth just "field") is used to change and maintain magnetization. If the magnetization were to reverse, then so too will the spin torque's influence on the ferromagnet. This shows up as a difference between constant terms in the Hall voltage when field points one way and when it points the other.

To relate measured Hall voltage to the size of the spin torque, a calibration scan is also done with field perpendicular to the permalloy's surface, measuring at AC frequency. This determines parameters such as permalloy's anisotropy (magnetization's directional favoritism). In theory, the Hall voltage should vary linearly with field and measuring this slope provides the factors we need [2].

* og2517@truman.edu, ndr37@cornell.edu, gms263@cornell.edu, jth247@cornell.edu, ralph@ccmr.cornell.edu

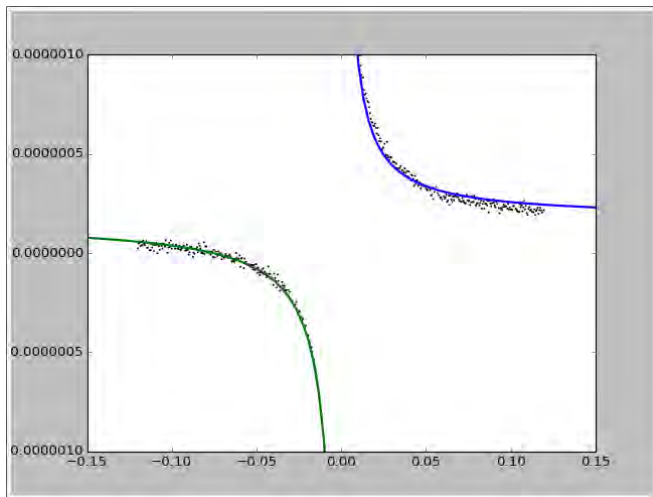


FIG. 1. The 2nd harmonic of the Hall voltage contains a “ $1/x$ ”-like term, as well as a subtle constant difference between the left and right sides. This constant difference is directly proportional to the SHR. Hall voltage is measured every 0.0005 T.

II.2. Method 2: Magneto-Optical Kerr Effect

The Magneto-Optical Kerr Effect, or MOKE, describes a phenomenon in which a magnetized ferromagnet rotates the polarization of the light it reflects. When the laser is incident at a normal angle to the ferromagnet, the change in polarization is most sensitive to magnetization perpendicular to the ferromagnet, a phenomenon called perpendicular MOKE or PMOKE. Instead of measuring Hall voltage, we use a 405 nm laser and a Wollaston prism to measure this component of the magnetization.

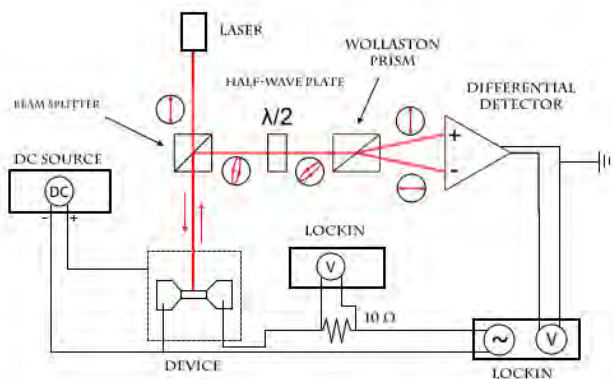


FIG. 2. Diagram for strain application while measuring SHR using the MOKE technique.

The setup is depicted in Fig. 2. Half-wave plates are rotated to ensure the light incident at the differential detector’s photodiodes are close to equal in magnitude. Ro-

tations of polarization by the Kerr Effect are then measured by differences in the two light intensities.

A scanning mirror turns to guide a laser beam to move along the sample, crossing the permalloy in a path perpendicular to the direction of current. One of these “scans” takes data from when the laser is not on the permalloy as well as data from when the laser does reflect off of permalloy.

Just as in measuring the 2nd harmonic, the direction of the spin torque will reverse when the magnetization is reversed. Magnetization will rotate in the opposite direction in addition to flipping 180° . Spin torque’s effect on out-of-plane magnetization will have the opposite sign. The laser scan is repeated with field pointing in the opposite direction, and the sum and difference between the two scans are taken.

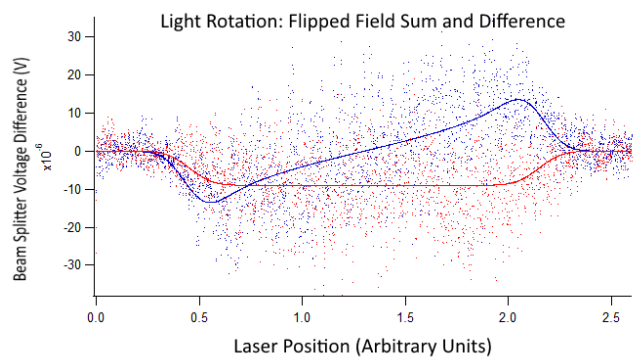


FIG. 3. The laser arrives at permalloy at around 0.5 units, and leaves permalloy at around 2.1. The **difference** between flipped-field scans is in red. The **sum** is in blue. This data was taken from an experiment by Alex Mellnik [1].

Fig. 3 depicts an ideal result of adding and subtracting scans. The **difference** (red) depicts the spin torque. The **sum** (blue) depicts anything that isn’t affected by external field direction, most apparently the field generated by the AC current itself. Luckily, the **sum** clearly tells us when the laser is hitting permalloy, as well as other useful information needed to interpret the **difference** graph.

II.3. Applied Strain

To compress the platinum, we create a potential difference, or backgate voltage, between the bilayer and the bottom of the PMN-PT. The vertical electric field tenses the PMN-PT, which ends up compressing the bilayer horizontally to preserve overall volume. Qualitative details of the compression are discussed in the Data Presentation section. When electric field overcomes the polarization of the PMN-PT, for a brief moment the bilayer is tensed rather than compressed. During this time the change in SHR can be observed to further establish a relationship to strain. Figs. 2 and 11 show circuit diagrams of each

measurement method used.

III. PROCEDURE

III.1. 2nd Harmonic

The sample of PMN-PT/Pt/Py is set up so that an AC current runs through the bar and Hall voltage difference of the sides can be measured. The geometry is shown in Fig. 4.

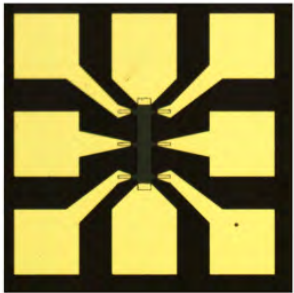


FIG. 4. The bilayer bar of platinum and permalloy is located in the center. The other eight features are conductive platinum surfaces connected to the bar. The top and bottom pads are normally connected to an AC current source. The left and right pads connect to a voltmeter to determine Hall voltage.

At some point, magnetic field will be sent in the same direction as the current in the bar. To figure out the exact direction of the bar, a magnetic field's direction is rotated in-plane (horizontally) and the Hall voltage recorded. The Planar Hall Effect changes the magnetoresistance as a function of field along the bar. As a result, the Hall voltage increases as $\sin(2\phi)$ where ϕ is the angle between the field and the bar. Thus the bar's azimuthal position can be found. Fig. 5 shows an example.

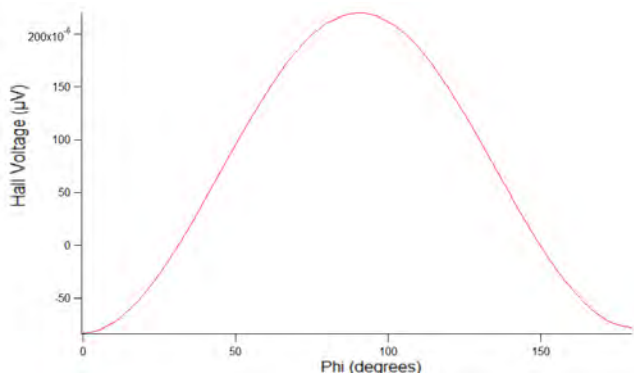


FIG. 5. The Planar Hall Effect causes the Hall voltage at AC frequency to go as $\sin(2\phi) + C$ where ϕ is the angle with respect to the bar. The bar in this figure is currently oriented close to $\phi = 45$.

Lock-in amplifiers produce the needed AC current at

4519.0 Hz and measure the 1st and 2nd harmonics of Hall voltage. A high prime number is used to reduce resistance due to capacitance and to prevent interference from outside sources of oscillating field at lower frequencies. The magnetic field is gradually swept from $-.12$ to $.12$ Teslas along the direction of current in the bar, with an arbitrary positive direction. The 2nd harmonic Hall voltage, 90° out of phase, is recorded. A second sweep is done $.12$ T downward to $.12$ T upward (vertically, out-of-plane), with a slight 1° tilt along the length of the bar in the in-plane positive direction when the field points upward. This allows the anisotropy terms in the Hall voltage to have the correct sign. In this scan the 1st harmonic is recorded.

Hayashi [2] predicts that the Hall voltage in the first and second harmonics will go as Eqns. 1 and 2 respectively. By fitting to versions of these equations that match our setup, (Eqns. 3 and 4 respectively), spin torque's effects can be analyzed and the spin Hall ratio calculated using Eqns. 5 and 6.

$$V_\omega \approx -\frac{1}{2} \Delta R_A \frac{H \cos \theta_H}{(H_K - H_A \sin^2 \phi_H) - H \sin \theta_H} \Delta I \quad (1)$$

$$V_{2\omega} \approx -\frac{1}{2} \left[\frac{1}{2} \Delta R_A \frac{\Delta H_z}{-(H_K - H_A \sin^2 \phi_H) + H \sin \theta_H} - \Delta R_P \frac{\Delta \tilde{H}_{IN} \cos 2\phi_H}{-H_A \cos 2\phi_H + H \sin \theta_H} \right] \Delta I \quad (2)$$

$$V_\omega \approx -\frac{1}{2} \frac{\Delta R_A \Delta I}{H_K} H \cos \theta_H \quad (3)$$

$$V_{2\omega} \approx \frac{1}{4} \frac{\Delta R_A \Delta I}{H_K} \Delta H_z + \frac{A}{H + B} \quad (4)$$

$$\Delta H_z = a \sin \theta \cos \phi \quad (5)$$

$$a = \frac{\hbar \theta_{SHE} J_C}{2e M_s t_f} \quad (6)$$

Eqns. 1 and 2 are the Hall voltage coefficients for the 1st harmonic and the 2nd harmonic 90° offset. H is the applied field in a given θ and ϕ direction. The ΔR terms are permalloy's Anomalous and Planar Hall Effect parameters, H_K and H_A are anisotropy terms, and ΔI refers to the magnitude of the current. ΔH_z is the effective out-of-plane field. A and B are other fitting parameters. θ_{SHE} is the spin Hall ratio, \hbar the reduced Planck constant, J_C the amplitude of AC current density through the layer exhibiting Spin Hall Effect, e the fundamental charge, M_s is the saturation magnetization of the ferromagnet, and t_f is the ferromagnet thickness.

It can be seen in Eqn. 5 that ΔH_z will flip sign when the in-plane field reverses, resulting in a constant difference between the left and right sides of Fig. 1.

Another lock-in is used to measure the voltage drop across a resistor to determine the current, and yet another to measure the voltage drop across the bar to determine the resistance, revealing current density through the bar.

To apply an electric field through PMN-PT, the bottom of PMN-PT is connected to a lead while one of the pads near the bar is connected to floating ground. A DC voltage difference is added to the AC current. It is assumed that the electric field from the bottom of the PMN-PT and the device will be approximately vertical.

III.2. MOKE

As AC current runs through the bar, a laser is directed to move laterally across it as a lock-in amplifier measures the polarization change using a Wollaston prism and differential detector. Half-wave plates are adjusted so that the beam splitter splits the beam almost equally, so polarization rotations show up prominently.

Voltage is fed to a mirror which moves to guide the position of the laser. This voltage serves as the independent variable of the scan, and is arbitrary in scale. The path of the laser is designed to avoid platinum leads, only reflecting off of PMN-PT and the permalloy bar. The .05 T magnitude of the applied field is chosen to saturate the magnetization of the bar.

Once both positive field and negative field scans are complete, the data values are summed and the difference taken to make two new graphs. The sum is fit to the Oersted field out-of-plane magnetization convolved with a 2D Gaussian laser beam profile. This gives an assessment of what data actually corresponds to the laser hitting the bar, where the bar is, how fast the laser moves, and the scale of the photodiode differentiator's signal. Combined with the fit to the difference graph, the spin Hall ratio can be calculated using the procedure detailed in Mellnik's paper [1].

To apply strain, an electric field is applied in the same way as it is in the 2nd harmonic method.

IV. DATA PRESENTATION

In order to present the effect that strain has on SHR, we must know when compression and tension occur, and to what degree. When the backgate voltage reaches a certain magnitude, a flutter in platinum's strain-based resistance (piezoresistance) can be measured. Possibly, when the polarization of PMN-PT is overcome by an external electric field, the platinum becomes briefly tensile, as shown in Fig. 6a [3].

The assumptions behind how PMN-PT reacts to strain are as such: As magnitude increases from 0, the electric

field increases until it overcomes the polarization of the material. In this window, the platinum is tensile rather than compressed.

We want to find out what happens to the SHR at this point especially.

The piezoresistance curve of the bar is shown in Fig. 6b. Unexpectedly, the curve is not remotely symmetric around 0 volts.

IV.1. Piezoresistance

To find out more about the strain-based trends that occur in the bilayer, piezoresistance curves were made on slightly different bars. For example, the piezoresistance curve of a bar without any permalloy is shown in Fig. 6c.

The linearity seen in this curve does not show up in a third sample, this one omitting platinum. That sample shows no discernible piezoresistance (Fig. 6d).

IV.2. 2nd Harmonic

Fig. 12 in the appendix depicts the voltage drop across a resistor as a percentage throughout the experiment, to show that the current through the platinum remained stable.

As shown in Fig. 7, the SHR fluctuations are linear from -500 volts to 500 volts, reflecting the mysterious property from the platinum-only sample. Additionally, there is a fluctuation at around 300V when the electric field is increasing. Each data point is taken based on 20 minutes of sweeping.

Fig. 8 shows the same graph, only each data point is modulated to compensate for changing piezoresistance. It has been shown that resistance will rapidly change at the fluctuation point. This graph, however, suggests that SHR does as well.

The spin Hall ratios themselves are concerning because they deviate far from expected values for platinum, which tend to hover around 0.07 [1] [4].

IV.3. MOKE

It may be important to note that since the recording of the data in all previous graphs, the PMN-PT was cut down to 71.6% of its original thickness, which would strengthen the electric field generated by a given backgate voltage.

The SHR values are presented in Fig. 9. The experiment behind these results is dubious due to extraneous curves that tend to appear in the data, as shown in Fig. 10. Compare to Fig. 3.

The data collected through MOKE also deviates far from expected SHR values. They are consistently two orders of magnitude lower than .007.

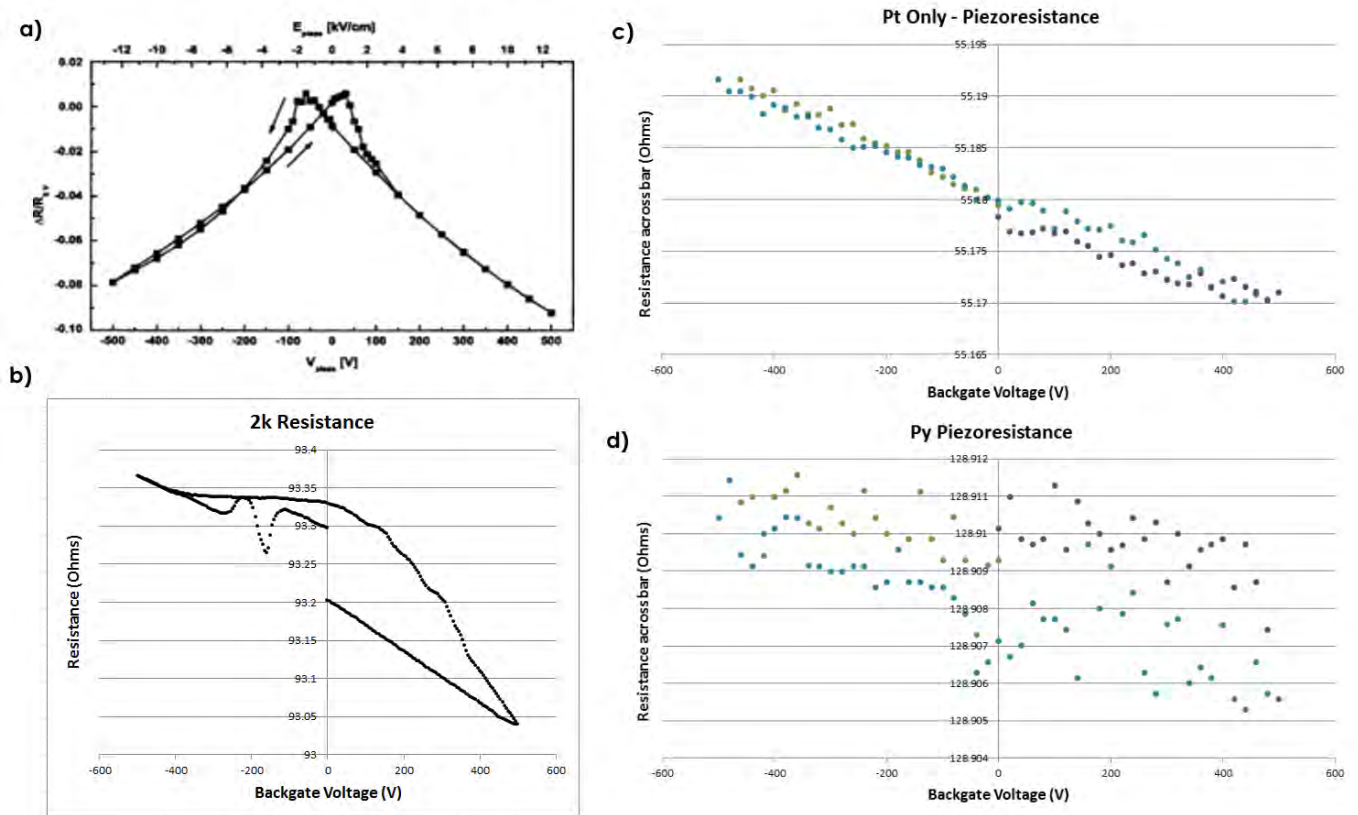


FIG. 6. a) The shape of a strain curve of PMN-PT, symmetric about when there is no applied electric field. As magnitude increases from 0, electric field has to overcome the polarization of PMN-PT, so it rises before rapidly falling once the PMN-PT becomes accustomed [3]. b) The resistance across the bilayer increases and decreases with applied strain. This measurement was done over the course of an hour. c) The relationship between backgate voltage and resistance across a bar of 15nm platinum and no permalloy. The backgate voltage starts from 0V to -500V (green path) and ends going from 500V to 0V (purple path). Data averaged over several runs. d) A similar measurement on 15nm permalloy on 25nm aluminum.

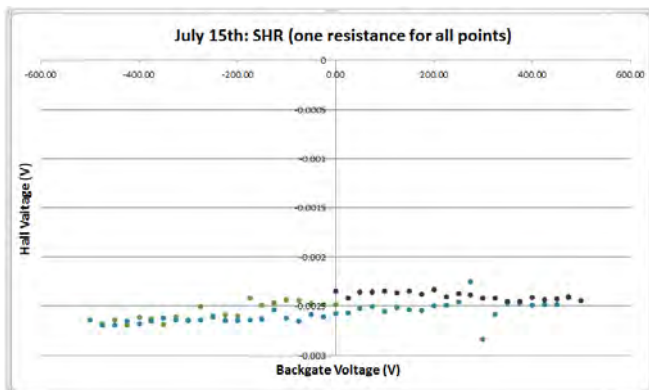


FIG. 7. The piezoresistance is not taken into account in these calculations of SHR.

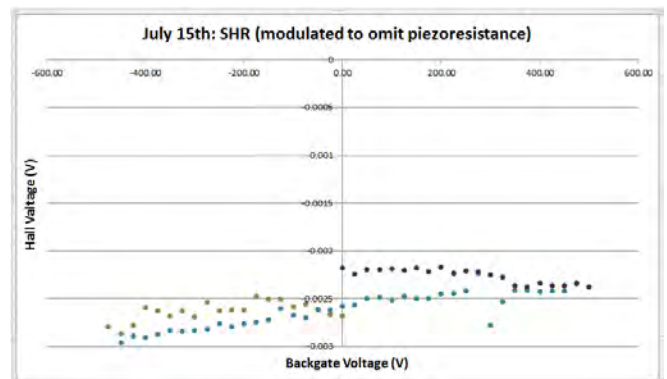


FIG. 8. The piezoresistance is measured and each data point modulated to compensate. Signs of a relationship between strain and SHR include a flutter at around 300V.

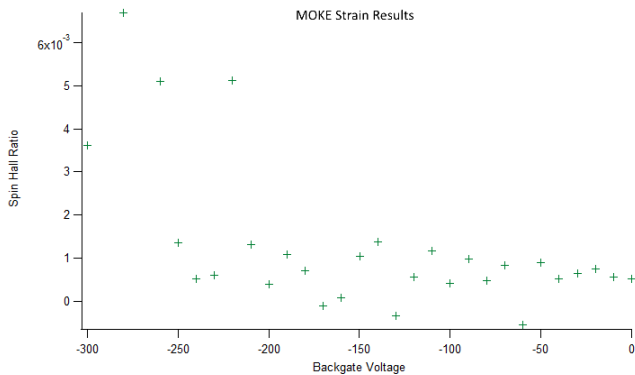


FIG. 9. The SHRs calculated from scan pairs done at all voltages between 0V and -300V in 10-volt steps.

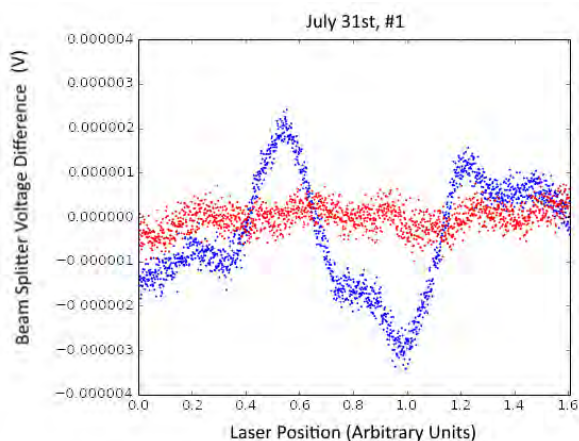


FIG. 10. The sum and difference of scans of opposite fields for one pair of scans in this experiment. The extra curves to the left and right of the graph may skew the fitting algorithm.

V. CONCLUSION AND CONTINUATION

We applied compression to platinum during measurements of the 2nd harmonic Hall voltage. The spin Hall ratio seemed to change as the bar was strained. However, the correlation to PMN-PT strain is inconsistent in at what electric field it occurs and in direction. In a cursory look at how strain changes SHR as measured using MOKE, no relationship could be found, but there were apparent problems with the MOKE method that have not been worked around. Additionally, in both methods, the spin Hall ratios don't seem to be accurate.

This research can be improved upon by applying stronger electric fields to overcome the polarization of PMN-PT. For the MOKE setup, extraneous fluctuations in the Kerr Effect should be tested and the experiment adjusted to avoid them. MOKE could use a more focused laser, so that less light reflects off of nearby platinum surfaces, for example. These experiments could also measure spin Hall ratio with other conductors and ferromagnets, and show a different strain relationship.

ACKNOWLEDGMENTS

I would like to thank Neal Reynolds for his steadfast guidance during these experiments, as well as Greg Stiehl, John Heron and Dan Ralph for their assistance. My participation would not have been possible without a grant from the National Science Foundation, funding from MRSEC, and an REU by Cornell Center for Materials Research, grant numbers DMR-1063059 and DMR-1120296.

-
- [1] Mellnik, A. R. *Measurements of Spin Torques Generated by Topological Insulators and Heavy Metals*. Cornell University. May 2015.
 - [2] Hayashi et al. *Quantitative characterization of the spin orbit torque using harmonic Hall measurements*. Phys. Rev. B 89, 144425 Published 29 April 2014
 - [3] Thiele et al. *Voltage-controlled epitaxial strain in LaSrMnO₃ / PbMgNbO₃ - PbTiO₃ (001) films*. Appl. Phys. Lett. 87, 262502 (2005).
 - [4] Liu et al. *Spin-Torque Switching with the Giant Spin Hall Effect of Tantalum* Science 4 May 2012: Vol. 336 no. 6081 pp. 555-558

VI. APPENDIX

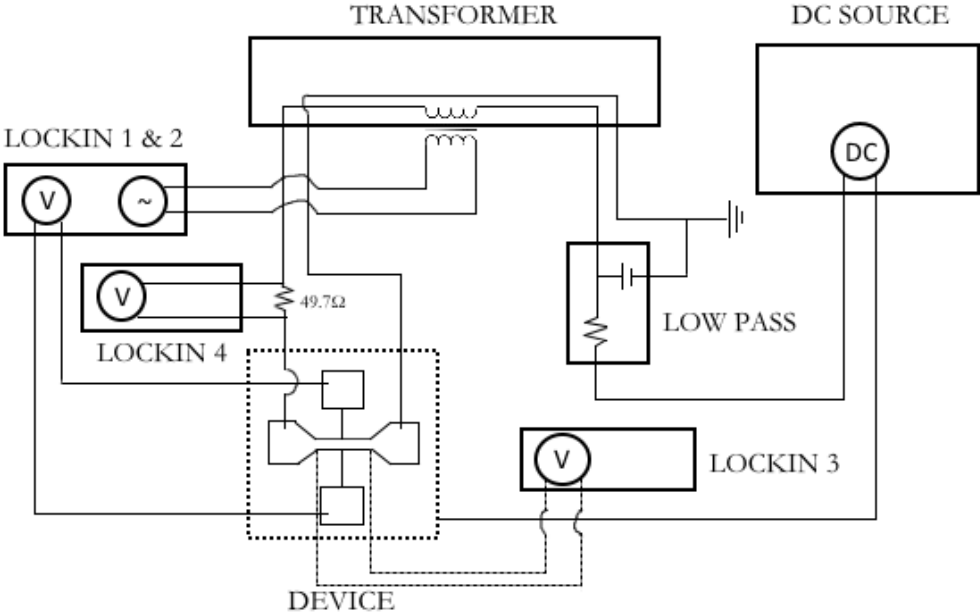


FIG. 11. Diagram for strain application while measuring SHR using the 2nd harmonic technique.

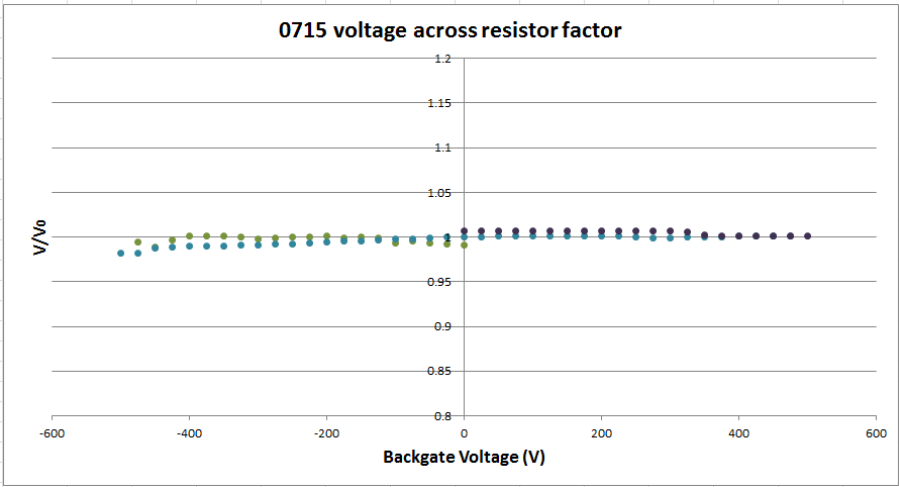


FIG. 12. Voltage drop across resistor during strain application in 2nd harmonic experiment. The y-axis is labeled with each point's ratio to the first data point.

Crack Propagation in Cancellous Bone

Nisha R. Gupta, Jonathan B. Matheny, Christopher J. Hernandez

Department of Mechanical and Aerospace Engineering, Cornell University, Ithaca, NY 14853

Abstract

While many toughening mechanisms have been extensively studied in cortical bone, fracture toughness and fatigue crack growth has not been well examined in cancellous bone, a cellular solid. Previous work in this lab has looked at crack growth in cancellous bone in relation to local stresses, which have no orientation. However, it is believed that tensile loading is important to crack initiation and propagation and thus, it is important to study the relationship between tensile stress and crack growth. Here we describe a method of determining the tensile stress of damage produced by cyclic loading of human vertebral cancellous bone. Using image processing scripts, the damage objects were flattened to calculate normal vectors along the surface. The normal vectors may be combined with finite element models to determine the tensile stress at each voxel in the damage object. By studying the relationship between tensile stress and fatigue crack growth, we can gain a better understanding of the fracture resistance mechanisms in cancellous bone.

I. Introduction

Bone is natural material with a unique set of properties that make it a good model for the design of high performance materials. Bone is lightweight yet it has excellent strength and stiffness¹. This favorable combination of properties is derived from the structure of bone, which consists of a porous foam interior, called cancellous bone, and a solid shell exterior, called cortical bone². In addition to its strength and stiffness, bone must have the toughness to resist fracture during cyclic loading; however, fatigue crack growth has only been extensively studied in cortical bone and not cancellous bone.

Many of the mechanical properties of bone come from its hierarchical structure. Bone has a mineral component, carbonated hydroxyapatite, and a polymer component, type-I collagen³. In cortical bone, the mineralized collagen fibrils are stacked together in lamellae, which are then wrapped in concentric circles to form osteons³. It has been shown that this microstructural hierarchy plays an important role in crack initiation and propagation⁴.

The creation of microcracks in bone is a fracture resistance mechanism³. Energy dissipation is achieved through two mechanisms: intrinsic toughening, which occurs ahead of the crack tip, and extrinsic toughening, which occurs behind the crack tip¹. Intrinsic toughening works to inhibit crack formation and promote ductility, while extrinsic toughening works to reduce local stresses and strains at the crack tip to prevent extension of the crack¹. In cortical bone, intrinsic toughening mechanisms are fibrillar sliding and molecular uncoiling of collagen, and extrinsic toughening mechanisms are crack deflection and crack bridging, which involve the mineralized boundaries of osteons¹.

Though these mechanisms have been well studied in cortical bone, little is known about crack growth in cancellous bone. While larger cracks dissipate more energy, crack extension can

lead to microfracture of discrete struts, called trabeculae, in cancellous bone⁵. Previous work in this lab has focused on measuring crack propagation in cancellous bone using local stresses determined from high-resolution finite element modeling. From the previous study, it was evident that there is a relationship between crack growth rate and stress intensity, but no relationship between crack growth rate and local stresses (Fig. 4 and 5). However, it has been suggested that the degree of crack extension is a result of the loading mode and that crack initiation and propagation may be influenced by mode-I (tensile) loading in cancellous bone⁵. Though it is difficult to measure tensile stress because it requires finding both the direction and magnitude of stress, it would be advantageous to study the relationship between crack growth rate and tensile stresses.

The overall goal of the current study is to investigate the mechanism of crack propagation in cancellous bone and its effect on mechanical properties. Here, we consider the effect of tensile stresses on the crack propagation of human vertebral cancellous bone during fatigue loading.

II. Methods

Specimen Collection and Mechanical Testing

Cylindrical specimens of cancellous bone from the fourth lumbar vertebral bodies of 11 human donors (4 males, 7 female, aged 62-88 years, tissue source NDRI) were collected and submitted to cyclic compression in two bouts of loading. The first bout of fatigue loading was stopped before failure, as detected by changes in the creep-fatigue curve (Fig. 1A), and the second bout of loading was applied until failure (5% apparent strain). Tissue damage was stained with xylenol orange fluorescent dye after the first bout of cyclic loading and again with calcein fluorescent dye after the second bout of loading (Fig. 1B).

Image Acquisition

Images of the specimens were collected using serial milling, an image acquisition approach that provides three-dimensional fluorescent images of the entire specimen (8 mm diameter, 4 mm in height) at a voxel size of 0.7 x 0.7 x 0.5 μ m. Propagating damage zones were identified as regions where the second stain was in direct contact with the first damage stain (Fig. 1B).

Finite Element Modeling

Linear elastic finite element models were created from micro-computed tomography images to analyze the stress distribution for each specimen (Fig. 2). Finite element models consisted of 31-98 million elements and were implemented on the Stampede Supercomputer Cluster (Texas Advanced Computer Center, TX,USA).

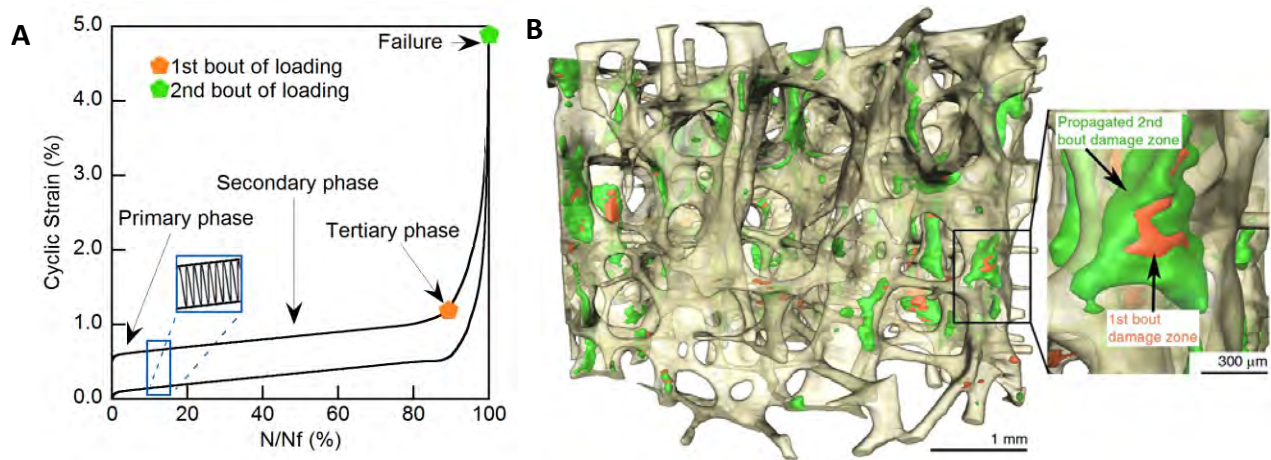


Figure 1. **A)** Creep-fatigue curve. First bout of cyclic compressive loading was applied to cancellous bone until the start of the tertiary phase and second bout of loading was applied until failure. **B)** Images acquired from serial milling after loading. The orange stain was applied after the first bout of loading and the green stain was applied after the second bout. Propagated damage was identified in the regions where the orange stain was in direct contact with the green stain.

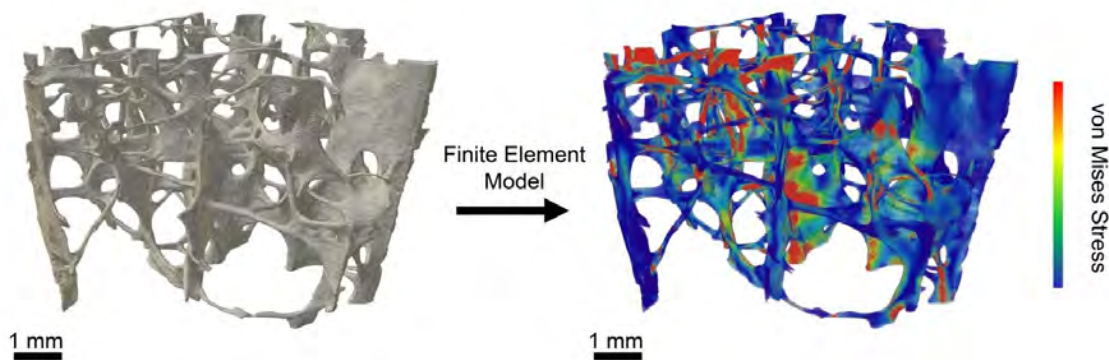


Figure 2. High resolution finite element models describing the distribution of tissue stresses in cancellous bone during cyclic compressive loading.

Image Processing and Analysis

Damage images were resampled to $2.8 \times 2.8 \times 2.5 \mu\text{m}$ to achieve approximately isotropic voxels and to reduce computational cost. Custom scripts were written for use with Matlab (R2010b (Version 7.11), Mathworks, Natick, MA, USA) and Amira (5.3 Visage Imaging, San Diego, CA, USA) to identify each individual damage object, flatten it to a thickness of approximately 1 voxel, and calculate the surface normal vectors at each voxel (Fig. 3). Due to the large size and high resolution of the damage images, damage objects had to be identified separately, and then cropped out of the original image stack into a new image stack. The image stacks of individual objects were then processed using a script that flattened the objects to their

centerline. The normal vectors were calculated at each vertex on the surface of the damage object. The surface normal vectors may be combined with finite element models to calculate the tensile stress for each damage object.

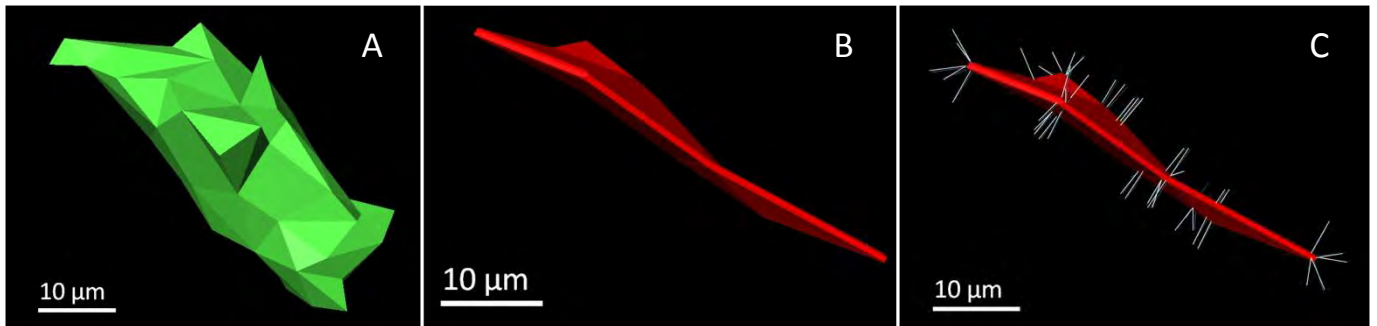


Figure 3. Images of a damage object **A**) before flattening and **B**) after flattening. **C**) Flattened images with surface normal vectors displayed.

III. Results and Discussion

Previous work in the lab consisted of using the local stress information provided by the high-resolution finite element models and the size of each damage object, growth rates (dc/dN) and local stress intensity range (ΔK) were determined (Fig. 4). While traditional fatigue crack growth involves multiple measurements of a single growing crack in a specimen, growth rate in the previous study was assessed once at each of the damage zones in each specimen. The observed crack propagation was similar to the small crack growth rates observed in cortical bone and was positively related to the stress intensity range (Fig. 4). However, there was no relationship between crack growth and von Mises stress (Fig. 5). This lack of a correlation to local stresses may be due to the fact that von Mises stress is a scalar value derived from principle stresses and does not consider the orientation of the stress.

A more accurate representation of the stresses contributing to crack growth may be found by combining the normal vector data with the finite element data. In order to find the normal vectors on the surface of each damage objects, the objects had to be flattened using image processing scripts. It was important to flatten the damage objects to their centerline because we assumed that the crack is opening in the midline of each 3D damage zone, thus we are finding the normal vectors of the surfaces created by crack opening, not the surfaces of the damage zones themselves. There were several challenges that occurred while writing the image processing scripts, such as the variation in shapes of damage objects and the large size of the image files (~1 GB). The complex shapes of the objects made it difficult to flatten them in a single dimension. To overcome this challenge, the thickness of the objects was measured at every region along the object and the objects were flattened in their thickest dimension along their centerline. To reduce the computational expense of processing the large image stacks, the damage objects were identified individually and separated into their own image stacks, which could be processed at the same resolution but required less memory.

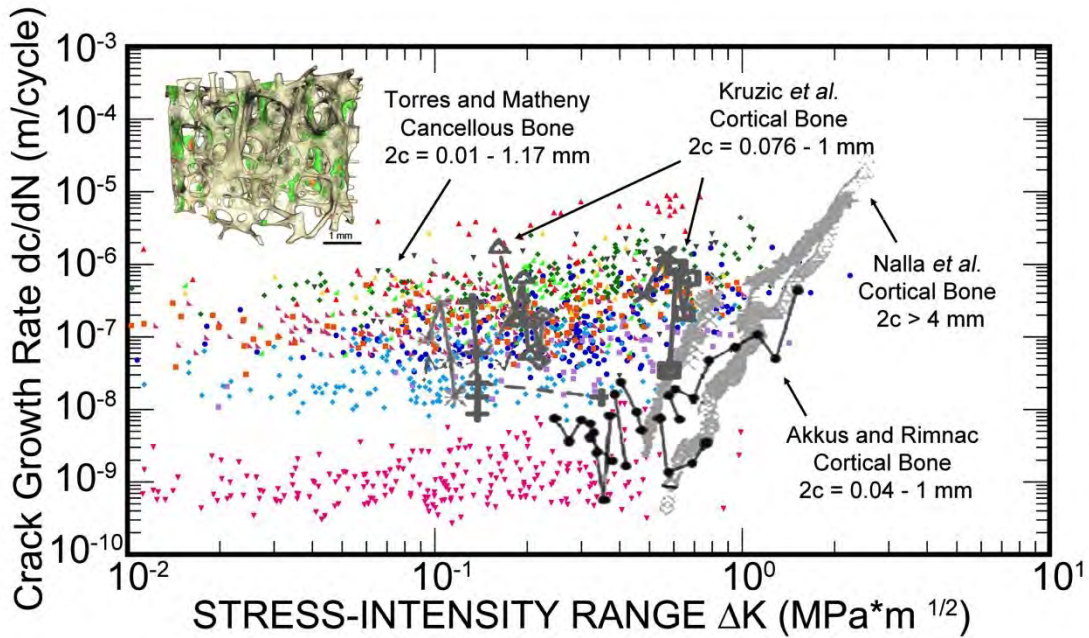


Figure 4. Fatigue crack growth measured in current study (Torres and Matheny, colored dots) compared to that measured in cortical bone (c =damage zone volume^{1/3})⁶.

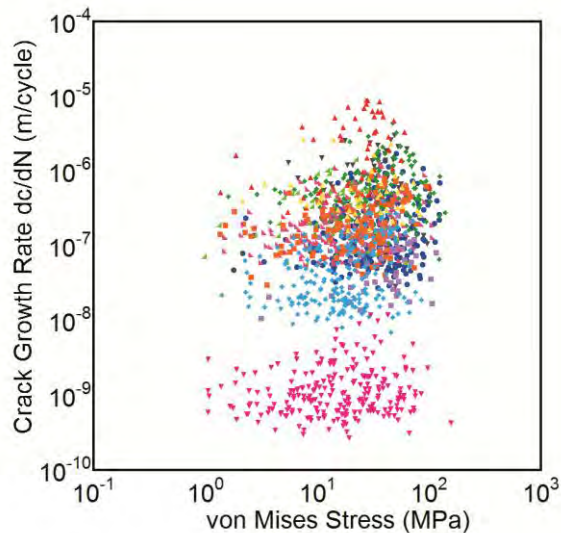


Figure 5. Crack growth rate does not correlate with local stresses.

With the scripts generated in this study to flatten damage objects and obtain their surface normal vectors, the tensile stress can be calculated at each voxel by mapping the normal vectors with finite element model. Using the tensile stress, a new stress intensity range can be calculated. Given that tensile loading is believed to contribute to crack extension in cancellous bone, we expect to see a greater correlation between crack growth and tensile stress than that seen with von Mises stress⁵. The limitations of the current method of analysis are that it assumes linear-elastic fracture mechanics and approximates crack length as the cube root of the volume of the damage zone. While the mineral component of bone satisfies linear-elastic fracture mechanics,

the collagen component introduces a source of plasticity that may need to be accounted for¹. However, the material appears to be undergoing brittle failure, as evidenced by the micro-cracking, as opposed to ductile failure so the linear-elastic approach is a fair assumption. Assuming linear elastic fracture mechanics and approximating crack length allows for a simple method of studying crack growth behavior in cancellous bone.

IV. Conclusion

In this study, we successfully devised an improved method of measuring the stress intensity range at individual cracks in human vertebral cancellous bone in order to better understand fatigue crack growth. Using scripts written to flatten damage object images and calculate their normal vectors, the tensile stress for each object can be determined and the effect of tensile loading on crack propagation can be studied more in depth. Studying fatigue crack growth in cancellous bone can provide new insight into the failure processes in cancellous bone and can also contribute to the design of high performance bioinspired materials.

V. Acknowledgements

This work was supported by the Cornell Center for Materials Research with funding from the Research Experience for Undergraduates program (DMR-1063059 and DMR-1120296) and by the National Institutes of Health and National Institute for Arthritis and Musculoskeletal and Skin Diseases (R01 AR057362).

VI. References

1. Wegst, U. G., Bai, H., Saiz, E., Tomsia, A. P., Ritchie, R. O. 2014. Bioinspired structural materials. *Nat. Mater.* 14, 23-36.
2. Meyers, M. A., McKittrick, J., Chen, P. Y. 2013. Structural biological materials: critical mechanics-materials connections. *Science* 339, 773-779.
3. Launey, M. E., Buehler, M. J., Ritchie, R. O. 2010. On the mechanistic origins of toughness in bone. *Annu. Rev. Mater. Res.* 40, 25—53.
4. Nalla, R. K., Kinney, J. H., Ritchie, R. O. 2003. Mechanistic fracture criteria for the failure of human cortical bone. *Nat. Mater.* 2, 164—168.
5. Lambers, F. M., Bouman, A. R., Tkachenko, E.V. Keaveny, T. M., Hernandez, C. J. 2014. The effects of tensile-compressive loading mode and microarchitecture on microdamage in human vertebral cancellous bone. *J. Biomech.* 47, 3605—3612.
6. Kruzic, J. J., Scott, J. A., Nalla, R. K., Ritchie, R. O. 2006. Propagation of surface fatigue cracks in human cortical bone. *J. Biomech.* 39 (5), 968—972.

Mechanical Characterization of Novel Bioink Derived from Decellularized Aortic Valves for 3D Bioprinting

Douglas Ivanoff¹, Dan Cheung², Bin Duan², Kate Schole², Jonathan Butcher²

¹ Department of Mechanical Engineering and Physics, The University of Tulsa, Tulsa, OK; ² Department of Biomedical Engineering, Cornell University, Ithaca, NY

Abstract

The development and implementation of 3D bioprinting as a viable tissue engineering technique allows for heterogeneity and accurate shape fidelity capable of being tailored to each patient. A hybrid hydrogel consisting of methacrylated hyaluronic acid/methacrylated gelatin was created with four conditions composed of varying concentrations of decellularized aortic leaflet or root (0, 1, 3, 6 mg/mL). Uniaxial compression test were run on each condition, and a model was applied to the non-linear data to extract modulus values. Rheological data suggests that cooling the hydrogels to 18 °C from room temperature increases the viscosity of the fluid without passing the crossover between the storage and loss modulus; thus, shape fidelity is expected to improve at 18 °C compared to room temperature. The shape fidelity of the bioink was assessed on an extrusion-based bioprinter by printing a 20 mm by 20 mm grid using Pluronic F127 and measuring the average area of the enclosed squares.

Introduction

Aortic heart valve disease is a severe condition affecting 1% of live births and 5 million adults per year in the United States.[1] The most common treatment is a surgical replacement with a prosthetic device: either a mechanical valve (MV) or bioprosthetic heart valve (BHV). While the replacement devices improve the condition of the patient and heart function, they have disadvantages compared to native valves. Patients with MVs require lifelong anticoagulation medication, whereas the BHVs' lifetime is shortened by mechanical fatigue of the leaflets.[2] Both of these options are especially limited in the pediatric treatment of heart disease due to their inability to grow and develop with the host. Another surgical option is replacement of the valve with a homograft, but this operation is severely limited by the supply of donors. Tissue engineered heart valves (TEHV) hope to provide a viable replacement option that allows for growth, host integration, and functionality similar to native valves.

Bioprinting is a common biofabrication technique due to its ability to replicate the complex structures of anatomical features. The three most utilized bioprinting techniques are inkjet-based, extrusion, and laser-assisted bioprinting.[3] A pneumatic extrusion bioprinter with three dispensing heads was used in this study. The advantage of extrusion-based bioprinting is the ability to print with high cell density and fabrication speed with a reasonable price. A solid material will not function with the extrusion method and a pure liquid will not retain shape after printing, so a viscous hydrogel is commonly used as the bioink. For bioprinting applications, hydrogels are limited by the material's cytotoxicity, viscosity, and ability to crosslink. Recent studies have used collagen, hyaluronic acid (HA), chitosan, and alginate as the bases for the hydrogels with several different cross-linking methods, including ionic polymerization and UV photopolymerization.[4] The aim of this study is to assess the mechanical properties of a hybrid hydrogel derived from aortic leaflet extracellular matrix (ECM) and identify its ideal conditions for extrusion bioprinting.

Experimental Section

Materials. Methacrylated hyaluronic acid (Me-HA) and methacrylated gelatin (Me-Gel) were created using a process described by Duan et al.[5] A control hydrogel was created by dissolving 2% w/v Me-Ha and 10% w/v Me-Gel DMEM/F12 cell culture medium including 0.05% Irgacure 2959. Four conditions were created from the control hydrogel. Four solutions were created with cell culture medium and decellularized aortic leaflet or root (dAL or dAR) with final concentrations of 0, 1, 3, and 6 mg/mL. Fabricated hydrogels were created with a volume mixture of 80% Me-Ha/Me-Gel combination and 20% of the dAL solution. Because the native tissue in the root wall of the heart valve is stiff than the native tissue in the leaflets, a material prepared with dAR would be expected to have a slightly higher modulus value than the same material prepared with dAL.

Testing. Uniaxial compression samples were created with round-disk silicon molds 8-mm in diameter and 1-mm in height. At least 8 samples for each concentration of the dAL hydrogel were extruded into the molds and exposed to 365 nm UV light for 5 minutes. The uniaxial compression test were performed on a TA-Instruments Q800 to 20% strain at room temperature (23 °C) with a ramp rate of 0.25 N/min. Analyzing the stress-strain data in terms of stress (σ) and applied stretch (λ), the model of a no-slip experiment on soft tissue was adopted from Roan et al.[6] and is shown in Equation 1.

$$\sigma = 2 \left(\lambda - \frac{1}{\lambda^2} \right) B_1 B_2 \text{Exp} \left[B_2 \left(\lambda^2 + \frac{2}{\lambda} - 3 \right) \right] \quad (1)$$

The variables B_1 and B_2 were found via a curve fit using the Mathematica 10 command “FindFit.” The product of the two variables is proportional to the modulus of the material.

Rheological experiments were also performed on each of the conditions using a TA-Instruments DHR3 rheometer using a 25 mm cone-plate with an angle of 2°. A flow temperature ramp was run from room temperature (23 °C) to 5 °C at a ramp rate of 2 °C per minute to measure the dynamic viscosity. In addition, an oscillatory temperature sweep was run from room temperature (23 °C) to 5 °C with a temperature step of 2 °C, strain of 1%, and shear rate of 1/s to find the crossing point of the storage and loss modulus. The varying temperatures were tested to determine the optimal conditions to extrude the hydrogel during bioprinting.

The shape fidelity of bioprinted structures is a key component to their ideal function. To test the shape fidelity of the Me-HA/Me-Gel hybrid bioink, the bioink was compared to Pluronic F-127, another bioink with exceptional shape fidelity and minimal swelling.[7] Figure 1 illustrates the shape fidelity test print with a 20-mm by 20-mm grid consisting of 16 squares (4-mm sides). The printer interprets the input as 10 straight-line paths. The overshoot on each side was included to ensure every square would be fully closed.

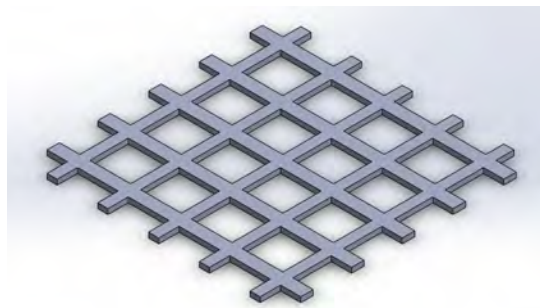


Figure 1: Shape fidelity grid consisting of 16 4-mm sided squares was created by intersecting 10 lines.

The area of each square is measured using images taken at 16x and the image analysis tool, ImageJ. Time limitations prohibited the printing of the Me-HA/Me-Gel bioink, while the Pluronic F-127 was printed and analyzed as a control test.

Results & Discussion

The average stress-strain curves from the uniaxial compression test are shown in Figure 2 for each condition. The behavior is nonlinear in the region of interest, thus Equation 1 was used to model the deformation. The model covers the strain range from 0% to 20%, because this is a common level of deformation in the valves inside the body. The curve fits matched the data sets accurately, so the models for each condition were averaged with a standard deviation calculated at every 1% to show the scatter and trend of each condition (seen in Figure 2). Figure 3 depicts the modulus for each condition. In order of increasing dAL concentration, the moduli of the hydrogels are 0.668 ± 0.266 kPa, 0.740 ± 0.166 kPa, 0.487 ± 0.091 kPa, and 0.490 ± 0.117 kPa. While the hydrogels with a higher concentration of the dAL appear to have a lower modulus, the standard deviation of the lower concentration hydrogels is much larger. There appears to be no significant difference between the modulus values all conditions. With a modulus below 1 kPa, the construct can be described as a soft material.

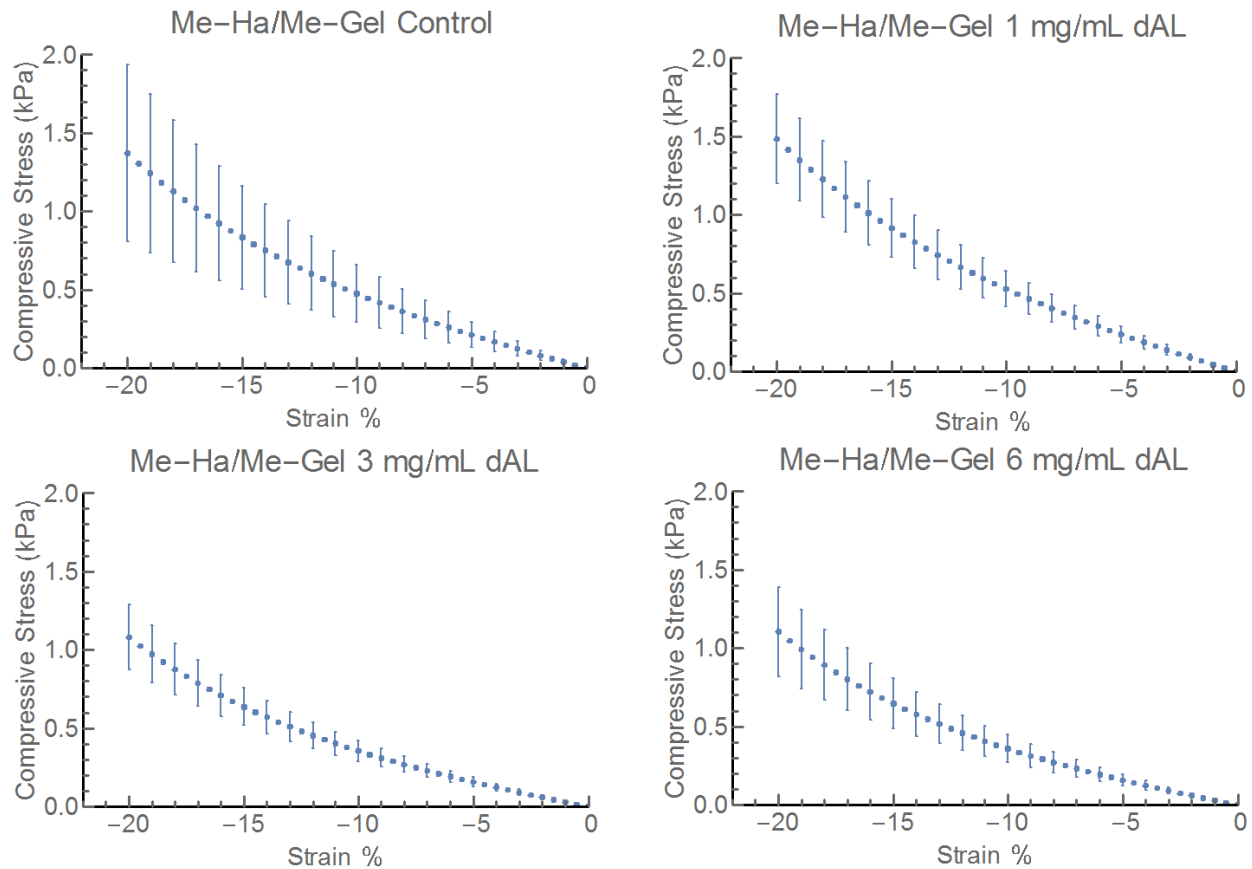


Figure 2: The stress-strain behavior of all four conditions of Me-HA/Me-Gel ($n = 8 - 13$)

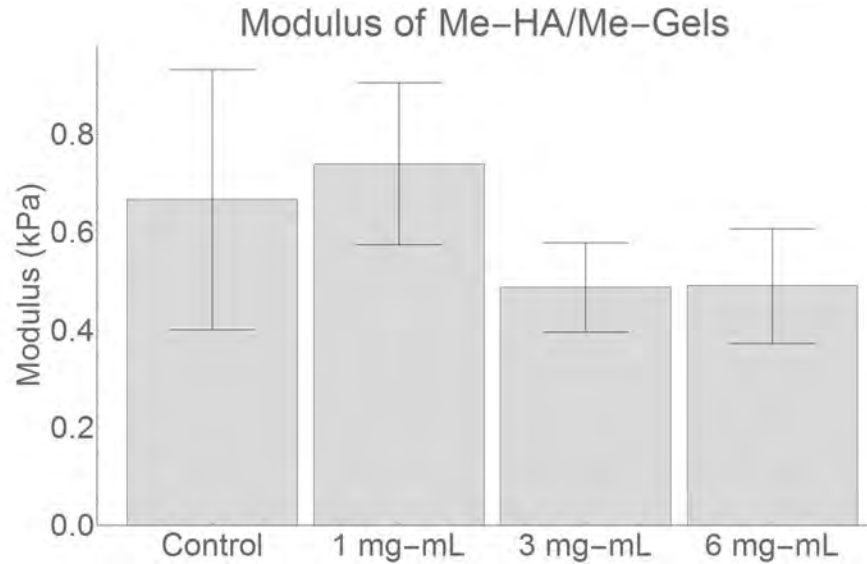


Figure 3: Modulus of each condition calculated from a curve fit of Equation 1 to the compression data.

The rheology of the hydrogel was investigated in order to identify ideal conditions during bioprinting. The rheometer test of a sample of the Me-HA/Me-Gel 6 mg-mL dAR is shown in Figure 4. The sample is representative of all the conditions, with viscosity increasing as temperature decreases and the crossing point between the storage and loss modulus located between 15 and 20 °C. With a noticeable viscosity increase below 20 °C, the rheological data suggest that chilling the hydrogel during the extrusion process might improve the ability of the hydrogel to retain shape; however, chilling the hydrogel below the crossing point of the loss and storage modulus would be detrimental to consistent extrusion due to the hydrogel displaying more solid-like properties. Simple extrusion of the material from a syringe at 4 °C produce thick, uneven lines.

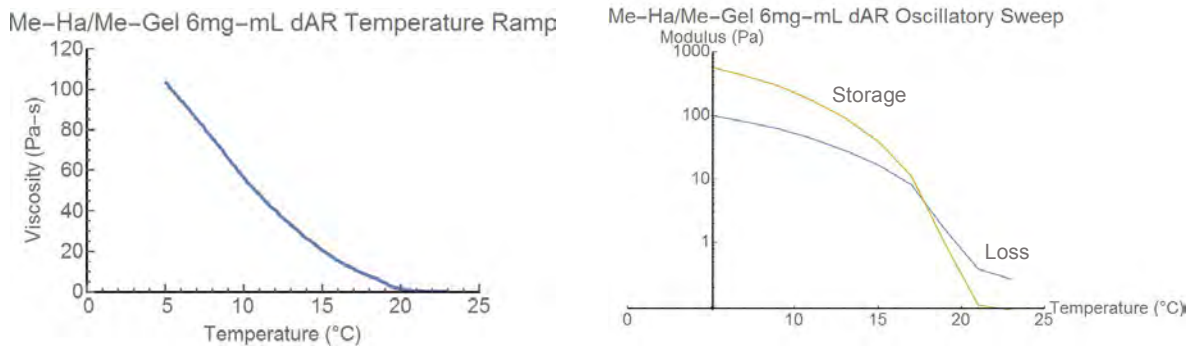


Figure 4: Rheometer testing for a Me-HA/Me-Gel 6 mg-mL dAR. A temperature ramp from room temperature to 4 °C (left) and an oscillatory temperature sweep from room temperature to 4 °C (right).

The grid of Figure 1 was printed at 18 psi with a 630 μm diameter tip using the Pluronic F-127, and each of the individual squares was imaged using a microscope at a fixed magnification of 25x. The contrast and brightness of the image were adjusted so that the image could be converted to a binary format to measure the square's area as seen in Figure 5.

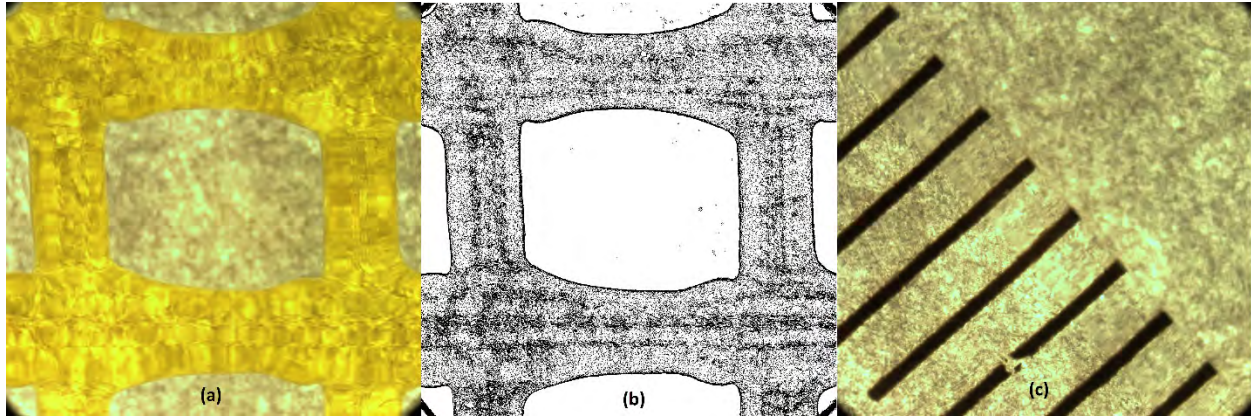


Figure 5: Images above are taken at 25x magnification. (a) A single square of Pluronic in the grid. (b) An analyzed image of the square to calculate enclosed area. (c) An image of a ruler with 1 mm spacing shown.

The average area of the squares was 7.99 mm^2 with a standard deviation of 0.96 mm^2 . Although the grid designed has 4 mm by 4 mm squares, an area of 16 mm^2 is not realistic due to the size of the extrusion tip and the design of the STL file. The pluronic print will serve as the control for future prints using the Me-HA/Me-Gel hydrogels.

Conclusions & Future Work

This study identifies the modulus of four conditions of a Me-HA/Me-Gel with varying concentrations of dAL. While the modulus values are lower than expected, several material concentrations could be altered to increase the modulus such as increasing the Irgacure concentration to 0.1% or increasing the w/v% of Me-HA to 4%. The rheological properties of the hydrogel demonstrated that shape fidelity of prints could be improved by cooling the material near $18 \text{ }^\circ\text{C}$ during the printing process. However, care must be taken not to reduce temperature too much as the material will begin to mimic solid property behavior. Future work will include bioprinting with each condition hydrogel at room temperature and $18 \text{ }^\circ\text{C}$, while comparing shape fidelity to that of the pluronic grid. After verifying for shape fidelity, a simple heterogeneous model valve structure with encapsulated cells will be printed using the hybrid hydrogels containing dAL and dAR for the leaflets and root, respectively. The structure will be conditioned in a bioreactor to assess the long-term viability and remodeling potential of the valve.

Acknowledgments

This work was supported by the Cornell Center for Materials Research with funding from the Research Experience for Undergraduates program (DMR-1063059 and DMR-1120296).

References

- [1] A. S. Go, D. Mozaffarian, V. L. Roger, E. J. Benjamin, J. D. Berry, W. B. Borden, D. M. Bravata, S. Dai, E. S. Ford, C. S. Fox, S. Franco, H. J. Fullerton, C. Gillespie, S. M. Hailpern, J. A. Heit, V. J. Howard, M. D. Huffman, B. M. Kissela, S. J. Kittner, D. T. Lackland, J. H. Lichtman, L. D. Lisabeth, D. Magid, G. M. Marcus, A. Marelli, D. B. Matchar, D. K. McGuire, E. R. Mohler, C. S. Moy, M. E. Mussolino, G. Nichol, N. P. Paynter, P. J. Schreiner, P. D. Sorlie, J. Stein, T. N. Turan, S. S. Virani, N. D. Wong, D. Woo, M. B. Turner, and American Heart Association Statistics Committee and Stroke Statistics Subcommittee, "Heart disease and stroke statistics--2013 update: a report from the American Heart Association," *Circulation*, vol. 127, no. 1, pp. e6–e245, Jan. 2013.
- [2] M. S. Sacks, F. J. Schoen, and J. E. Mayer, "Bioengineering Challenges for Heart Valve Tissue Engineering," *Annu. Rev. Biomed. Eng.*, vol. 11, no. 1, pp. 289–313, 2009.

- [3] S. Knowlton, S. Onal, C. H. Yu, J. J. Zhao, and S. Tasoglu, "Bioprinting for cancer research," *Trends Biotechnol.*
- [4] K. Markstedt, A. Mantas, I. Tournier, H. Martínez Ávila, D. Hägg, and P. Gatenholm, "3D Bioprinting Human Chondrocytes with Nanocellulose–Alginate Bioink for Cartilage Tissue Engineering Applications," *Biomacromolecules*, vol. 16, no. 5, pp. 1489–1496, May 2015.
- [5] B. Duan, E. Kapetanovic, L. A. Hockaday, and J. T. Butcher, "Three-dimensional printed trileaflet valve conduits using biological hydrogels and human valve interstitial cells," *Acta Biomater.*, vol. 10, no. 5, pp. 1836–1846, May 2014.
- [6] E. Roan and K. Vemaganti, "The nonlinear material properties of liver tissue determined from no-slip uniaxial compression experiments," *J. Biomech. Eng.*, vol. 129, no. 3, pp. 450–456, Jun. 2007.
- [7] D. B. Kolesky, R. L. Truby, A. S. Gladman, T. A. Busbee, K. A. Homan, and J. A. Lewis, "3D Bioprinting of Vascularized, Heterogeneous Cell-Laden Tissue Constructs," *Adv. Mater.*, vol. 26, no. 19, pp. 3124–3130, May 2014.

Growth of Monolayer Transition Metal Dichalcogenides by Metal-Organic Chemical Vapor Deposition

Alan Kaplan¹, Saien Xie², Jiwoong Park^{3,4}

¹Department of Materials Science and Engineering, University of Maryland, College Park, MD; ²School of Applied and Engineering Physics, Cornell University, Ithaca, NY; ³Department of Chemistry and Chemical Biology, Cornell University, Ithaca, NY; ⁴Kavli Institute at Cornell for Nanoscale Science, Ithaca, NY

Abstract

Transition metal dichalcogenides (TMDs) are layered structures similar to graphite, and can exist in a single layer form, like graphene. What differentiates monolayer TMDs from graphene is that they are direct band gap semiconducting materials, and exhibit relatively high electron mobility. Because of this, monolayer TMDs can have a huge impact on current electronics, as long as they can be fabricated in large scale. In order to do this, we have been growing monolayer TMDs by metal-organic chemical vapor deposition (MOCVD). We have been successful in growing different TMD uniform monolayers on the scale of one inch.

I. Introduction

In modern electronics, size is key. The smaller a device can be, the better. To further reduce the size of electronics, smaller transistors are required, and thin film semiconductors would be ideal for this purpose. Transition metal dichalcogenides (TMDs) are semiconducting materials which can be isolated into just one, three-atom thick layer, because of their unique crystal structure. The bulk form of these materials is made up of individual atomically thin layers that are held together by weak van der Waals forces, which allows us to separate just one layer for use in transistors¹. Figure 1 shows a model of one layer of MoS₂. In addition to reducing the size of electronics, monolayer TMDs are prime candidates for use in flexible electronics² or valleytronics³, and exhibit interesting properties such as piezoelectricity⁴ and direct band gaps⁵.

There are several methods of isolating monolayer TMDs, of which exfoliation is the most simple. Exfoliation is peeling a few layers from the bulk material and looking through the pieces to find small areas of monolayer material. The small pieces are great for making

a few devices, but the process cannot be used for large scale production. To make large amounts of electronics from TMDs, chemical vapor deposition is better suited for the job because it is the most versatile, controllable, and scalable method currently available⁶. Over the past ten weeks, we used metal-organic chemical vapor deposition (MOCVD) to make the most uniform and continuous monolayer possible of molybdenum disulfide (MoS₂), tungsten disulfide (WS₂), molybdenum diselenide (MoSe₂), and tungsten diselenide (WSe₂).

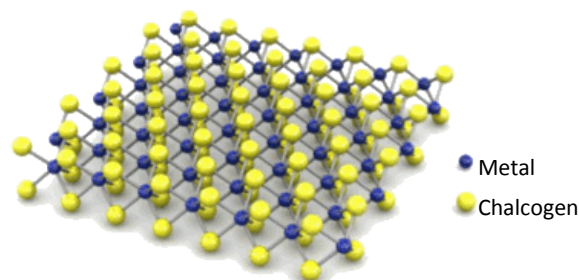


Figure 1 | Model of single layer TMD
(Adapted from ref. 7)

II. Setup

To perform the MOCVD growth, a tube furnace was used with the setup as seen in Figure 2. In order for the flow rate of the solid precursors, $\text{Mo}(\text{CO})_6$ and $\text{W}(\text{CO})_6$, to be stable, heating tape is wrapped around the cylinders to increase the vapor pressure of the precursors so they can sublime more easily. The flow of the precursors into the system is precisely regulated by the mass flow controllers (MFC) down to 0.1 standard cubic centimeter per minute (sccm). Additionally, sodium chloride is placed inside the quartz tube upstream of the samples to increase the grain size and uniformity of the growth.

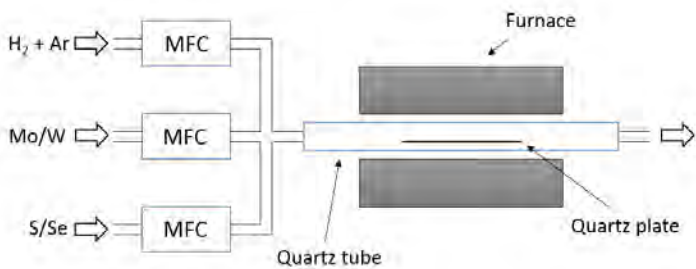


Figure 2 | Schematic of the furnace setup. Transition metal and chalcogen precursors are flown into the quartz tube with the carrier gas, Ar, and deposited along the SiO_2/Si substrate, located on the quartz plate. The byproducts are flown out of the tube by a vacuum pump.

III. Growth

Since the goal of the growth is to make materials for electronic or optical purposes on a large scale, the product of the MOCVD needs to be uniform and continuous. The success of the growth depends on many factors: appropriate precursors, temperature, flow rate of the carrier gas, and H_2 flow. First of all, the choice of precursors is extremely important since the metal precursor needs to completely decompose at a temperature that can be reached by the furnace, and needs to be volatile enough to become a gas at low enough temperatures to be flown into the system. The chalcogen precursor also needs to be volatile, however, barely needs to decompose for a successful

growth⁶. Additionally, getting the furnace to the right temperature is critical because it needs to be hot enough for all of the precursors to decompose, otherwise the material we want will not be deposited. For the goal of uniformity, the carrier gas, argon, flow rate is especially important since it delivers and uniformly spreads the metal precursor into the hot zone of the furnace. Finally, flow of H_2 is important because it helps to remove from the system the carbon species that decompose from the organic precursors.

IV. Characterization

Once the samples are grown, there are a variety of tools to help us check the uniformity and also characterize the sample as a monolayer. If the sample has large grains, then the pattern will be visible on an optical microscope, as seen in Figure 3a. From this image, we can diagnose the uniformity and continuity of the sample. Additionally, the continuity and uniformity can be examined on a much smaller scale using the scanning electron microscope (SEM).

In addition to the optical microscope and SEM, we can characterize if the material is a monolayer and verify which material was grown using Raman spectroscopy and photoluminescence tests. Each TMD has a unique Raman spectrum, so we can verify the composition of the growth, and we can also determine if the material is a monolayer from the spectra. The definitive test for monolayers is the photoluminescence test. Since multiple layers of TMDs have indirect band gaps, and single layers of many have direct band gaps, the photoluminescence test is able to distinguish monolayers by putting the sample under a laser. Since they have a direct band gap, only the monolayer areas will emit light when excited by the laser. Also, since each TMD has a different band gap, the material can be identified by the emitted photon energy.

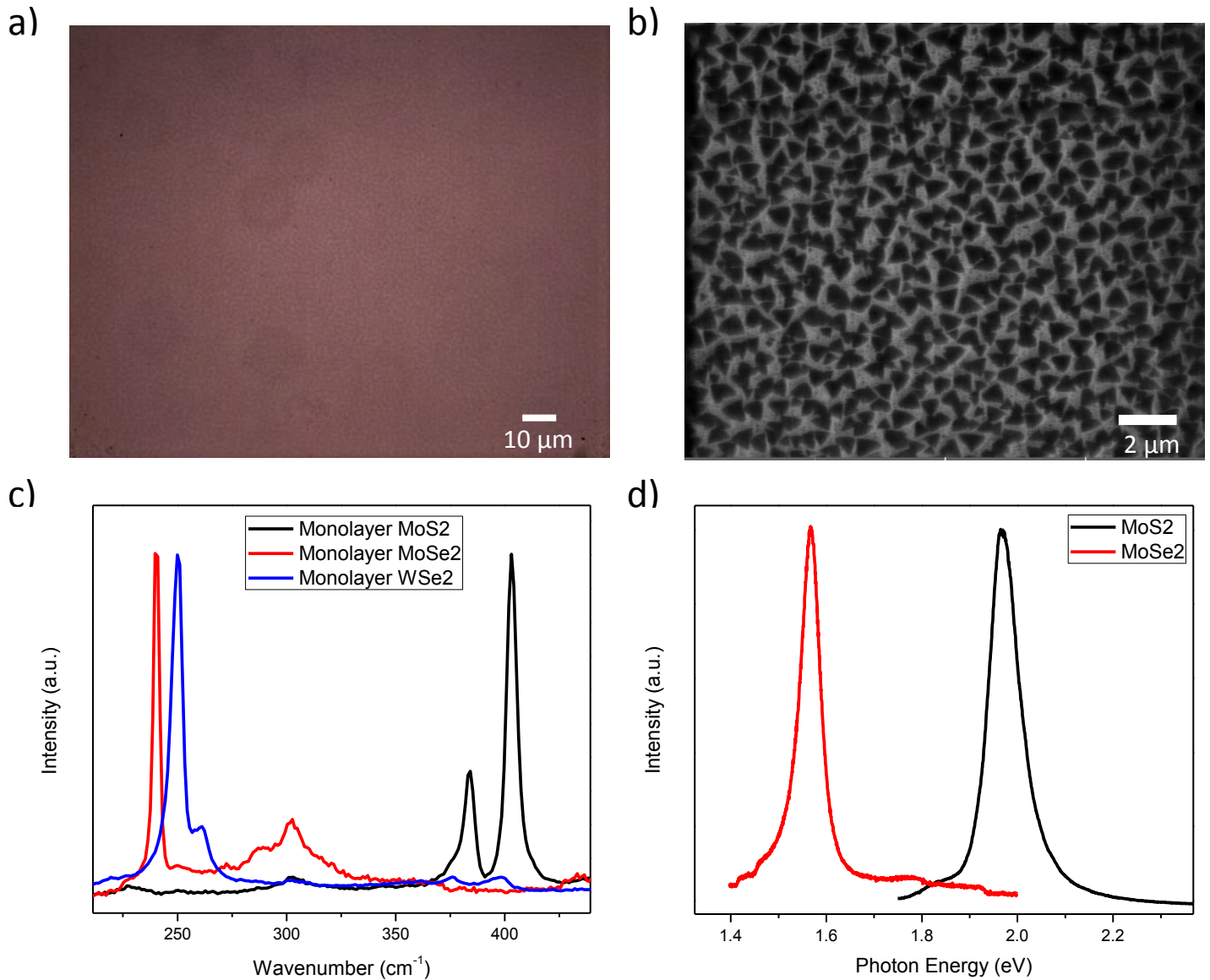


Figure 3 | Characterization of monolayer TMDs. **a)** Optical microscope image of monolayer MoS₂ growth. **b)** SEM image of the same monolayer MoS₂ growth. **c)** Normalized Raman spectra of MoS₂, MoSe₂, and WSe₂. **d)** Normalized photoluminescence spectra of MoS₂ and MoSe₂.

V. Conclusion

So far, we have grown four TMDs, MoS₂, WS₂, MoSe₂, and WSe₂, all of which have been studied before using other methods to isolate monolayers. Because of the versatility of MOCVD, in the future, this furnace will be used to grow monolayers of many more TMD materials. Hopefully, this will unveil interesting and useful properties that could possibly

revolutionize the world of electronics. Moving forward, the molybdenum and tungsten sources will be switched out for chromium, tantalum, and titanium, and as for the chalcogen sources, tellurium will also be introduced. The MOCVD setup allows for unmatched control of the growth, and if controlled combinations of metals are introduced, will allow for the tuning of properties to create the ideal material.

VI. Acknowledgements

I would like to thank the entire Park group for welcoming me so well this summer, and especially Saien Xie for being an awesome mentor. This work was supported by the Cornell Center for Materials Research with funding from the Research Experience for Undergraduates program (DMR-1063059 and DMR-1120296).

VII. References

- ¹ Kaasbjerg, K., Thygesen, K. S. & Jacobsen, K. W. Phonon-limited mobility in n-type single-layer MoS₂ from first principles. *Phys. Rev. B* **85**, 115317 (2012).
- ² Rogers, J. A., Someya, T. & Huang, Y. Materials and mechanics for stretchable electronics. *Science* **327**, 1603–1607 (2010).
- ³ Mak, K. F., McGill, K. L., Park, J. & McEuen, P. L. The valley Hall effect in MoS₂ transistors. *Science* **344**, 1489–1492 (2014).
- ⁴ Wu, W. et al. Piezoelectricity of single-atomic-layer MoS₂ for energy conversion and piezotronics. *Nature* **514**, 470–474 (2014).
- ⁵ Mak, K. F., Lee, C., Hone, J., Shan, J. & Heinz, T. F. Atomically thin MoS₂: a new direct gap semiconductor. *Phys. Rev. Lett.* **105**, 136805 (2010)
- ⁶ Kang, K. et al. High-mobility three-atom-thick semiconducting films with wafer-scale homogeneity. *Nature* **520**, 656–660 (2015).
- ⁷ Benameur, M.M., Radisavljevic, B., Sahoo, S., Berger, H. & Kis A. Visibility of dichalcogenide nanolayers. *Nanotechnology* **22**, 125706 (2011)

Large Scale Separation of Colloidal Nanoparticles

William Kellogg¹, Douglas Nevers², Tobias Hanrath²

¹Department of Chemical and Biological Engineering, SUNY Buffalo, Buffalo, NY

²Department of Chemical and Biomolecular Engineering, Cornell University, Ithaca, NY

Nanoparticles are a major focus of research and interest for both public and private interests due to their broad range of applications. The commercialization of nanoparticles is currently limited by modern separation techniques as traditional methods are not continuous processes and they could not operate at a realistic scale and cost for commercial uses. Our work focuses on the use of a novel separation technique, electrophoretic deposition, to achieve high yield and high quality separation of copper sulfide nanoparticles. We ultimately develop a two-step procedure, which can separate nanoparticles from solution in a reproducible manner, and scanning electron microscopy confirms that our deposited particles are in fact copper sulfide without any unreacted precursors or solvent.

Introduction

In recent years, nanoparticles show great promise for a wide variety of applications, from drug carriers to data storage media, expanding the demand for their commercial production. While many synthesis routes exist for nanoparticles scale-up and production the scalability of post-synthesis separation methods are not typically addressed nor commercially feasible. Conventional separation techniques, such as centrifugation or chromatography, face major hurdles since they are batch processes by nature, and they cannot efficiently handle kilogram scale quantities of material [1]. Electrophoretic deposition offers an innovative alternative to conventional methods because it can process large amounts of material, and it can achieve separation in a continuous setup [2].

Electrophoretic deposition utilizes the separation of charged objects via the

application of a uniform electric field, i.e. electrophoresis; this causes these objects to migrate toward and ultimately deposit upon the electrode of opposite charge. The shape and size of particles will impact both their speed and degree of separation. This technique first saw much use in the biological and biochemical fields as a method for protein separation, but recently many researchers have adapted it for nanoscale applications [1]. Specifically, Lhuiller achieved a greater than 95% yield via absorbance of his redeposited material in his batch separation of two-dimensional Cadmium Selenide (CdSe) nanoplatelets (40nm x 10nm) from 3 nm CdSe quantum dots [3]. Additionally, Kim was able to reach a yield of 61% for a continuous flow separation of CdSe nanoparticles [2].

Our work focuses on the batch separation of Copper Sulfide (Cu_{2-x}S) due to its reduced cost compared to CdSe

nanoparticles. We aim to develop the optimal separation conditions in terms of voltage, solvent ratio, electrode spacing, and aging effects to maximize yield while maintaining particle quality. After we find the optimal conditions for Cu_{2-x}S separation, these results will serve as a framework to expand our work to separation of other types of nanoparticles.

Methods and Materials

Figure 1 below provides a simple illustration of how electrophoresis works and the principles that govern it.

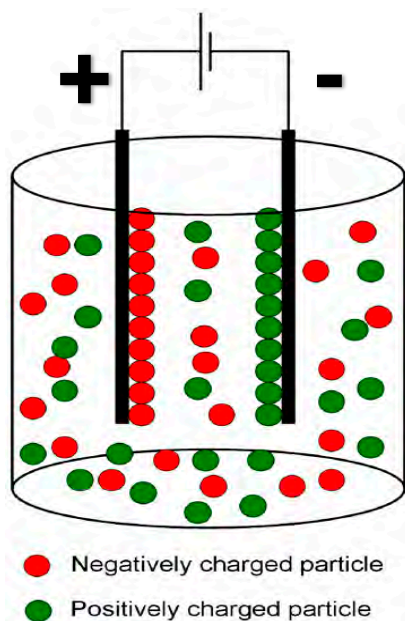


Figure 1. Schematic of Electrophoretic Deposition [4]

This first step for our procedure involved the creation of a nanoparticle stock solution. For the initial experiments, a vial of refined nanoparticles was obtained and then used to create 5.0 mg/mL solutions of refined nanoparticles in hexane. The refined solutions of nanoparticles had already undergone centrifugation. We would then transfer the required amount of solution (1-2 mL) into a beaker via a syringe and add hexane and/or acetone to achieve the desired conditions.

For the raw solution experiments, a vial of post-synthesis slurry was obtained directly from the reaction. This slurry contained the desired nanoparticles, unreacted precursors, unused surface ligands, and solvent. We then prepared desired stock solutions of unpurified nanoparticles in acetone, ethanol or hexane in a 1:10 ratio of nanoparticle to solvent by mass.

We experienced difficulty obtaining consistent results from our raw solution separations using our initial procedure. The yield varied from approximately 50% in one solution to less than 10% in other solutions. Additionally, the deposition both changed color and shifted from the positive to the negative plates. We theorized the presence of unreacted precursor and salts in the raw solution were interfering with the solution quality, so we decided to shift to a new two-step procedure. This procedure started by suspending nanoparticles in oleylamine instead of hexane. The oleylamine served to filter out the unreacted precursor since the chlorides within the precursor would bind to the amine group of the oleylamine solvent. We performed several runs of EPD on the same solution to fully extract the nanoparticles, and after each run we would mass the plates and then wash the film into a beaker using hexane. The beaker was labeled in 10 mL increments, so by the end of the first step we would know the total collected mass and volume of hexane in solution, and could obtain an approximate value of concentration. This solution was then used for the second step of the procedure, which involved EPD in hexane or acetone similar to the refined solution experiments. The process was complete when deposition no longer occurred and the remaining solution resembled the supernatant from the

centrifugation separation of raw nanoparticle solutions.

In our system, the electrodes themselves were made of stainless steel (2 cm by 5 cm). They were attached to glass slides to hold the electrodes in place. Additionally, smaller glass slides were used as spacers to control the electrode spacing. Metal plates (either 1 cm copper disks or 2 cm by 2.5 cm stainless steel plates) were weighed and then attached to the electrodes using double-sided tape. The distance between the positive and negative plates was measured using a dial caliper. Then, a clamp was attached to the smaller glass slide, and the plates were dipped into solution and placed as close to the bottom of the beaker as possible. Alligator clips were used to attach the positive and negative terminals of the power supply to each electrode. For consistency, the same electrodes were used as the positive and negative electrode for every test. The power supply is then set to the appropriate voltage, typically 800V, and the experiment will run for the requisite time, typically thirty minutes. When finished, tweezers were used to remove the plates from the electrodes and place them on a scale for weighing. Finally, both the plates and electrodes were cleaned using hexane.

Results

Our refined solution experiments showed that electrode spacing between 0.5 cm and 1.5 cm did not impact nanoparticle deposition (figure 2) and that increasing the acetone concentration of the solution 0 to 50% nearly tripled the deposition (figure 3) Figure 4 illustrates the deposition pattern that was observed. Figure 5 shows the inconsistent results of the initial raw solution tests in terms of average yield. Average yield numbers were obtained by performing several EPD

tests on solutions of nanoparticles prepared from the same batch of post synthesis slurry. We would find the total mass deposited on the plates for this solution and compare this to the mass input into that solution to determine the yield for that particular solution. Once the yield numbers were calculated for each solution, they would be averaged out to find the average percent yield for the solutions prepared from that batch of nanoparticles. ; figure 6 shows the improved consistency of the new procedure and figure 7 shows the impact of voltage in the new procedure. Figure 8 illustrates that 92% of the mass is lost for the raw solution prior to any EPD as it is raised from 0 to 600 ° C. Figure 9 is an SEM image displaying the copper sulfide nanoparticles deposited on a copper plate substrate, and figure 10 is a composition analysis confirming the presence of copper and sulfur in these nanoparticles. The size of the copper peak and the presence of aluminum and germanium are likely from the copper plate and not the nanoparticles themselves.

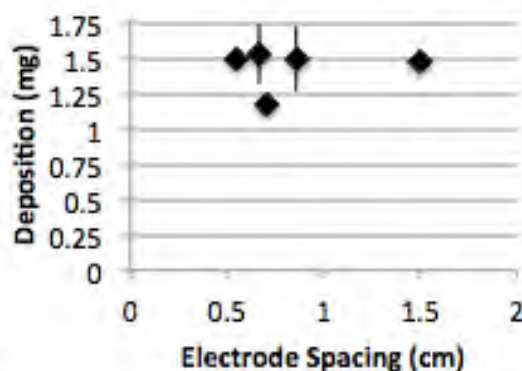


Figure 2 Deposition graphs charting deposited material versus electrode spacing for the refined solution

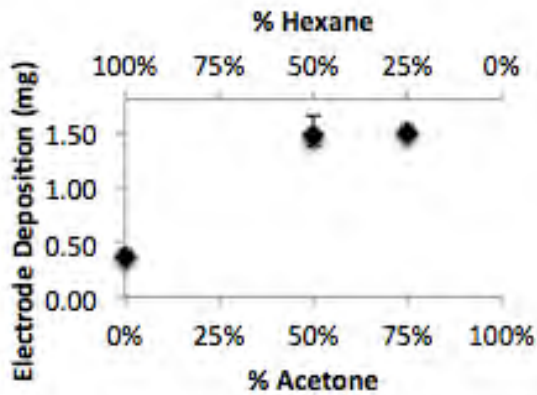


Figure 3 Deposition graphs charting deposited material versus the acetone ratio by volume within the solvent for the refined solution experiments. Experiments were performed at 0% Acetone (100% Hexane), 50% Acetone and 75% Acetone.



Figure 4 Image of refined solution deposition pattern on copper plates, nanoparticles deposit exclusively on the negative electrode

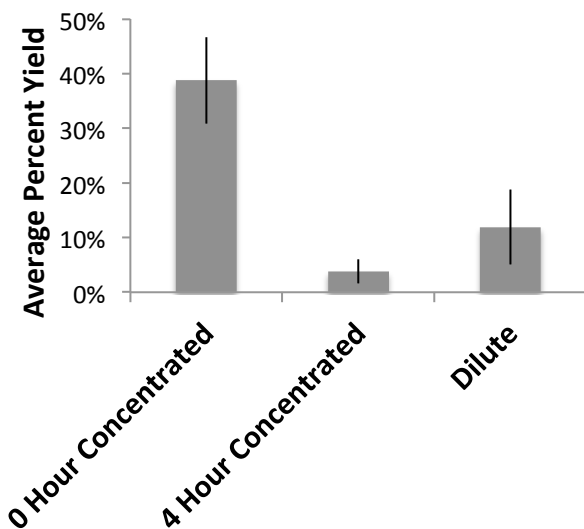


Figure 5 Average percent yield of various raw solutions

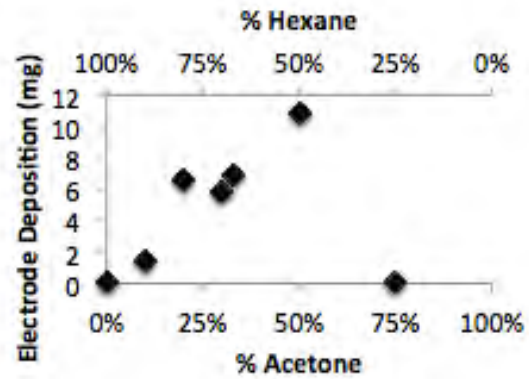


Figure 6 Electrode Deposition at varied acetone concentration for the redesigned raw procedure

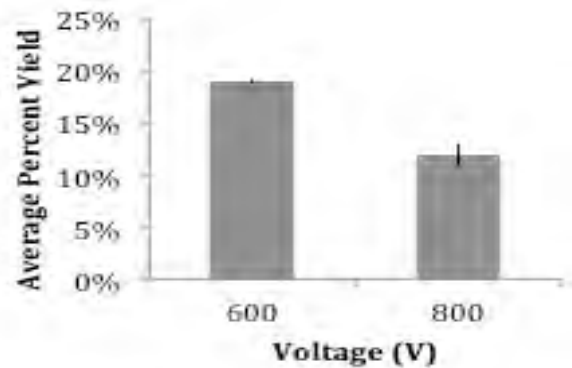


Figure 7 Effect of voltage on the average percent yield for the improved raw procedure

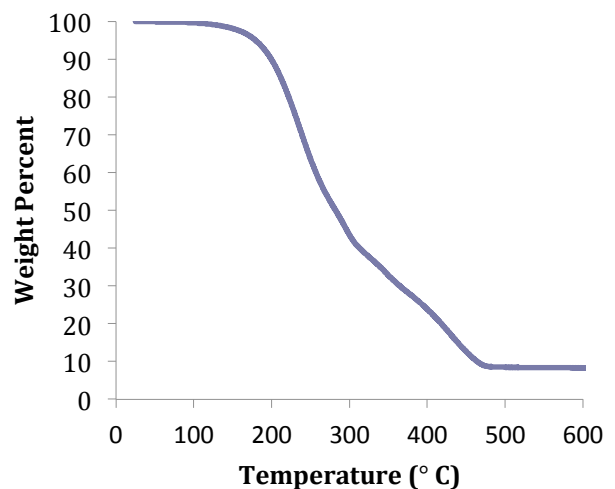


Figure 8 TGA data showing the mass loss of the raw solution prior to any EPD as it is heated from 0 to 600° C

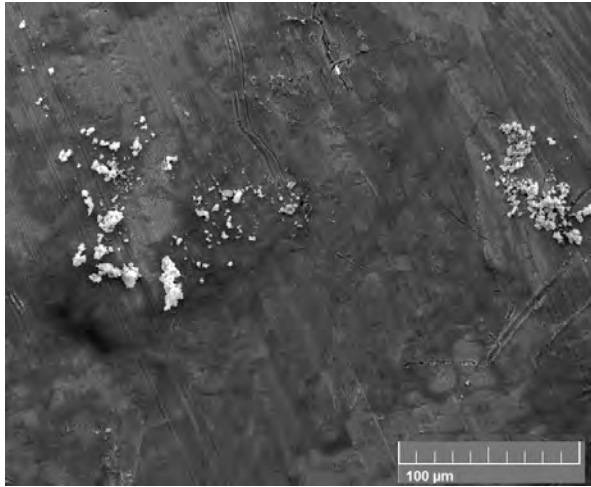


Figure 9a SEM image of post phase 2 copper sulfide nanoparticles deposited on copper plate substrate

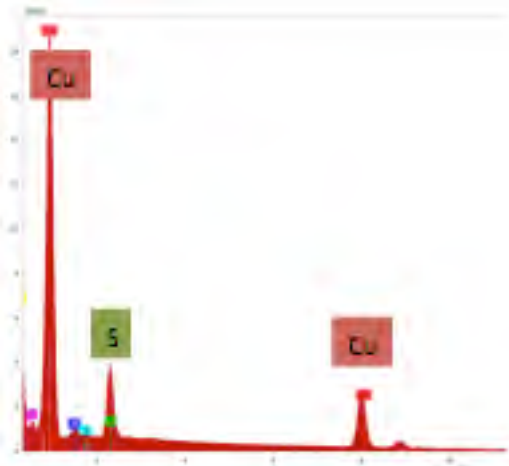


Figure 9b Composition analysis of the copper sulfide nanoparticles highlighting the copper and sulfur peaks

Discussion

Our refined solutions results largely paralleled our expectations from theory, and we believe we can explain the few surprises in the data. Figure 4 was the first check, and the exclusively negative deposition pattern matched expectation because the positive zeta potential of the

copper sulfide nanoparticles should lead to deposition on the negative plates. Figure 3 also corresponded with our expected values. We tested at 0% Acetone, and 75% acetone, because these were approximately the high and low acetone content values we found in literature [2]. We also tested at 50% since this was another very common ratio; specifically this is the solvent ratio that Lhuiler et al. used for his selectivity experiments. [3]. These results demonstrated that increased acetone concentration yielded higher deposition amounts, which makes sense since it increases the overall dielectric constant of the solution [5]. The dielectric constant assesses how easily an applied electric field can polarize a solution with higher dielectric constants being more polarizable. Therefore, the solutions with higher dielectric constants allow for increased particle mobility and it logically follows that it would lead to more deposition. There is little difference between the results at 50 and 75% acetone since they both achieved full separation and turned the solution clear. The total deposition of particles was verified via absorbance measurements. Figure 2 slightly surprised us since the electrode spacing showed little impact on the amount deposited while the electric field falls off at a factor of $1/\text{radius}^2$ [6], but we believe this is because the deposition was complete for each system by the specified time; though it may have been faster at shorter spacing. The color change of the solution from brown to clear signified all the nanoparticles were removed from solution, and this was also verified by absorbance measurements that suggest the yield of particles is at or near 100%. This showed that for the refined solution at the optimal solvent

ratio, electrode spacing was not statistically significant.

The movement from refined to raw solution experiments drastically increased the complexity since the refined solution had undergone at least one, and usually two, rounds of centrifugation making it much easier to deposit. Conversely, the raw solution is used directly from synthesis, so it still contains unreacted precursors and excess ligands along with the desired nanoparticles. Figure 5 shows the different results we obtained between experiments run with concentrated and dilute solution. The raw, concentrated solutions were made under nearly identical synthesis conditions, so they should have resulted in very similar deposition patterns and amounts. The only difference was that the slurry for raw concentrated A was obtained at the 0 hour mark from the top of the concentration ramp while raw B was obtained at the 4 hour mark. We did not believe this would significantly impact yield since they are at the same concentration. However, as shown in Figure 4, the raw A concentrated solution resulted in deposition amounts an order of magnitude larger than those of the raw B concentrated solution.

We again attributed this to impacts from the unreacted precursor affecting the solution quality, and we also discussed the B solution may be less stable and degraded much more rapidly than the A solution. We next developed our new procedure discussed earlier to improve the consistency of our separations. Our traditional procedure was a one step process where we immediately placed the raw particles into hexane, and we realized that our successful refined solutions were two-step procedures that included a degree of separation (centrifugation) before

suspension in hexane. To model the initial separation, we began running our first phase of the procedure in oleylamine because the amine would attract the salts and keep them in solution while the nanoparticles should migrate to the electrode. Furthermore, oleylamine was a logical choice because it is the ligand on our Cu_{2-x}S nanoparticles. We hypothesized this first step would increase the purity of our second phase of separation, and lead to improved results.

As shown in figure 7, the new procedure improved the precision and repeatability of our results, but it resulted in a rather low yield value. The yield value only reached 18%, and we attribute the low yield from the second phase to a lack of optimization since we have not yet found ideal separation conditions in terms of voltage, electrode spacing, and solvent ratio for phase 2. The figure demonstrates that the simple change from 600V to 800V can improve yield by 6%. We theorize this result may occur due to degradation of the particles at higher applied potentials. Additionally, figure 6 shows a similar trend of solvent ratio as seen for the refined solution in figure 3. However, a drop off occurs above 50% for the raw solution procedure; the solution began to bubble during these tests, suggesting that the solution was too conductive at these acetone concentrations and caused the steel electrodes to depolarize. Since this did not happen for the refined case, it suggests that the phase 2 solution is more conductive so not as much acetone can be tolerated. This is possibly due to residual salts, and may require a lower voltage. Overall, these results were significant because they proved this two-step procedure produced consistent results. The initial raw solution tests varied from 3 to 50% from solution to solution while

the improved second procedure only varied from 18-19% within the same testing conditions. Although a yield of approximately 20% is rather low, since it is repeatable it can be improved given further parameter testing.

Additionally, figure 8 illustrates that our 20% yield numbers are a conservative estimate. Our yield values are calculated by dividing the mass collected out of phase 2 from the initial mass of phase 1. However, this initial mass value includes unreacted precursor and solvent along with the nanoparticles. Meanwhile, our SEM images and composition analysis show that the mass output values contain strictly nanoparticles since there are no chloride or nitrogen peaks present in figure 9b. Figure 8 shows that only approximately 8% of the input raw solution is actually solid material (i.e., unreacted precursor or nanoparticles). This value has a certain degree of error (+/- 10%) since our collected mass should include the ligand on particle's surface, and exclude unreacted precursor. If you calculated a new collection yield using this 8% initial mass of nanoparticle figure it would raise the overall yield to over 100%, which follows logically considering there is some hexane and present in the final film out of phase 2. While the precise determination of nanoparticle yield (or precursor conversion) convolutes the evaluation of nanoparticle separation yield, it indicates that our yield values are likely higher than what we have presented in our figures.

Conclusion

For this project, we aimed to develop a scalable post-synthesis separation procedure utilizing electrophoretic deposition. We ultimately accomplished this goal with our two-step procedure, but the yield value lies far

below a realistic number for commercial applications. However, we believe that with more time and continued testing we could hone our parameters to create a much higher yield value. The next critical steps would be to test additional voltage values and see if they continue to improve the yield numbers, and to examine the impact of electrode spacing on the raw solution to see if it mirrors that of the refined solution tests. Figure 7 supports that further optimization can improve yield as lowering the voltage from 800 to 600 V improved our yield by about 5%.

Future testing and the development of a high yield nanoparticle separation procedure would benefit industry and society immensely by enabling truly continuous fabrication of nanoparticle-based devices. Nanoparticles are a booming field with a plethora of applications, but they will never be commercially feasible for continuous production until a scalable separation technique is developed. Centrifugation is currently the most dominant technique, but size, cost, and efficiency prevent this from being scaled up. Our work helps lay the foundation for the development of electrophoretic deposition as a nanoparticle separation technique and the overall advancement of nanoparticle production methods.

References

- [1] B. Kowalczyk, I. Lagzi, B. A. Grzybowski, Nanoseparations: Strategies for size and/or shape-selective purification of nanoparticles. *Current Opinion in Colloid and Interface Science*, 2011; 1-3:6-9
- [2] D. Kim, H. K. Park, H. Choi, J. Noh, K. Kim and S. Jeong, *Nanoscale*, 2014, DOI: 10.1039/C4NR04351K.

[3] E. Lhuillier, P. Hease, S. Ithurria, B. Dubertret. Selective electrophoretic deposition of CdSe nanoplatelets. *Chemistry of Materials*, 2014; 5-6

[4] J. H. Dickerson, S. V. Mahajan, S. A. Hasan, J. Cho, M. S. Shaffer, A. R. Boccaccini. Electric field assisted fabrication of carbon nanotube-nanocrystal composite structures. SPIE, 2009; 2

[5]Engineeringtoolbox.com,. 2015. 'Dielectric Constant Of Some Common Liquids'. Accessed July 28 2015. http://www.engineeringtoolbox.com/liquid-dielectric-constants-d_1263.html.

[6] Web.mit.edu,. (2015). Retrieved 28 June 2015, from <http://web.mit.edu/8.02t/www/materials/StudyGuide/guide05.pdf>